1-1-2009

Experimental studies of vibrations of flexible structures induced by axial pipe flow

Ravi Kumar Peri
Ryerson University

EXPERIMENTAL STUDIES OF VIBRATIONS OF FLEXIBLE STRUCTURES INDUCED BY AXIAL PIPE FLOW

by

Ravi Kumar Peri

B. Tech, Jawaharlal Nehru Technological University-Hyderabad, 1995

A thesis

Presented to Ryerson University

In partial fulfillment of the requirements for the degree of

Master of Applied Science

In the program of

Mechanical Engineering

Toronto, Ontario, Canada, 2009

Author's Declaration

I hereby declare that I am the sole author of this thesis.

I authorize Ryerson University to lend this thesis to other institutions or individuals for the purpose of scholarly research.

I further authorize Ryerson University to reproduce this thesis by photocopying or by other means, in total or in part, at the request of other institutions or individuals for the purpose of scholarly research.

Signature

Abstract

This thesis presents experimental studies of vibration of a straight beam and a thin plate in axial pipe flow. Dynamic behaviors of the two structures are investigated for a wide range of mean flow velocities. Responses of the structures were measured and analyzed in the time and frequency domains with an aim to understand the fluid-solid interactions. The experimental results reveal that high mean flow velocities can excite higher vibration modes because of turbulence.

Acknowledgements

I'd like to thank Dr. Shudong Yu for his guidance and advice throughout the entire research period and thesis writing.

I'd also like to thank Joseph Amankarah, Alain Machin, Xuan Zhang, Farzin Abbasian, Peter Bulksi and Alokendu Bhattacharya for their assistance in the preparation of the experimental setup.

Finally, I wish to thank my parents for their support, and my wife for her patience and motivation in completing this research. I dedicate this thesis to my son who wishes to be an engineer.

Table of Contents

List of Figures

List of Tables

Nomenclature

L	Length of the cantilever cylinder	m
d_c	Diameter of the cantilever cylinder	m
U_{cd}	Critical flow velocity	m/s
I	Area moment of inertia	m^4
E_c	Young's modulus of elasticity of the cantilever cylinder material	N/ m^2
V_s	Supply voltage	V
U	Mean flow velocity	m/s
d_p	Internal diameter of the pipe	m
ξ	Kinematic viscosity of water	m^2/s
Re	Reynolds number	
$\overline{U}$	Non dimensional flow velocity	
ρ	Density of water	kg/m^3
ν	Poission's Ratio	
E_s	Young's modulus of elasticity of the cantilever plate material	N/ m^2
h	Thickness of cantilever plate	m
L_p	Length of cantilever plate	m
ρ_p	Density of cantilever plate material	kg/m^3
μ^*	Mass ratio	
Q	Mass flow rate	m^3/hr

Chapter 1

INTRODUCTION

Research on axial flow induced vibrations received significant attention from the nuclear industry when dealing with vibrations of heat exchanger tubes and fuel bundles [1]. Experiments were carried out on a cylinder in axial flow in a test loop [2]. The axial flow induced vibrations in industrial structures are usually of small amplitude. These small amplitude vibrations or fretting in nuclear reactor fuel-element bundles can cause wear or damage to the supporting tubes over a long period of time [3]. Replacement of these supporting tubes is costly from time and economic stand points.

Real industrial structures, such as a nuclear fuel bundle, are too complicated in geometry. In this thesis, a straight beam and a thin plate in an axial pipe flow are studied. Results from these simple structures help understand the excitation mechanisms.

Well known mechanisms include vortex shedding (caused by oscillating flow separation from a circular cylindrical structure in cross-flow), galloping (caused by fluid forces due to the motion of a noncircular structure in cross-flow), turbulence buffeting, fluid-elastic instability, and pulsational flow [4, 5]. Turbulence buffeting, fluid-elastic instability and pulsational flow are the three dominating mechanisms in axial flow. Turbulence induced excitation or turbulence buffeting is an extraneously induced excitation due to surface pressure fluctuations associated with turbulence in the flow. The magnitude of these surface pressure fluctuations increases with the increase in the mean flow velocity [6]. Fluid-elastic instability is a flow induced excitation resulting from any or all of the fluid inertia, fluid damping and fluid stiffness forces that arise

from high fluid flow velocities causing large amplitude oscillations. Finally, pulsational flow is another extraneously induced excitation due to the use of limited number of impellers and vanes in pumps [5].

1.1. Objectives and Methodology

The objective of this thesis is to study the flexural vibration behaviors of two simple structures (a beam and a plate) in an axial pipe flow with varying mean flow velocities.

1.2. Literature Review

1.2.1. Cylinder in axial flow

The dynamics of a beam of circular cross section (also called cylinder) in axial flow was studied by Païdoussis [1] both analytically and experimentally. His works lead to the derivation of the equations of motion including the effect of axial flow. According to Païdoussis [7], cylinders experience fluid-elastic instabilities when the mean flow velocity reaches certain critical values.

Vibration of cylindrical structures in axial flow was directly related to the power industry. The following topics are significant to the concerned industries [3]:

(i) Measurement of the amplitude of particular cylindrical structure configurations, modeling nuclear reactor components and flow conditions.

(ii) Understanding the causes of vibrations such as turbulence buffeting, fluid-elastic instability, pulsational flow etc.

(iii) Development of means for predicting the vibration amplitudes which is an important ingredient for design.

From experiments [3, 8, 9], it was found that, for a solid steel cylinder with $L/d_c = 100$ in water flow, the dimensional critical flow velocity $U_{cd} \sim 1180$ ft/s ~ 360 m/s in order to observe any fluid-elastic instabilities. Such high mean flow velocities are not possible in practical applications. Even for very slender hollow cylinder, excited by the flow in both its beam and shell modes, with $L/d_c = 100$ and a thickness-to-diameter ratio of 1/50, the critical velocity $U_{cd} \sim$ 29 m/s, which is very large in practice.

For this reason, experiments on fluid-elastic instabilities have been carried out for cylinders of elastomers (with very low modulus of elasticity E_c) in order to experimentally observe the said phenomenon in axial flow.

1.2.2. Plates in axial flow

Study on the dynamics of plates finds an important place in the aeronautical industry. The reason can be attributed to the application of this study to high-performance aircraft and missile skins. Similarly, hydroelasticity of plates includes dynamics of plates in relation to application to submarine skins, boundary-layer transition to turbulence and noise generation. Paper making and winding, high-speed tape winding and spinning disks in disk-drives are a few more applications that make the study of plate vibration in axial flow important.

Applications of this kind of fluid-structure interaction system could be traced to renewable sources of energy generation by extracting energy from the surrounding fluid flow for generation of electric power. One such concept of new energy-harvesting devices is called the flutter-mill. All this was based on the dynamics of cantilever flexible plates subjected to axial flow. In the theoretical work done by Païdoussis et al. [10, 11], he found that cantilever flexible plates subjected to axial flow lose stability by flutter at a sufficiently high flow velocity.

An application proposed by Allen and Smits [12] is to use piezoelectric foils in an ocean current, oscillating in response to vortices shed from a bluff body located upstream and convected along their lengths thereby generating electricity.

1.3. Contributions and usefulness of the proposed research

In the experiment with cylinder in axial flow an underwater bi-axial accelerometer was used to pickup the fluid-structure interactions. In the experiments available in the literature, visual aids were used for a similar study. This thesis presents some much needed quantitative experimental studies. A plate was placed inside a water-flowing pipe. The lateral vibration response was picked up using a tri-axial accelerometer. In the literature, the experiments were carried out with fluid flow on one side of the structure in the case of a hydro-elastic study.

In the experiments, smart sensors (Micro-Electro-Mechanical Systems accelerometers also known as MEMS accelerometers) were used. The bi-axial and tri-axial MEMS accelerometers are available at a very low cost and at the same time designed with built-in low-pass filters measuring frequencies from 0.5 Hz to 550 Hz. These MEMS accelerometers are ideally suited for the above experiments, as the research in flow induced vibrations focuses on low frequency. Calibrations and the manufacturer's data sheets show that these sensors exhibit on-par sensitivity with respect to their piezoelectric counterparts. Another advantage over piezoelectric sensors is that these MEMS accelerometers, for a given sensor size, pickup responses in 2–axes in the case of bi-axial ones and 3-axes in the case of tri-axial ones. The tiny size of these sensors including the circuit board can be designed within a diameter of 8 mm and can be embedded axially in a cylinder of 12 mm diameter. This would not be possible in the case of commercially available piezoelectric accelerometers due to their larger sizes.

1.4. Structure of Thesis

The experimental setups are described in Chapter 2. Experimental data processing, analysis and discussions for the cylinder are presented in Chapter 3. Experimental data processing, analysis and conclusion for the rectangular plate are given in Chapter 4. Conclusions and recommendations for future work are given in Chapter 5.

Appendix A contains detailed steps involved in cylinder and plate preparations for the experiments. The data sheets for accelerometers ADXL321 and ADXL335 are provided in Appendices B and C respectively. The tensile test results and the technical data for silicon chord stock from the manufacturer are given in Appendix D. Appendix E contains the calibration procedure and charts for bi- and tri- axial accelerometers.

Chapter 2

EXPERIMENTAL SETUP AND PROCEDURE

2.1. Test Rig without Tank

In the nuclear power industry, the piping network is designed as a closed loop system and high velocities of flow are achieved using a centrifugal pump. Pump pulsations in such systems are quite predominant. Consequently, the signals from turbulence induced vibration of structures are often embedded in the noise pump pulsation signals. In order to capture signals from the fluid structure interaction due to turbulent flow, the test rig was modified by adding a tank for absorbing energy from flow pulsations.

The water circulating test rig contains two sets of pipes. The first set of pipes of 8 inch (204 mm) diameter is placed at the ends of the closed loop (photographed in Figure 2.1-1). The second set of transparent pipes of 4 inch in diameter is placed in the central portion as a test chamber and is 64 inch (~1625 mm) in length. A digital flow meter is installed near the discharge end for monitoring the mean flow rate.

A 7-vane centrifugal pump, with radial inlet and radial outlet, powered by a 3-phase 60 Hz motor (10 HP, 1760 RPM rated speed), is used to achieve desired flow rates. The spindle speed of this motor is controlled by a Danfoss VLT6000 system in 1-60 steps, thus enabling a fine increment in flow velocities. In this test rig, the position of the test structure is 40 inch or 10 times the pipe diameter from the 90 degree bend to ensure that the incoming flow is a fully developed pipe flow. The rig along with the test section was filled up with water at room temperature and a static pressure of 40 psi (~280 kPa). Measures were taken to eliminate air bubbles in the system

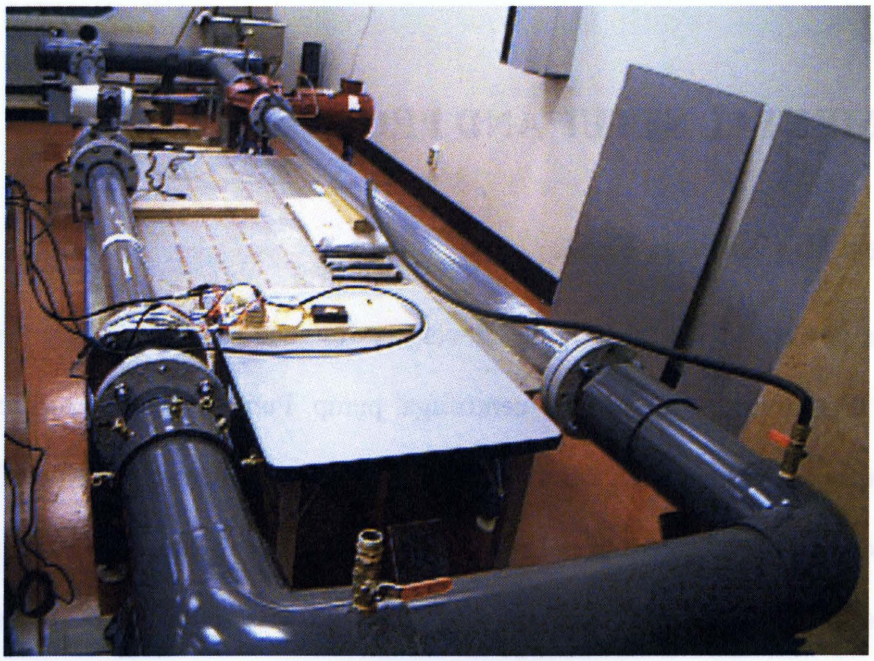

Figure 2.1-1 Test rig setup for the FIV experiment without the tank

2.2. Test Rig with Tank

In the process of upgrading the previous setup of test rig, a reservoir was added. The test rig was revamped and structurally reinforced with 11 rigid supports replacing floating ones. The tank of 48 inch in diameter and 73 inch in height has capacity of 500 US gallons. Figure 2.2-1 shows the entire experimental setup with the tank, which was introduced mainly to reduce the flow pulsations.

In this rig, the test section is placed at ~3.8 m downstream from the 90 degree bend maintaining smooth flow. The rig along with the test section was filled up with water at room temperature with approximately 1.8 m positive head that eliminates all air bubbles initially trapped into the system during filling.

Figure 2.2-1 Test rig setup for the FIV experiment with the tank

2.3. Preparation of cylinder

For this experiment the clamped-free cylinder (or cantilever cylinder) with blunt end was made from a commercially available 12.7 mm diameter silicon rubber chord stock manufactured by Global Rubber Products, Ontario having a specification S70 – a 70 durometer silicon rubber was used. Appendix A provides detailed steps in the preparation of this cylinder. Technical report with physical and mechanical properties for the above material from manufacturer and results from tensile test performed for the chord stock in Mechanical Engineering Department materials lab enclosed in Appendix D. The Figure 2.3-1 shows the isometric view of the cantilever cylinder and aluminum holder permanent assembly.

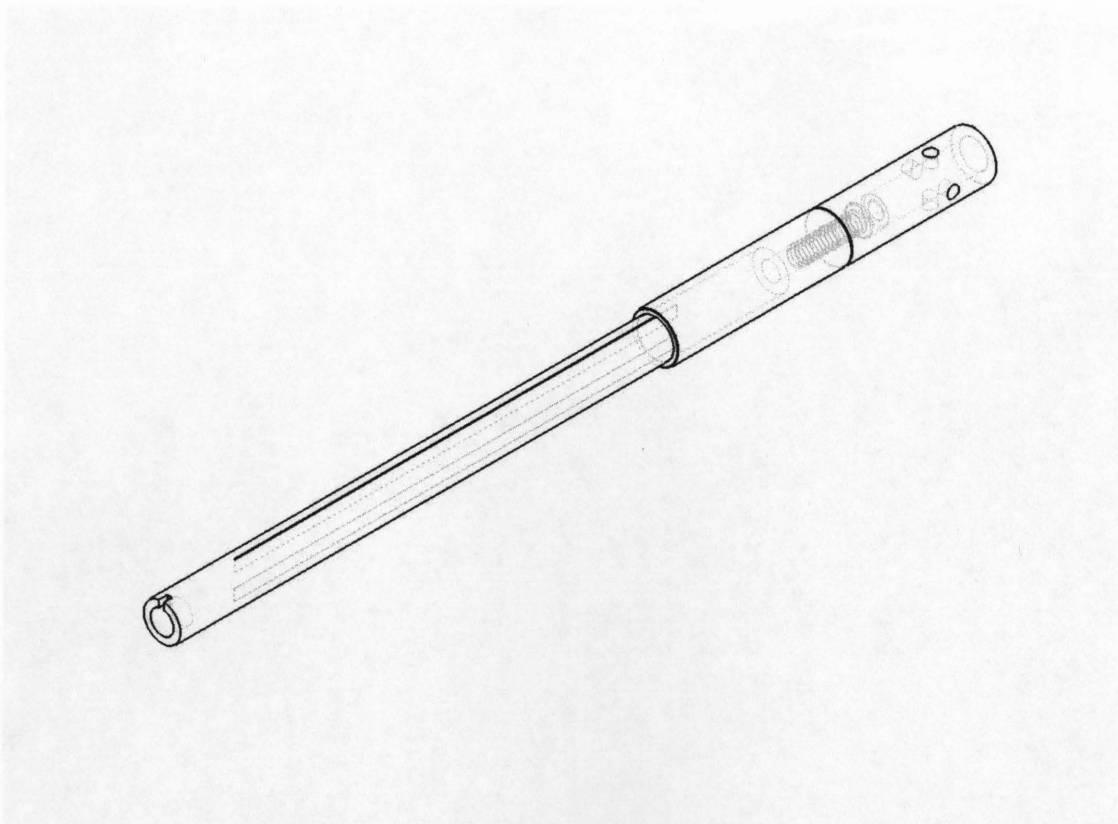

Figure 2.3-1 Isometric view of the permanent assembly - cantilever cylinder containing the silicon rubber chord stock, stainless steel strips, the aluminum fixture and adaptor with the 1/4in socket head cap screw

Selection of Accelerometer: In most engineering applications high-amplitude low-frequency vibrations of 4 Hz to 300 Hz cause damage or failure of equipment [13 & 14]. This was one of the driving factors in the selection of underwater accelerometer in addition to sensitivity, resolution and size. Given that the diameter of the elastomer cylinder is 12.7 mm diameter by design, the accelerometer circuit board was limited to 8 mm diameter so that its installation causes minimal distortion in the free end of the cylinder.

Extensive research for an underwater accelerometer (piezo-electric or MEMS) in the market showed they are expensive. Thus and the search was limited to above-water MEMS type transducer as it was more economical and easy to install along with its tiny circuit. The ADXL321 from Analog Devices is a MEMS type thin and small with 4 mm square by 1.45 mm

thick, 16-lead and plastic lead frame chip scale packaging features capable of measuring acceleration with a full-scale range of ±18 g.

The ADXL321 is a small and thin, low power, complete dual-axis accelerometer with signal conditioned voltage outputs, single monolithic integrated circuit. It can also measure both dynamic acceleration (vibration) and static acceleration (gravity). The bandwidth of the accelerometer established as 0 – 500 Hz using capacitors 0.01 μF for both X and Y axes at the XOUT and YOUT pins per data sheet, enclosed in Appendix B, to suit application.

Typical vibration spectra of cantilevered flexible cylinders in highly confined axial flow sensed with embedded accelerometer [9], recorded that the acceleration experienced was over 5g (rms) and hence transducer with a full scale range of ±18 g for measuring acceleration was considered to be sufficient for this experiment.

A two layered printed circuit board was designed with help from Satellite Design and Management Lab (Ryerson University) using free printed circuit board (PCB) layout software from Express PCB (www.expresspcb.com) in order to manufacture in-house tiny accelerometer circuit limiting size to 8 mm diameter and 4 mm thick. This custom design was required to suit to the size of the cylinder with flexible connections. The ones available in the market, of a slightly bigger size with under water capability, were quite expensive. A local vendor in Markham, Ontario, provided its services in installing the components on these boards thus making reliable accelerometers.

Four long flexible multi strand wires of predetermined length were taken out of commercially available 60 conductor ribbon cable (multi wire planar cable) and soldered to the accelerometer to complete the circuit.

As per manufacturer guidelines and recommendations the ADXL321 type accelerometer though tested and specified at supply voltage, V_S = 3 V. However, it can be powered with V_S as low as 2.4 V or as high as 6 V. The zero g bias output being ratiometric, hence the zero g output nominally equal to $V_S/2$ at all supply voltages. A DC supply of 4.5 V generated from three 1.5 V of AA size batteries is provided to the accelerometer for two main reasons:

- The output being ratiometric, so the sensitivity (or scale factor) varies proportionally to supply voltage: at V_S = 5 V, typically sensitivity is 100 mV/g; at V_S = 2.4 V, typically sensitivity is 45 mV/g as per manufacturer.
- The output noise was not ratiometric but was absolute in volts. As a result the noise density decreases as the supply voltage increases. The reason being the scale factor (mV/g) increases while the noise voltage remains constant. At V_S = 5 V, the noise density typically 190 μg/√Hz, while at V_S = 2.4 V, the noise density typically 400 μg/√Hz as given in manufacturer's literature.

Accelerometer calibration was carried out by using Dytran made calibration shaker as shown in Appendix E. The sensitivity of accelerometer was taken as 84 mVolt/g or 0.084 Volt/g or equivalent to 116.785 m/s^2 /Volt from the calibrations charts.

Cantilever setup with transducer: The accelerometer was carefully oriented with its 4 mm square face parallel to the cross section and installed in the axial hole at the free end of the cantilever cylinder. Further to this the square side of the accelerometer was aligned parallel / perpendicular to the stainless strips in the cantilever cylinder manually within ±1.0° accuracy.

Silicon rubber adhesive (Sil-Poxy from Smooth-On Inc., Easton, PA) was evenly applied over the inserted transducer to fill up the axial hole on the free end of cantilever cylinder making it a blunt flat end with minimum surface imperfections.

The wires of the accelerometer were carefully oriented and laid on either side of the stainless steel strip along the axis of the cylinder and retained in place with silicon rubber adhesive. This was done in such a way that the four-single 28 gauge multi-strand wires have negligible effect on the flexural rigidity (E_c*I) of the cantilever cylinder. These wires were routed axially on the aluminum fixture and adapter using the above silicon rubber adhesive as shown below in Figure 2.3-2.

Test-fixture for cantilever cylinder: In order to place the cantilever along the axis of the test section of pipe in the water circulating test rig a simple Test-Fixture was designed with a 4 inch (101.6 mm) outside diameter (OD) and 3½ inch (88.9 mm) inside diameter polycarbonate tube. The OD of the tube was machined down to 100 mm diameter for a length of 86 mm leaving a shoulder so that it can slide into the test section of the pipe without interference. Four equally spaced radial holes drilled through all the wall thickness of the tube and tapped with M4x0.7 threads at a predetermined position(s).

The cantilever was then secured along the axis of the tube with the help of M4 x 0.7 stainless steel studs and three pairs of M4 x 0.7 hexagonal nuts to achieve zero DOF at the adapter end of the cantilever. The cantilever cylinder was located axially along the test-fixture by tensioning the three stainless steel studs between the aluminum adapter and polycarbonate tube. Figure 2.3-3 shows the arrangement.

Figure 2.3-2 Isometric view showing the installation of the accelerometer with wires on the cantilever cylinder

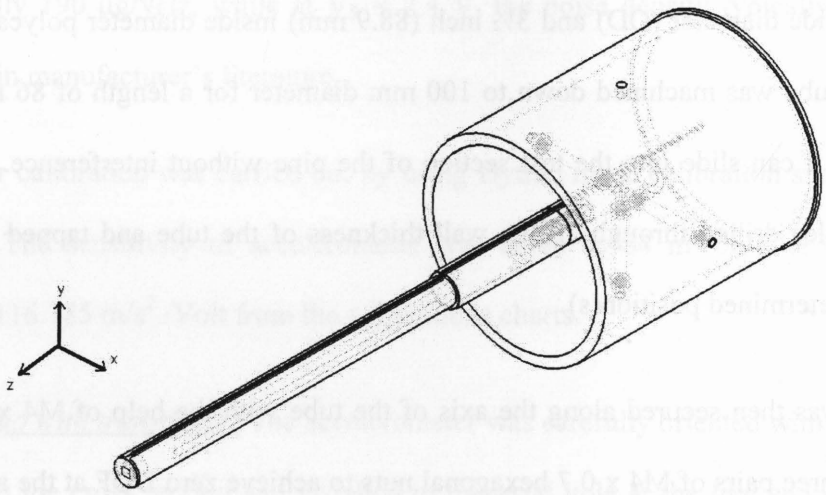

Figure 2.3-3 Isometric view of the test-fixture for the cantilever

Experimental Setup:

This test-fixture – cantilever cylinder assembly then inserted carefully into the test section of the water pipe in the water-circulating test rig ensuring the orientation of the stainless strips in the cantilever along the vertical plane ensuring the orientation of the accelerometer along the horizontal or vertical axis with ±1.0° accuracy.

The test-fixture – cantilever cylinder assembly was then secured rigidly with zero DOF by compression force provided by the mating flange to the pipe of the test section in the rig and the electrical leads are cautiously routed along the face of the flange and connected to the circuit using the terminal strip.

The circuit consists of the following components:

1. Test fixture – cantilever cylinder assembly in the water circulating test rig
2. Data acquisition system comprising a laptop (oscilloscope software loaded) and USB Oscilloscope - Handyscope HS4 with 4 channels, sampling 195.3125 kHz at 16 bit resolution (from TiePie engineering, Netherlands)
3. 4.5V DC battery pack with four port terminal strip
4. Two coaxial cables with BNC connectors on one end and the other end open

An additional accelerometer was installed on the mid-section of the test pipe along the radial and tangential planes to pick up the structure vibrations induced by the flow. Figure 2.3-4, Figure 2.3-5 and Figure 2.3-6 illustrate the setup.

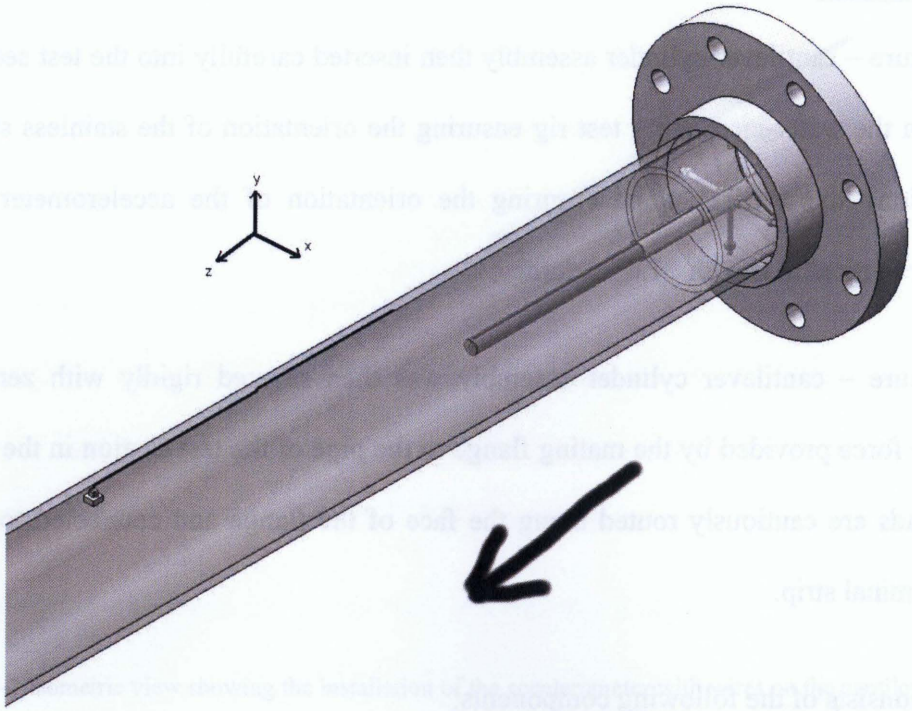

Figure 2.3-4 The test section with the fixture-cantilever cylinder assembly

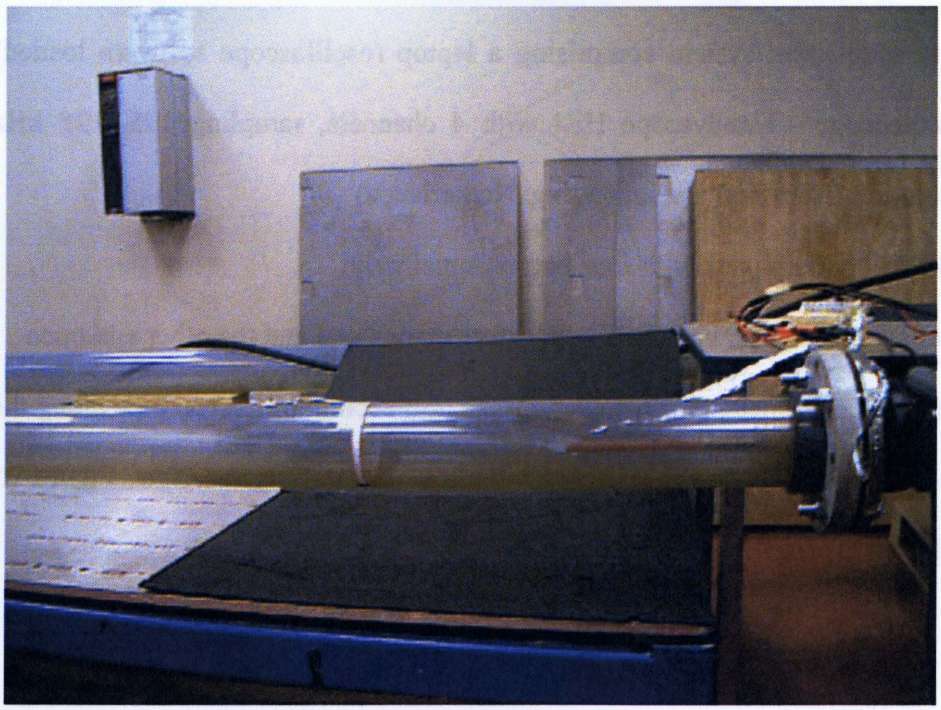

Figure 2.3-5 Front view of the experimental setup

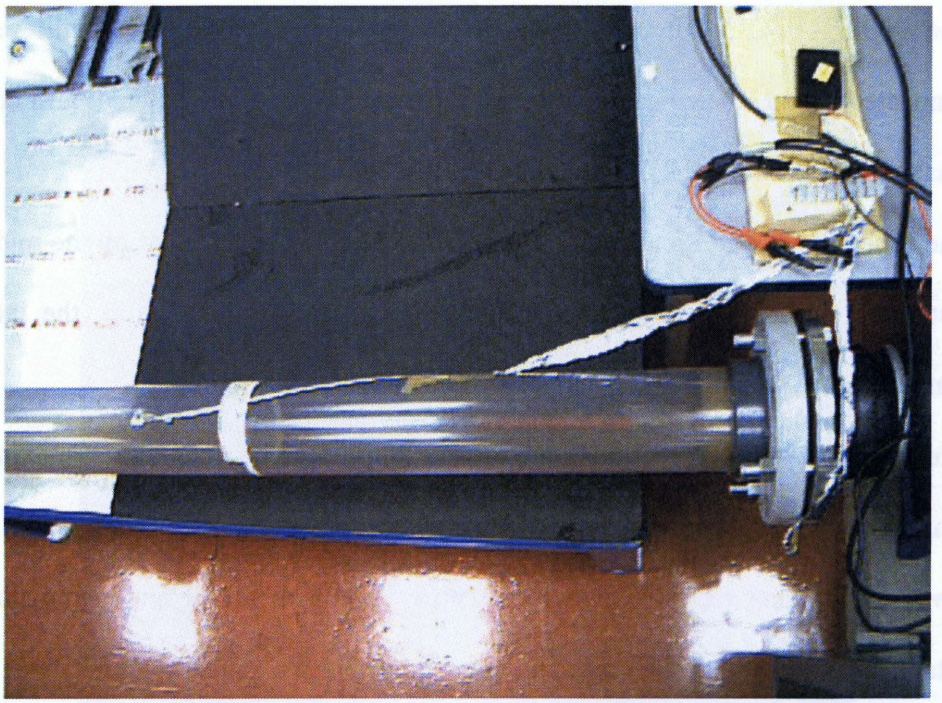

Figure 2.3-6 Top view of the experimental setup

Experimental procedure:

1. Flow meter readings recorded at each increment of pump controller from 1 Hz to 57 Hz
2. The flow meter was then turned off to avoid picking up noise i.e., 60 Hz and its multiple harmonics by the accelerometer(s)
3. The fluorescent lights were turned off to avoid picking up of noise 120 Hz and its multiples
4. Laptop was operated on battery for the entire duration of the experiment when data was acquired to avoid picking up AC ripples at 60 Hz and its multiples
5. USB Oscilloscope - Handyscope HS4 connected to the laptop
6. Accelerometers were powered with the 4.5V DC battery pack using the terminal strip

7. The XOUT, YOUT from the accelerometer embedded in the cantilever cylinder connected to the coaxial cables through the terminal strip, the latter in turn connected to Channel 1 and Channel 2 of the USB Oscilloscope
8. The Pipe-XOUT and Pipe-YOUT from the accelerometer installed on the mid-section of test rig connected to the coaxial cables through the terminal strip, the latter in turn connected to Channel 3 and Channel 4 of the USB Oscilloscope
9. Sampling rate was set to 10 kHz at 16 bit resolution while maintaining maximum record length of 131,072 samples for the USB Oscilloscope
10. Two sets of data recorded when the entire system was still and pump turned off to establish the level of white noise and noise threshold
11. For each increment (1 Hz) in the controller frequency, the pump spindle ramps ½ hertz and data was captured for all channels
12. From 2 Hz to 57 Hz controller frequency the data recorded for each change in frequency after ensuring 30 seconds settling time for the flow
13. Few videos were taken to capture the flow induced vibrations of the cantilever
14. This procedure was carried out once in test rig without tank and once with test rig with tank

Figure 2.3-7 show the test fixture - cantilever cylinder assembly post experiment.

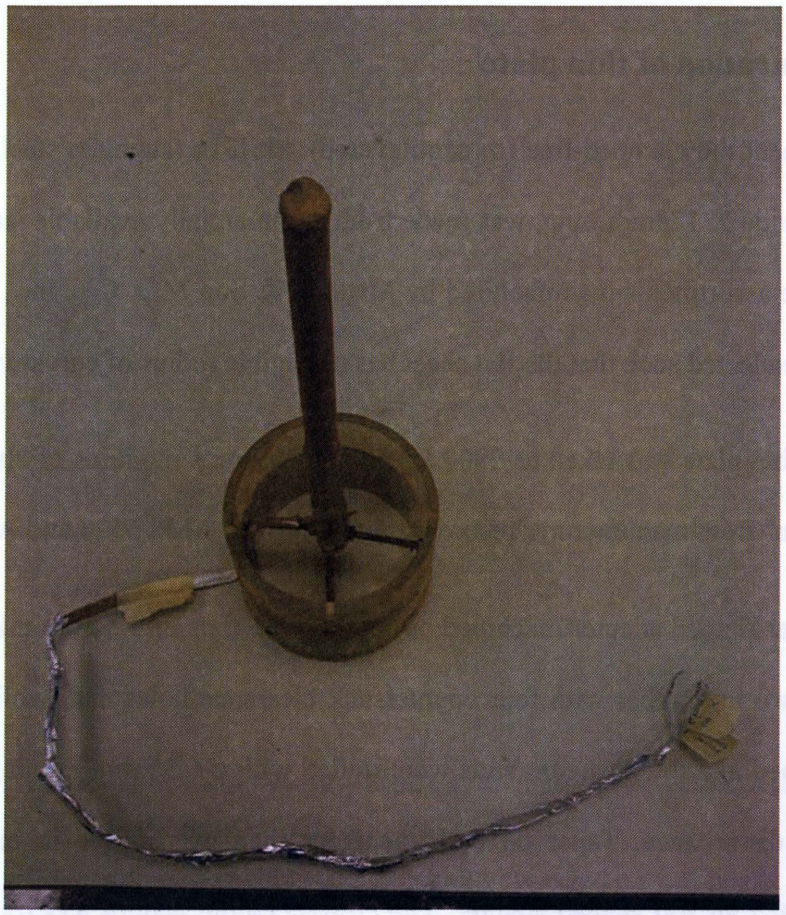

Figure 2.3-7 The cantilever cylinder and fixture tube arrangement – post experiment

2.4. Preparation of thin plate

For this experiment the clamped-free (or cantilevered) AISI316 (stainless steel) plate, 0.178mm thick X 36mm wide X 175mm long, was made from commercially available stainless steel shim flat pack 9 piece assortments manufactured by Maudlin & Son Mfg. Co., Inc., USA. The width of the plate was selected such that the flat sheet has negligible radius of curvature.

The density of the plate was taken as 7900 kg/m^3 and Young's modulus of elasticity was taken as 200 x 10^9 N/m^2 from manufacturer records complying with AMS 5524 and ASTM-A-666.

An aerofoil / pear shaped adapter machined out of Al 6061 flats of 6.35mm thick X 38mm wide X 54mm long two in number with four countersunk clearance holes and two M4 tapped holes. These are clamped and the upstream ends were milled with a 6.35 mm radius cutter in order to minimize flow disturbance. Taper on both the faces then was milled in order to obtain an approximate pear / air foil shaped adapter. The clearance-hole pattern was transferred from the aluminum adapter to the stainless steel plate. Four M4 x 0.7 flat screws of predetermined length used to clamp the stainless steel plate to the pear shaped adapter as shown in Figure 2.4-1.

Silicon rubber epoxy is applied to downstream ends of the aluminum adapter in order to have a smooth transition for fluid flow from the adapter to the plate thus minimizing flow disturbances.

Selection of Accelerometer: Measuring range from 0.5 Hz to 300 Hz was considered as one of the driving parameters in the selection of underwater accelerometer in addition to sensitivity, resolution and size. The thickness of the plate and the lateral vibrations dictated requirement of very light and thin accelerometer circuit board with a transducer slim enough to minimize flow disturbances and having minimal effect on the stiffness of the plate upon installation.

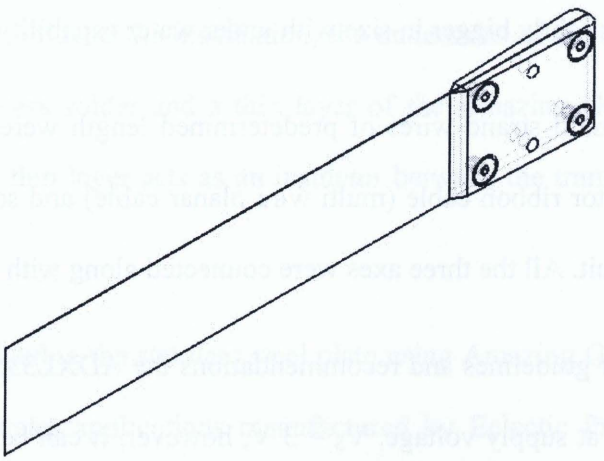

Figure 2.4-1 Isometric view of the permanent assembly of the cantilever plate to the aluminum adaptor with M4 flat head screws

Thus the ADXL335 from Analog Devices, a MEMS type thin and small with 4mm square by 1.45mm thick, 16-lead and plastic lead frame chip scale packaging features capable of measuring acceleration with a full-scale range of ±3 g, was selected in order to measure lateral vibrations.

The ADXL335 is a small and thin, low power, complete 3-axis accelerometer with signal conditioned voltage outputs. It can also measure both dynamic acceleration (vibration) and static acceleration (gravity). The bandwidth of the accelerometer was established as 0.5 Hz to 1600 Hz for the X, Y axes and 0.5 Hz to 550 Hz for the Z axis using capacitors of 0.01μF for the X, Y and Z axes as recommended in the data sheet given in Appendix C, to suit the application.

A two-layer printed circuit board was designed using free printed circuit board (PCB) layout software from Express PCB (www.expresspcb.com) in order to manufacture in-house tiny

accelerometer circuit limiting size to ~2mm thick x 9mm wide and 18mm long. The custom design of the sensor was required with flexible connections for the given plate thickness. In the market sensors to a slightly bigger in size with under water capability were quite expensive.

Five long flexible multi strand wires of predetermined length were taken out of commercially available 60 conductor ribbon cable (multi wire planar cable) and soldered to the accelerometer to complete the circuit. All the three axes were connected along with power and ground wires.

As per manufacturer guidelines and recommendations the ADXL335 type accelerometer though tested and specified at supply voltage, V_S = 3 V, however, it can be powered with V_S as low as 0.3 V or as high as 3.6 V. A DC supply of 3.0 V generated from of two 1.5 V AA batteries is provided to the accelerometer for two main reasons:

- The benefit from the output that being ratiometric, so the sensitivity (or scale factor) varies proportionally to supply voltage. At V_S = 3 V, the sensitivity is typically 270 mV/g in each axis as per manufacturer specifications. These accelerometers have quite negligible variation in sensitivity due to change in temperature.
- The output noise was not ratiometric but absolute in volts; therefore, the noise density decreases as the supply voltage increases. The reason being the scale factor (mV/g) increases while the noise voltage remains constant. At V_S = 3 V, the noise density 300 μg/√Hz in Z axis, as indicated in manufacturer's literature.

The sensitivity of the accelerometer was taken as 218 mV/g or 0.218 V/g or, in other words, equivalent to 4.6 g/V or 45 m/s^2/V from the calibration (details provided in Appendix E) of both the transducers.

Cantilever plate setup with transducers: Two accelerometers along with the leads were installed flat on the cantilever plate at a distance of 35 mm, approximately one fifth of the total plate length, from the clamp end. Prior to the installation, the undersides of the accelerometer boards were sanded to remove excess solder and a thin layer of the Amazing GOOP-Marine contact adhesive was applied. This thin layer acts as an insulator between the transducer board and the SS plate.

The accelerometers were glued to the stainless steel plate using Amazing GOOP-Marine contact adhesive meant for underwater applications manufactured by Eclectic Products, USA. Upon curing of the adhesive a multiple-layers transparent nail polish was applied on the transducer circuit board to make it water proof. To ensure further safety a thin layer of silicon rubber adhesive (Sil-Poxy from Smooth-On Inc., Easton, PA) was evenly applied on the top of the board and leads to provide minimum surface imperfections.

The leads were glued to the plate surface and carefully routed to the aluminum adapter. This was done in such a way that the five-single 28 gauge multi-strand wires have minimum effect on the flexural rigidity (E_p*I) of the cantilever plate. These wires were routed axially on the aluminum adapter using the above silicon rubber adhesive as shown below in Figure 2.4-2.

Two dummy transducer boards of identical dimensions were glued on the opposite side of the plate so as to minimize the flow disturbance caused by the raised surfaces of the real transducer boards.

Test fixture-Cantilever plate assembly: A clear polycarbonate tube was designed and machined much similar to the test fixture used for the cantilever cylinder (further details provided in

Appendix A). The cantilevered plate was located axially along the test-fixture by tensioning the four stainless steel studs between the aluminum adapter and polycarbonate tube. Figure 2.4-3 shows the arrangement.

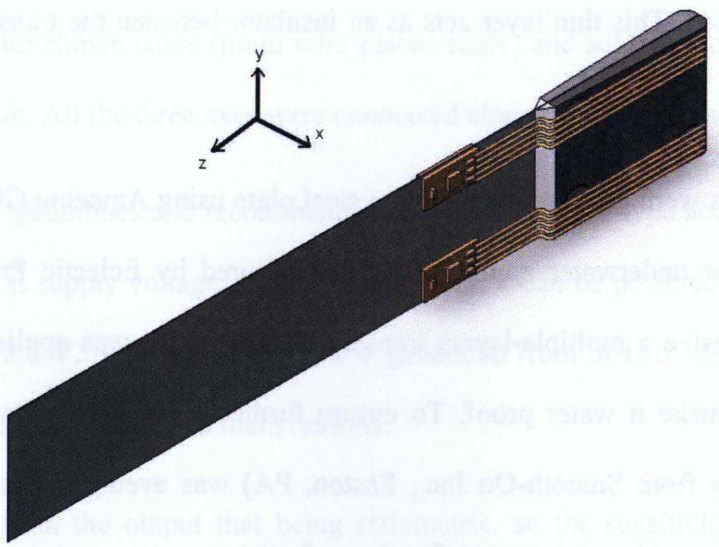

Figure 2.4-2 Isometric view showing the installation of the accelerometers with wires on the cantilever plate

Experimental Setup:

This test-fixture – cantilever plate assembly inserted carefully in to the test section of the water pipe in the water-circulating test rig ensuring the orientation of the thickness of cantilever stainless plate normal to the vertical plane ensuring the orientation of the accelerometer normal to flow with a ±1.0° accuracy.

The test-fixture – cantilever plate assembly was then secured rigidly with zero DOF by compression force provided by the mating flange to the pipe of the test section in the rig and the electrical leads are cautiously routed along the face of the flange. They are connected to the circuit using the terminal strip along with the following components:

1. Test fixture – cantilever assembly in the water circulating test rig
2. Data acquisition system comprising a laptop (Oscilloscope software loaded) and USB Oscilloscope - Handyscope HS4 with 4 channels, sampling 195.3125 kHz at 16 bit resolution (from TiePie engineering, Netherlands)
3. 3.0 V DC battery pack with four port terminal strip
4. Two Coaxial cables with BNC connectors on one end and the other end open

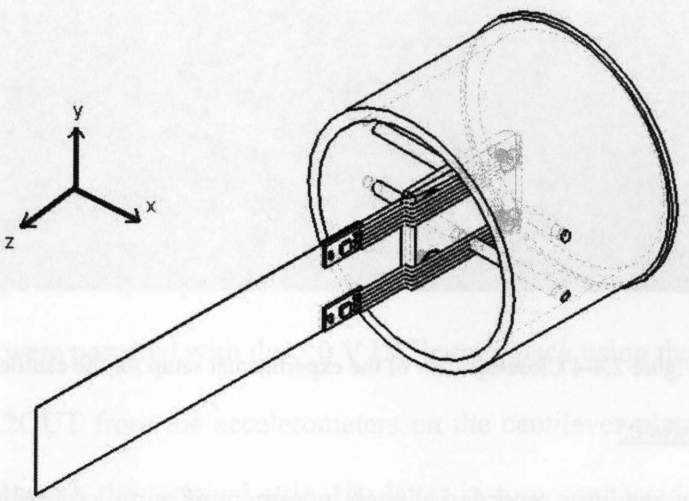

Figure 2.4-3 Isometric view of the test-fixture for the cantilever plate

The position of the cantilever plate was approximately 12.5 ft or 3.8 m downstream from the 90 degree bend in the rig to avoid flow separation and other sharp bend induced vortices. The fixture assembly along with transducer, leads and masking tapes on the studs inevitably induce wakes and other flow disturbances due to the setup design. The rig along with the test section was filled up with water at room temperature. The tank was filled with 450 gallons of water

ensuring the discharge immersed in water to minimize two phase flow. Figure 2.4-4 and Figure 2.4-5 show the setup.

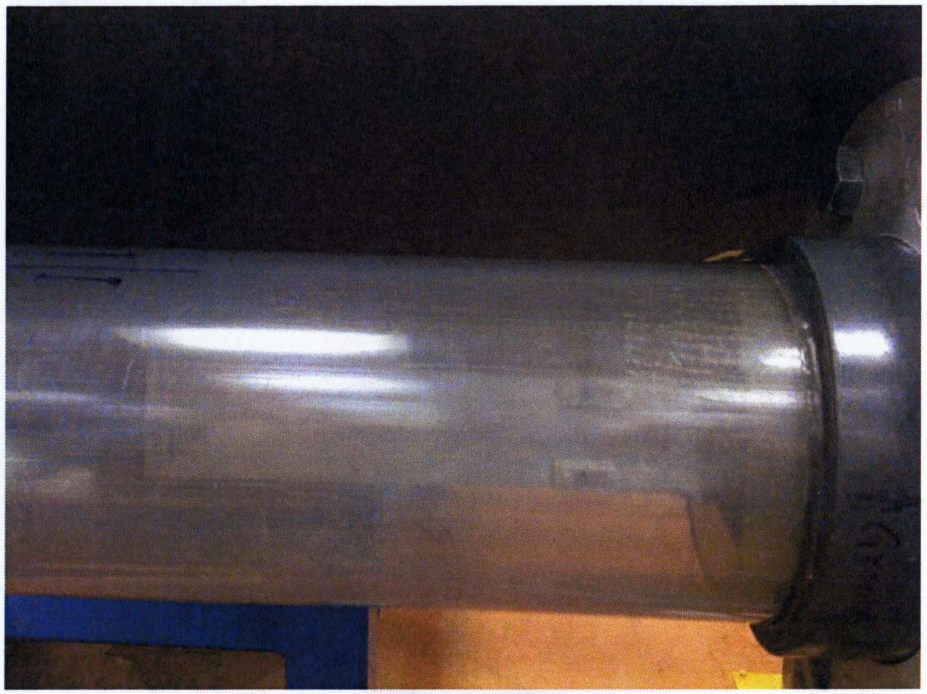

Figure 2.4-4 Close-up view of the experimental setup for the cantilever plate

Experiment procedure:

1. Flow meter readings recorded at each increment of pump controller from 1 Hz to 40 Hz
2. The flow meter was then turned off to avoid picking up of noise i.e., 60 Hz and its multiple harmonics by the accelerometer(s)
3. The fluorescent lights were turned off to avoid picking up of noise 120 Hz and its multiples
4. Laptop was operated on battery for the entire duration of the experiment when data was acquired to avoid picking up AC ripples at 60 Hz and its multiples

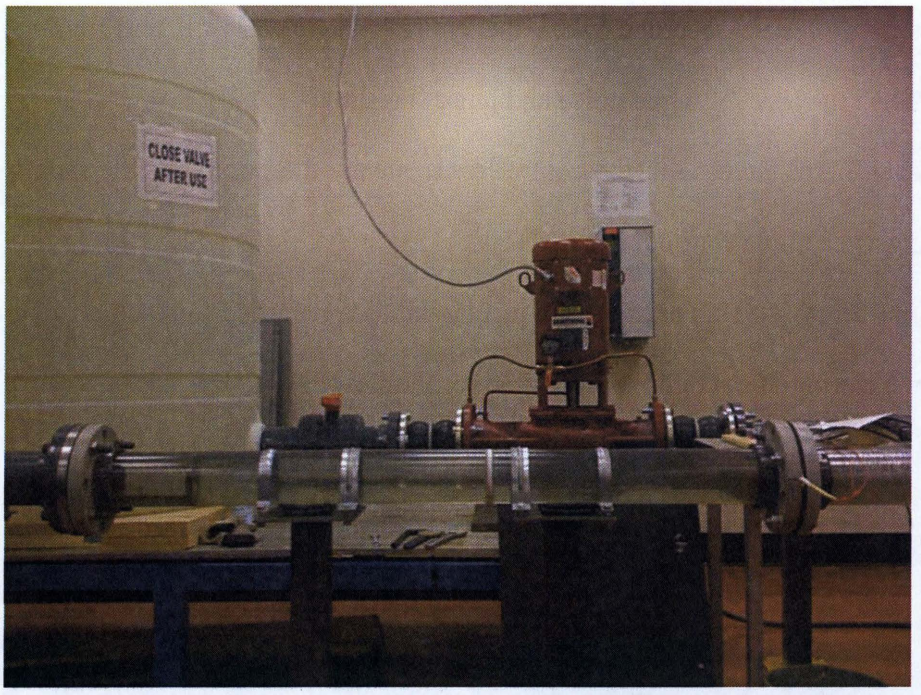

Figure 2.4-5 Front view of the experimental setup for the cantilever plate

5. USB Oscilloscope - Handyscope HS4 connected to the Laptop
6. Accelerometers were powered with the 3.0 V DC battery pack using the terminal strip
7. The X1OUT, X2OUT from the accelerometers on the cantilever plate connected to the coaxial cables through the terminal strip, the latter in turn connected to Channel 2 and Channel 3 of the USB Oscilloscope
8. Three sets of data were recorded at 30 Hz controller reading at different sampling rates of 5 kHz, 10 kHz and 20 kHz at 16 bit resolution while maintaining a record length of 65,536 samples for the USB Oscilloscope
9. After initial analysis from the above data for convergence sampling rate was set to 5 kHz at 16 bit resolution while maintaining maximum record length of 65,536 samples for the USB Oscilloscope

10. Two sets of data recorded when the entire system was still and pump turned off to establish the level of white noise and noise threshold
11. At each hertz increase in the controller frequency the pump spindle ramps ½ hertz and data was captured for both channels
12. From 2 Hz to 40 Hz controller frequency the data recorded for each change in frequency after ensuring 30 seconds settling time for the flow
13. Few videos recorded to capture the flow induced vibrations of the cantilever

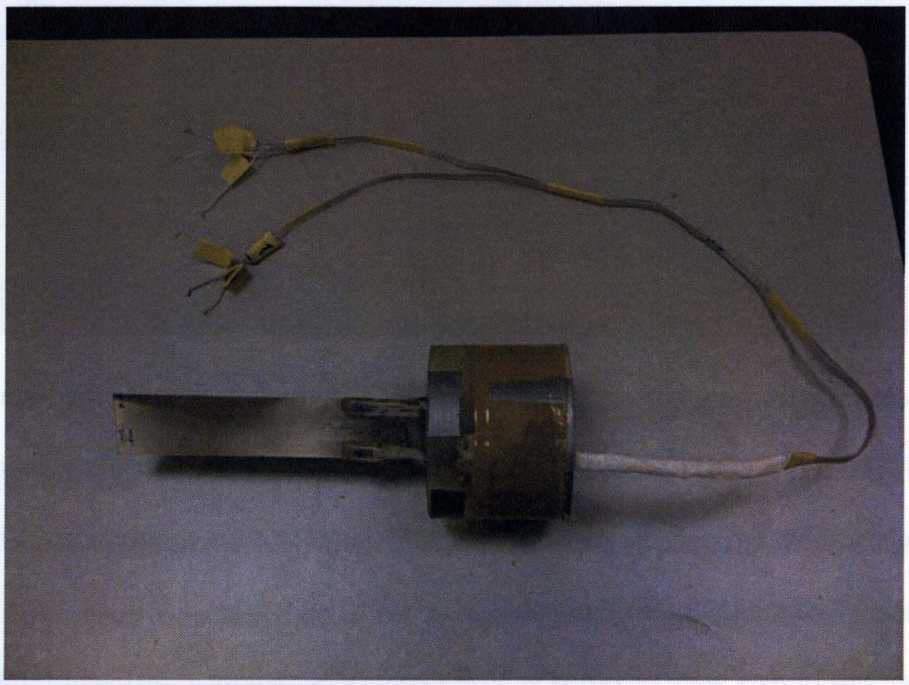

Figure 2.4-6 The cantilever plate with the two accelerometers – post experiment

Figure 2.4-6 and Figure 2.4-7 show the test fixture - cantilever cylinder assembly post experiment.

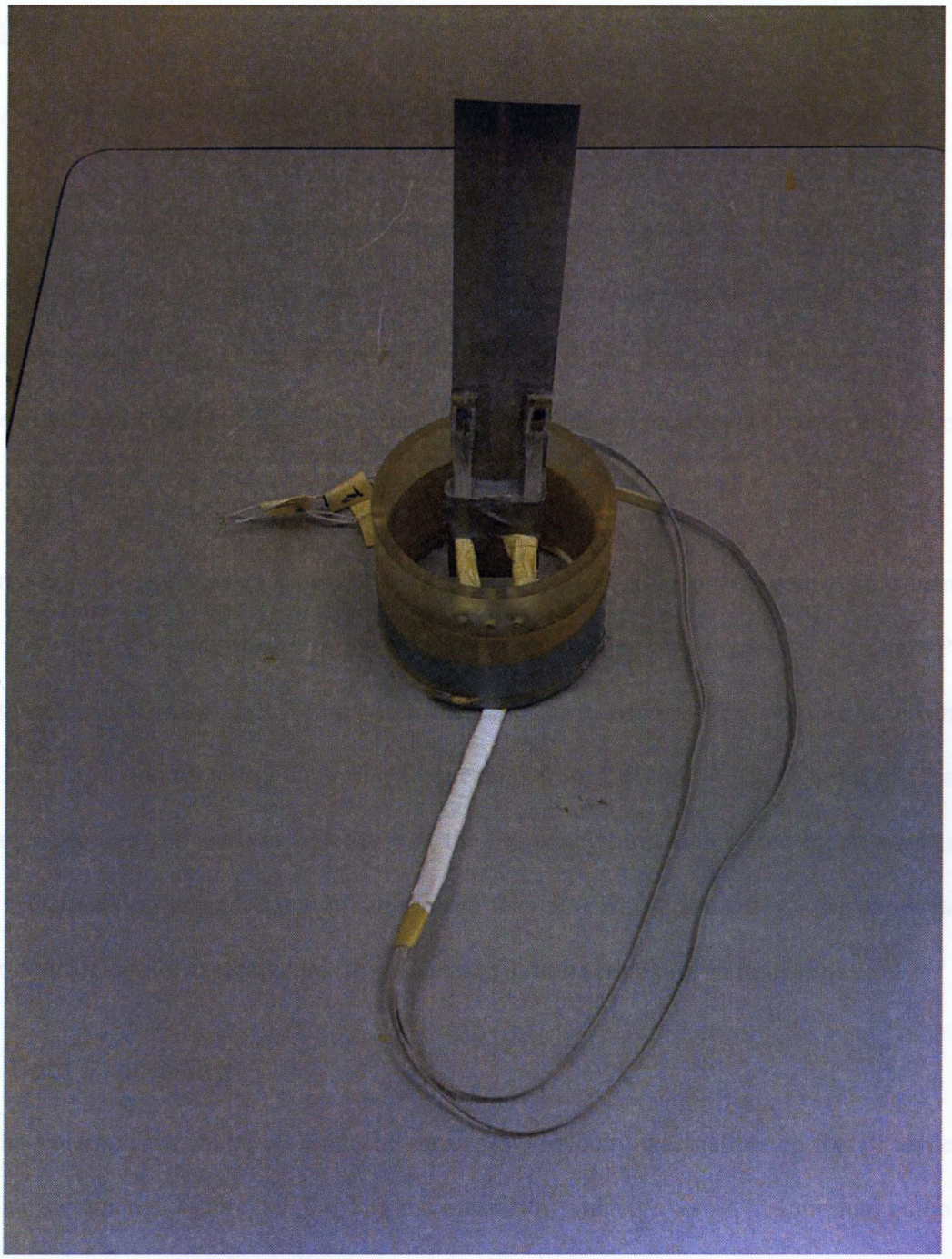

Figure 2.4-7 The cantilever plate and the fixture tube arrangement – post experiment

Chapter 3

AXIAL FLOW INDUCED VIBRATION OF A CYLINDER

In this Chapter, a series of experiments were performed on a cylinder in axial flow. The motion of the cylinder was picked up using a MEMS-based accelerometer, sampled using a data acquisition system (HS4), and processed using MATLAB. Temporal averages for a set of recorded data were determined to show that the flow induced vibration is random and ergodic in nature.

The time-domain rms accelerations of the cylinder motion are plotted against the mean flow velocity U m/s for a wide range. In the frequency domain, the power spectra densities (PSD's) are obtained by means of fast Fourier transform for accelerations for a number of mean flow velocities corresponding to the controller frequencies from 2 Hz to 54 Hz. A total of 52 sets of data were recorded and analyzed. Because of the frequency limitation of the accelerometers, the PSD's are shown only for frequency range from 0 to 500 Hz. Fortunately, the upper limit of 500 Hz is sufficient for typical axial flow induced vibration problems in industry.

1. Data Processing

From the volume flow meter reading, the mean flow velocity was calibrated for all achievable controller increments. Figure 3.1-1 shows the mean flow velocity versus the nominal pump shaft speed (half of the controller frequency) with and without the tank. The decrease in the mean flow velocity is due to work done by the pump on the raised head in the tank acting as a reservoir or sink.

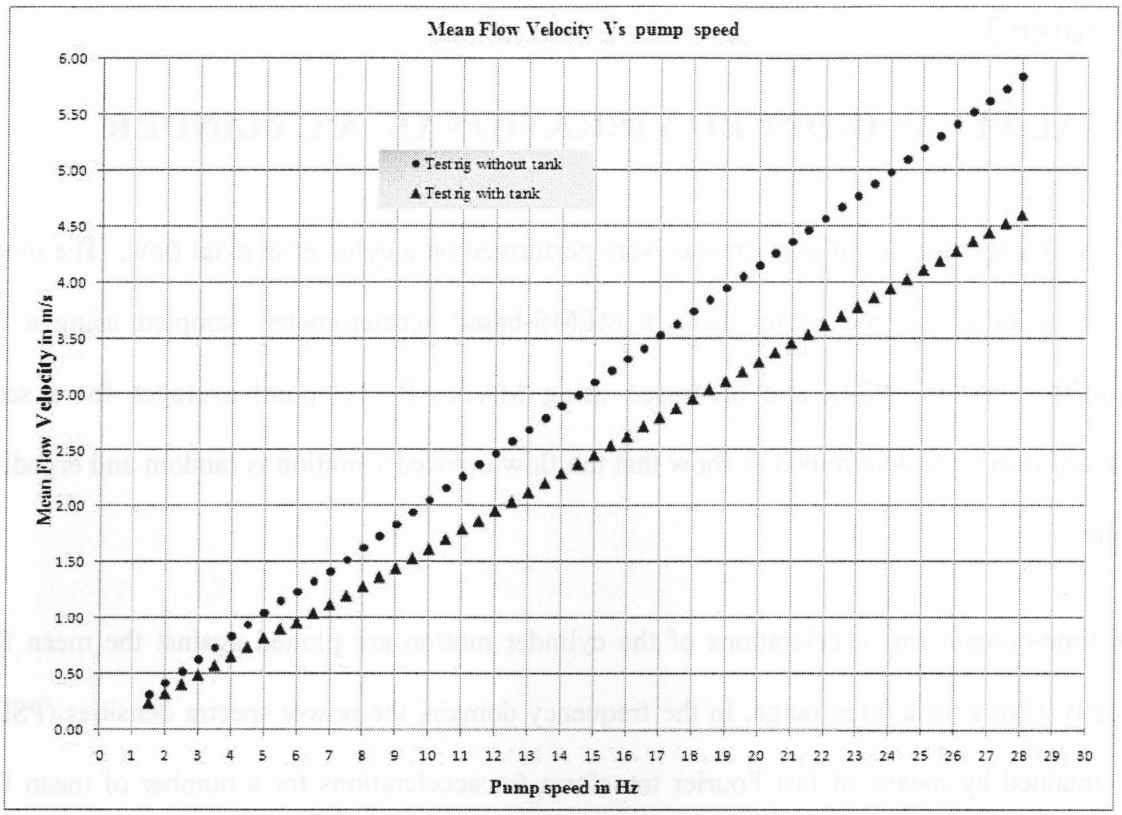

Figure 3.1-1 Flow velocity *vs.* pump speed in the test rig with and without the tank

The Temperature in the test rig filled with lukewarm water was 20°C with a kinematic viscosity (ξ) of 1.004 x 10^{-6} m^2/s in the pipe of 4.0 inch (101.6 mm) diameter. The Reynolds number for the pipe flow ($Re = U^*d_p/\xi$) was 20,000 at a mean flow velocity of 0.2 m/s and 600,000 at a mean flow velocity of 5.9 m/s.

Under the no flow condition, the signals from the accelerometers were recorded to establish a threshold value for noise. It was found that the noise generated by the entire system (including transducer and acquisition system) was ±0.2 mV or ±0.02 m/s^2 in terms of acceleration (= 2 mV * 116.785/1000 $m/s^2/mV$). Figure 3.1-2 shows the equivalent noise threshold. White noise

defined as amplitudes of component waves are all equal and the frequencies of components extend from zero to infinity.

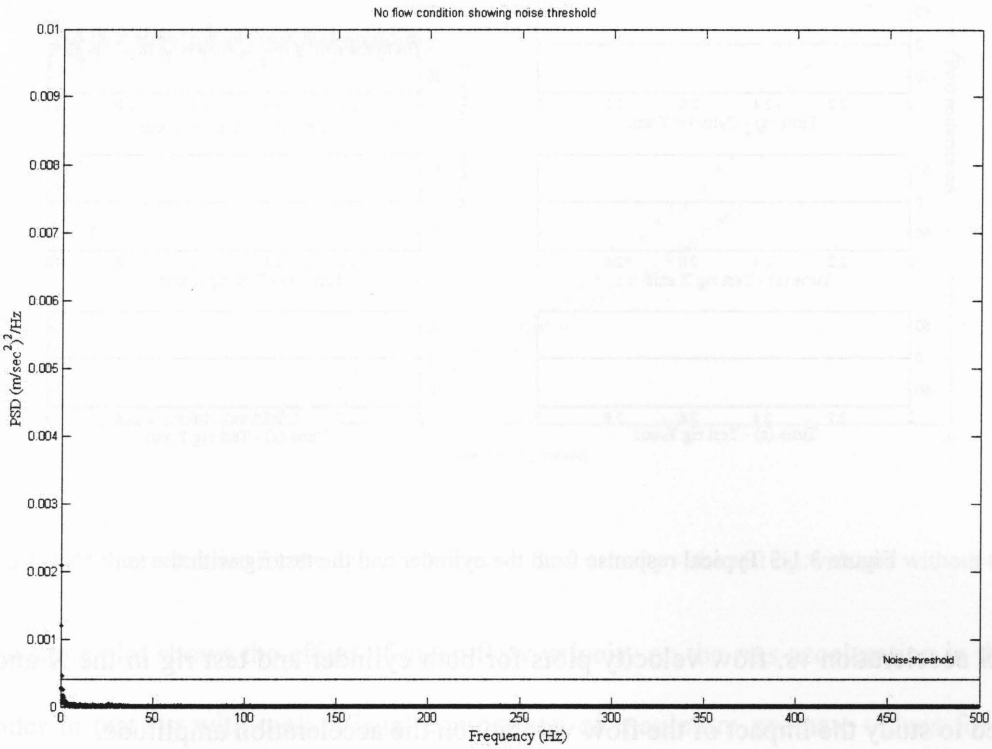

Figure 3.1-2 Establishing noise the threshold

A typical window of time domain signal is presented in Figure 3.1-3 for the cylinder and the test rig for two different flow conditions U = 1.0 m/s (or 5 Hz pump speed) and U = 4.1 m/s (or 20 Hz pump speed). The significant increase in amplitudes at the two different flow velocities can be attributed to the flow turbulence, flow pulsations. Observations show that the response for the cylinder was different in X and Y axes. This was due to the stainless steel strips placed in the Y axis. For the test rig the signal in the X axis (tangential direction) is stronger than that in the Y-axis (radial direction – gravity comes into effect).

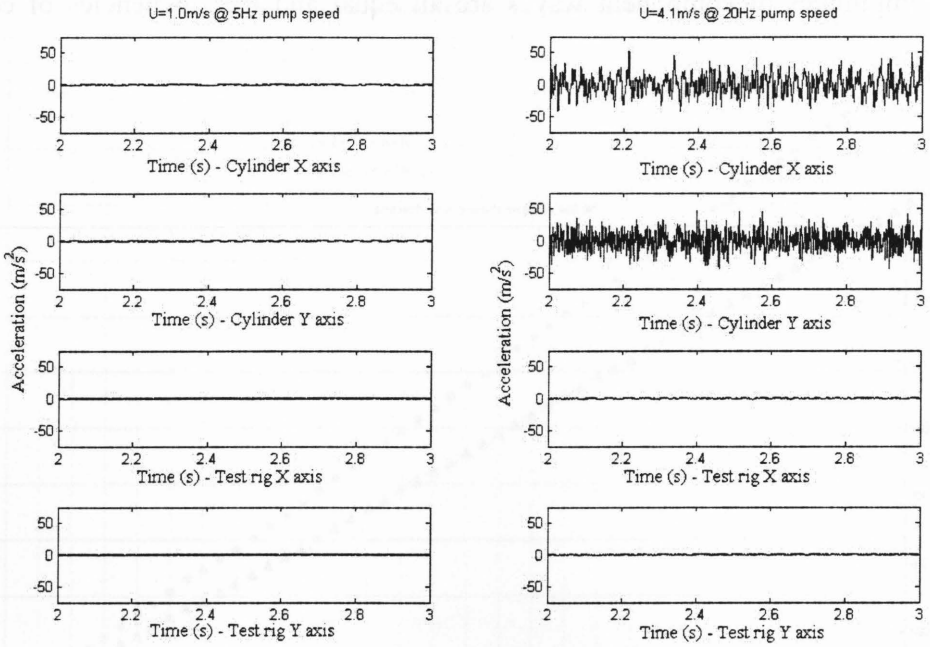

Figure 3.1-3 Typical response from the cylinder and the test rig with the tank

The RMS acceleration *vs.* flow velocity plots for both cylinder and test rig in the X and Y axes are plotted to study the impact of the flow velocity on the acceleration amplitude.

Plot in Figure 3.1-4 shows the effect of mean flow velocity on RMS acceleration in the X axis for cylinder in the test rig with and without tank. In case of test rig without tank when the flow velocity ramping from 1.6 m/s (or 7.5 Hz pump shaft speed) to 2.5 m/s (or 12.5Hz pump shaft speed, there is a spike in the rms response. This phenomenon is caused by the acoustic-structure resonance (2 x 7 x the pump speed, or second harmonics of 7-vane pump). The entire system has a resonant frequency of about 140 Hz.

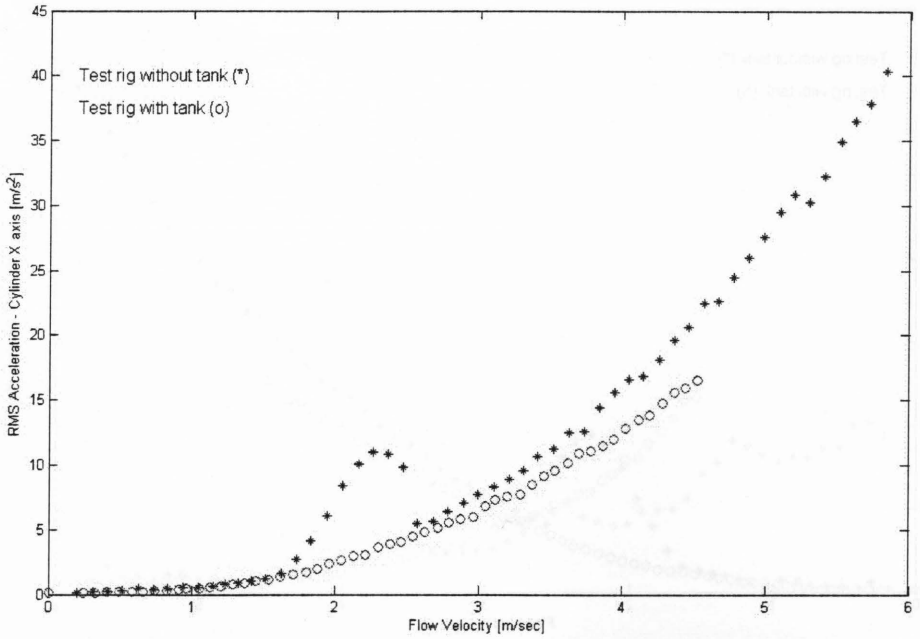

Figure 3.1-4 RMS acceleration for the cylinder X axis *vs.* flow velocity – the test rig with and without the tank

While the same plot shows the effect of mean flow velocity on the rms acceleration in the X axis for cylinder in test rig with tank. Visual comparison of maximum ordinate values for cylinder response in both the configurations of test rig shows mean flow velocity as the driving parameter in increasing the acceleration.

Figure 3.1-5 show the similar behavior as observed above but for the Y axis of cylinder. The maximum ordinate values in these plots are less than that of the X axis due to the reason that cylinder has stainless steel strips embedded in Y axis all along the length increasing flexural rigidity in this axis. This plot for both test rigs with and without tank reiterates the significant contribution of mean flow velocity to the acceleration amplitude of the cylinder.

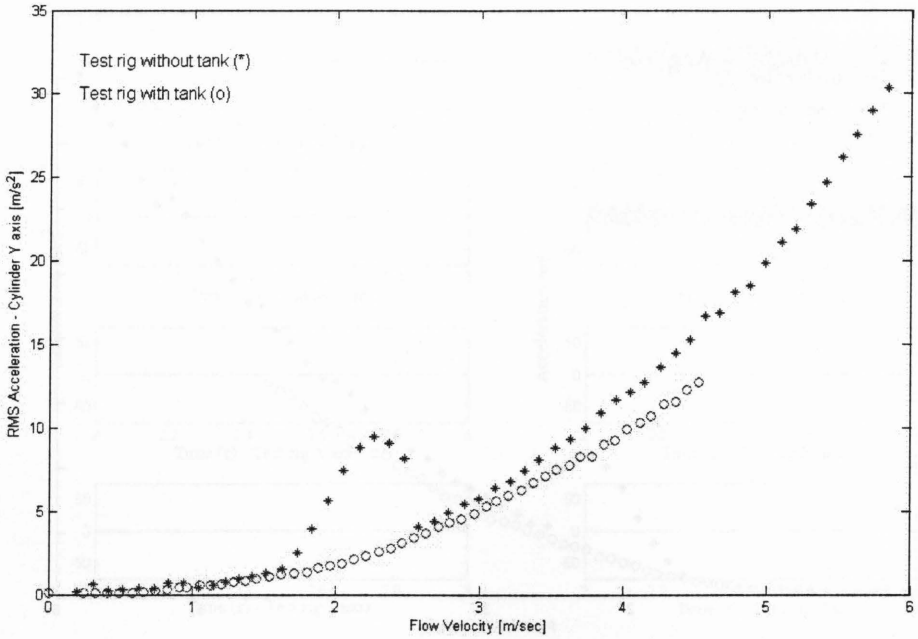

Figure 3.1-5 RMS acceleration for the cylinder Y axis *vs.* flow velocity – the test rig with and without the tank

Figure 3.1-6 and shows test rig response in the X axis for both with tank and without tank configurations. The scale for the ordinate in this plot was much less compared to the flexible cylinder. Test rig without tank has many resonant modes and could be seen from the periodic increase in the rms values all along the flow velocity. The first one occurs when flow velocity was 1.5 m/s and 2.6 m/s. With the test rig re-designed with tank it was seen that the response changed as could be seen in the same plot. The maximum rms value in this system was achieved at a lower flow velocity in comparison with that of test rig without tank. In the process the bump seen in the previous test rig configuration was removed by providing rigid pipe clamps and supports.

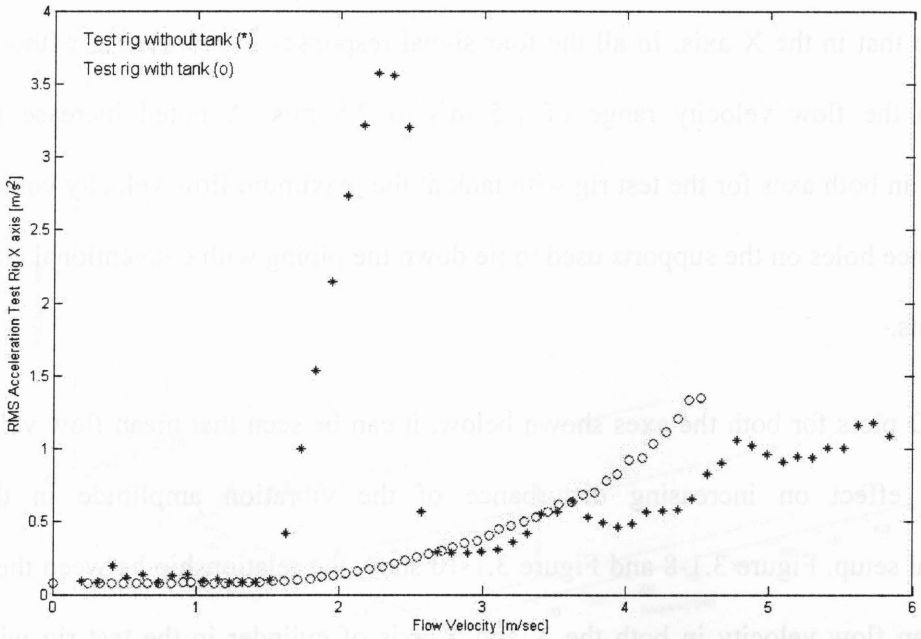

Figure 3.1-6 RMS acceleration for the test rig X axis *vs.* flow velocity – with and without the tank

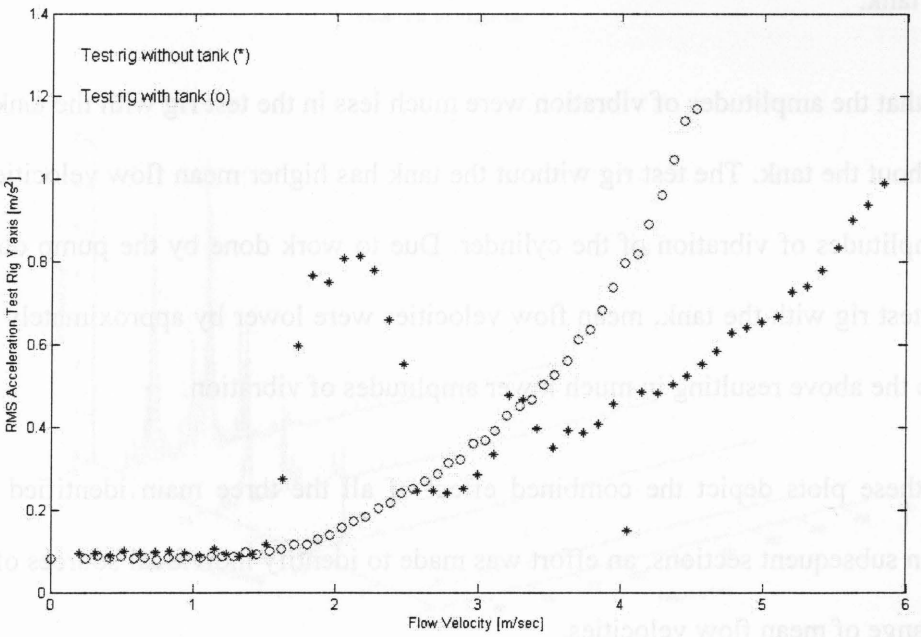

Figure 3.1-7 RMS acceleration for the test rig Y axis *vs.* flow velocity – with and without the tank

The test rig response in the Y axis as shown in Figure 3.1-7 has lower levels of excitation as compared to that in the X axis. In all the four signal responses in the test rig without tank was observed in the flow velocity range of 1.5 m/s to 2.5 m/s. A noted increase in the rms acceleration in both axes for the test rig with tank at the maximum flow velocity could be due to large clearance holes on the supports used to tie down the piping with conventional clamps using bolts and nuts.

From the 3D plots for both the axes shown below, it can be seen that mean flow velocity has a pronounced effect on increasing disturbance of the vibration amplitude in the current experimental setup. Figure 3.1-8 and Figure 3.1-10 show the relationship between the amplitude and the mean flow velocity in both the X and Y axis of cylinder in the test rig without tank. Figure 3.1-9 and Figure 3.1-11 show the similar effects of the mean flow velocity on the acceleration amplitude on a linear scale FFT in the frequency domain for the cylinder in the test rig with the tank.

It was seen that the amplitudes of vibration were much less in the test rig with the tank compared to those without the tank. The test rig without the tank has higher mean flow velocities resulting in larger amplitudes of vibration of the cylinder. Due to work done by the pump on the raised head in the test rig with the tank, mean flow velocities were lower by approximately 27% when compared to the above resulting in much lower amplitudes of vibration.

So far, all these plots depict the combined effect of all the three main identified sources of excitation. In subsequent sections, an effort was made to identify individual sources of excitation for a wide range of mean flow velocities.

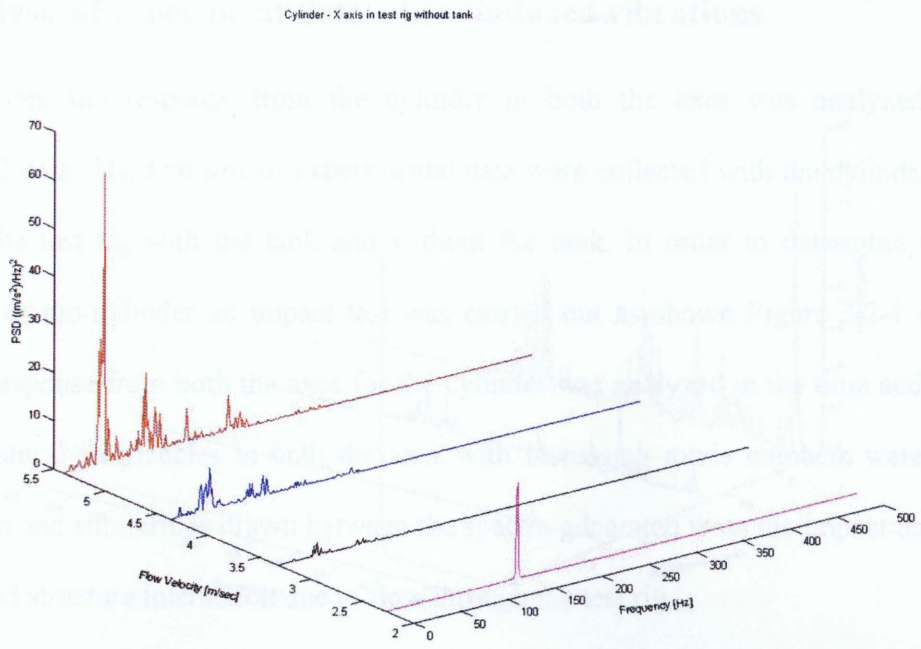

Figure 3.1-8 Effect of flow velocity on the vibration amplitude in the X axis – the test rig without the tank

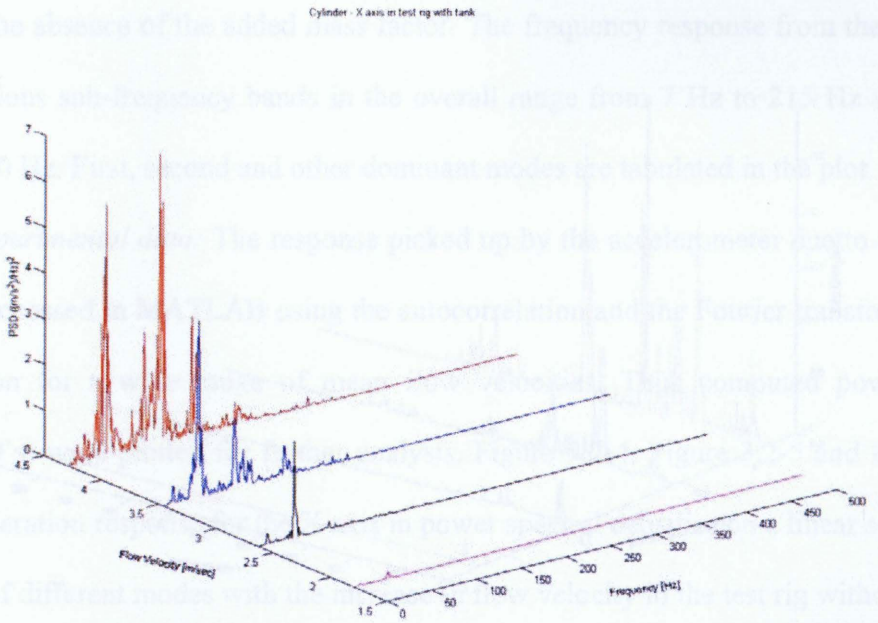

Figure 3.1-9 Effect of flow velocity on the vibration amplitude in the X axis – the test rig with the tank

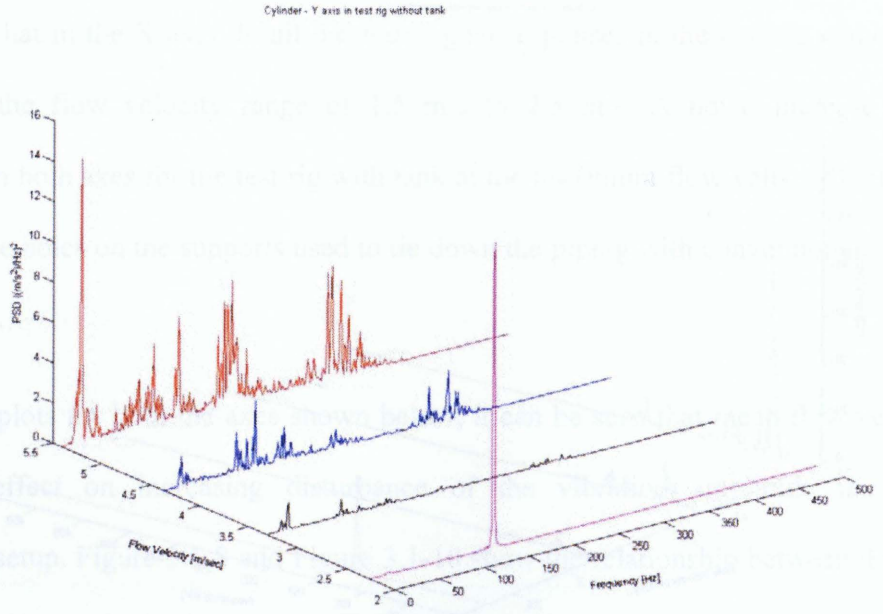

Figure 3.1-10 Effect of flow velocity on the vibration amplitude in the Y axis – the test rig without the tank

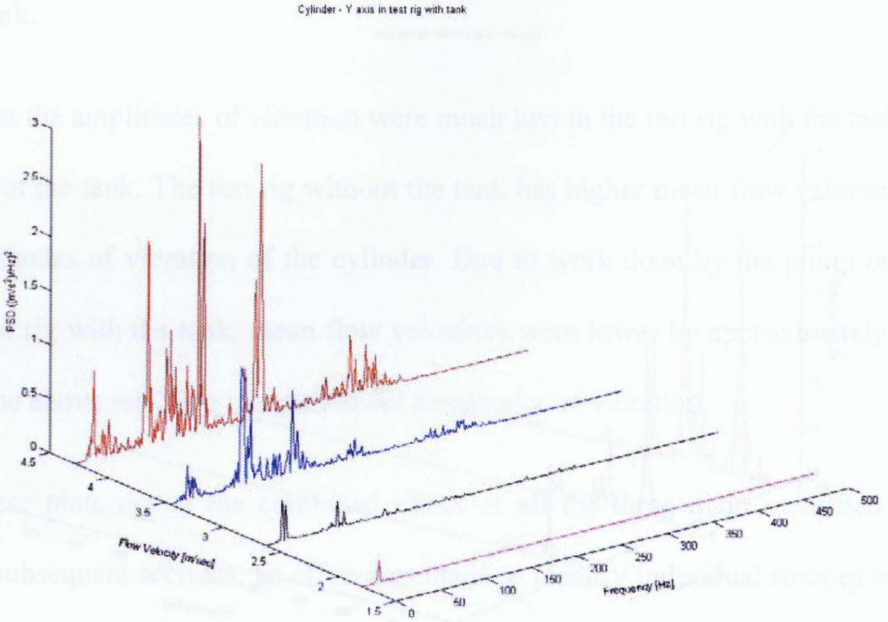

Figure 3.1-11 Effect of flow velocity on the vibration amplitude in the Y axis – the test rig with the tank

3.2. Analysis of experiment data – flow induced vibrations

In this section, the response from the cylinder in both the axes was analyzed from the experimental data. The two sets of experimental data were collected with the cylinder subjected to FIV in the test rig with the tank and without the tank. In order to determine the natural frequencies of the cylinder an impact test was carried out as shown Figure 3.2-1 and Figure 3.2-2. The response from both the axes for the cylinder was analyzed in the time and frequency domains. Natural frequencies in both the axes with increasing mode numbers were identified from this test and similarities drawn between the spectra generated from the impact data and that from the fluid structure interaction due to flow through the test rig.

3.2.1. Cylinder X-axis

Analysis of impact test data: The Fourier transform of the impact data for the acceleration in the X axis is shown in Figure 3.2-3 and it is clear that resonant frequencies are higher than those in water due to the absence of the added mass factor. The frequency response from the impact test shows the various sub-frequency bands in the overall range from 7 Hz to 215 Hz with a weak response at 300 Hz. First, second and other dominant modes are tabulated in the plot.

Analysis of experimental data: The response picked up by the accelerometer due to the cylinder motion was processed in MATLAB using the autocorrelation and the Fourier transform function for acceleration for a wide range of mean flow velocities. Thus computed power spectral densities (PSD's) were plotted for further analysis. Figure 3.2-4, Figure 3.2-5 and Figure 3.2-6 show the acceleration response for the X axis in power spectral densities on a linear scale and the development of different modes with the increase in flow velocity in the test rig without the tank. These plots show the effect of turbulence (flow induced) on the approximate modal behavioral dynamics that change from first mode to higher harmonics.

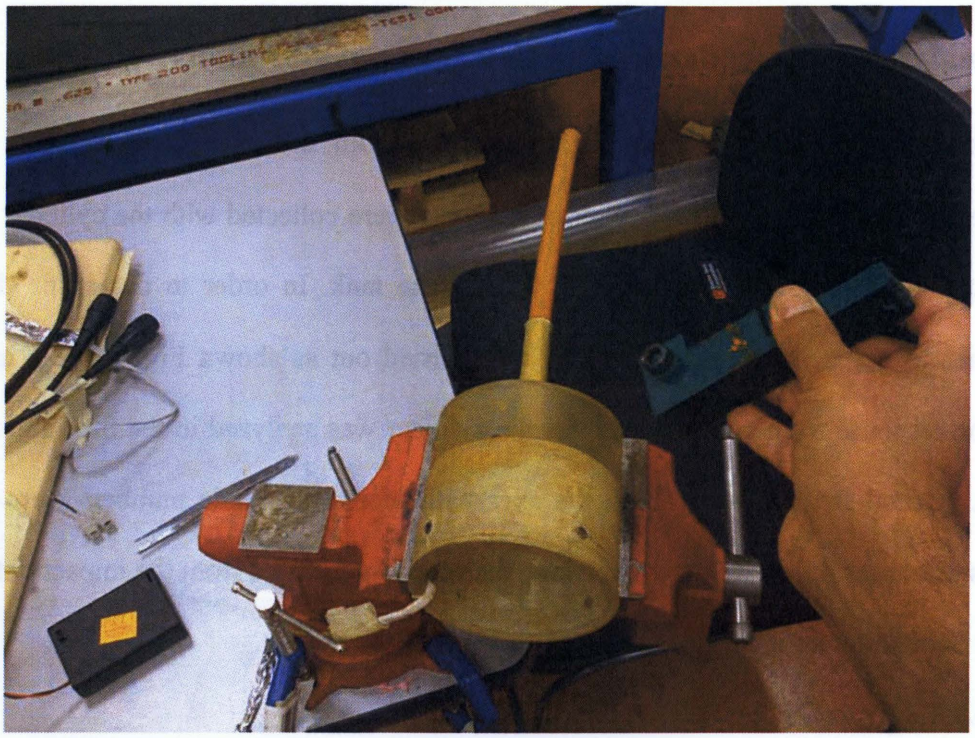

Figure 3.2-1 Impact test arrangement-1 for the cantilever cylinder

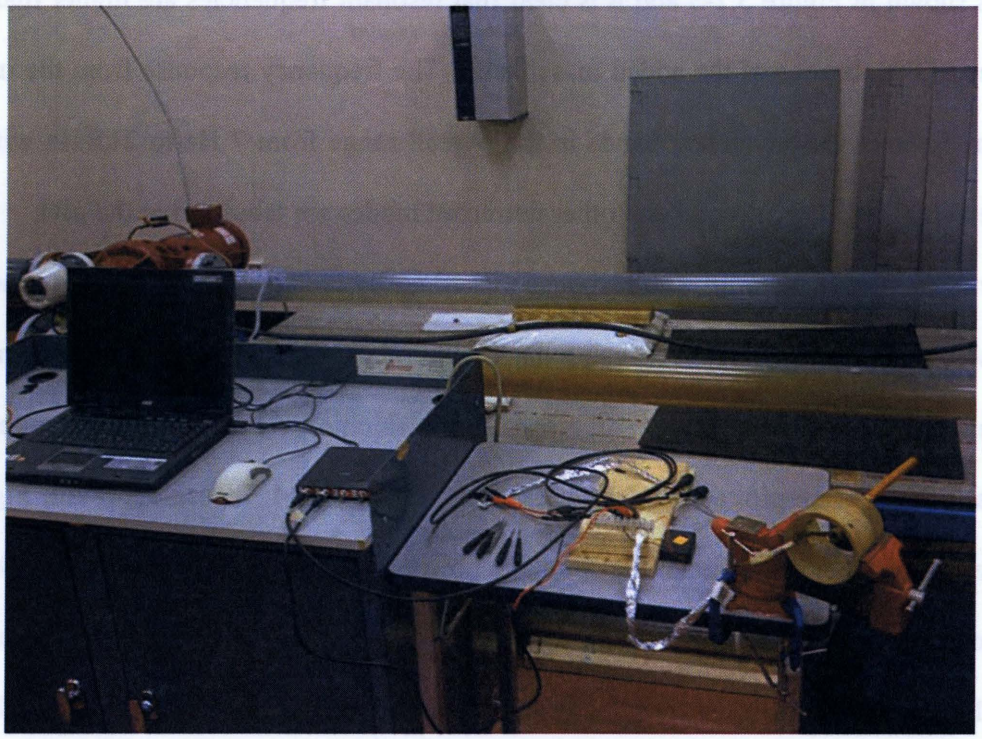

Figure 3.2-2 Impact test arrangement-2 for the cantilever cylinder

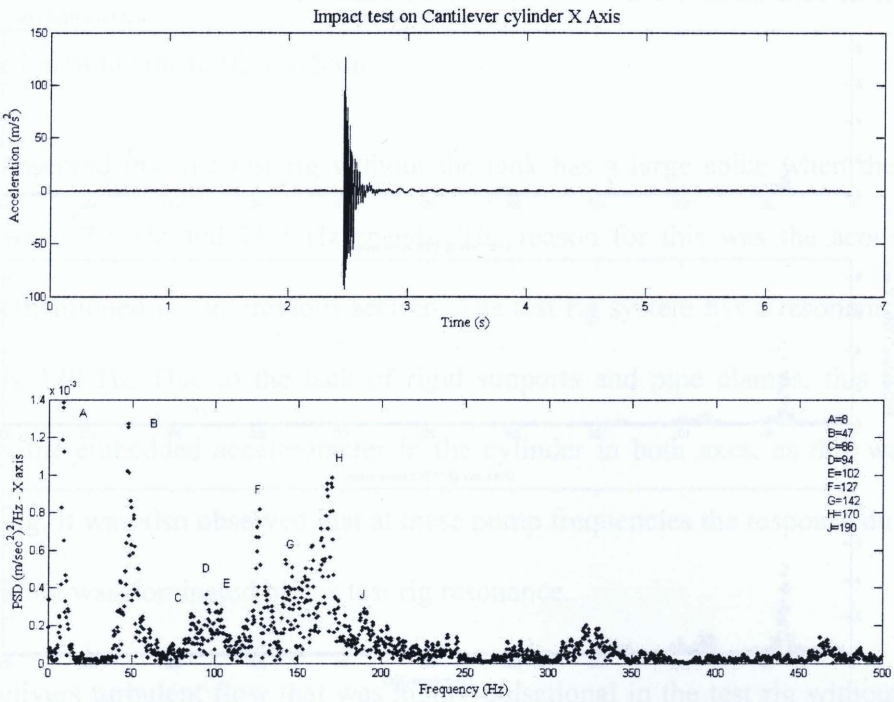

Figure 3.2-3 Cylinder-impact test results in the X axis

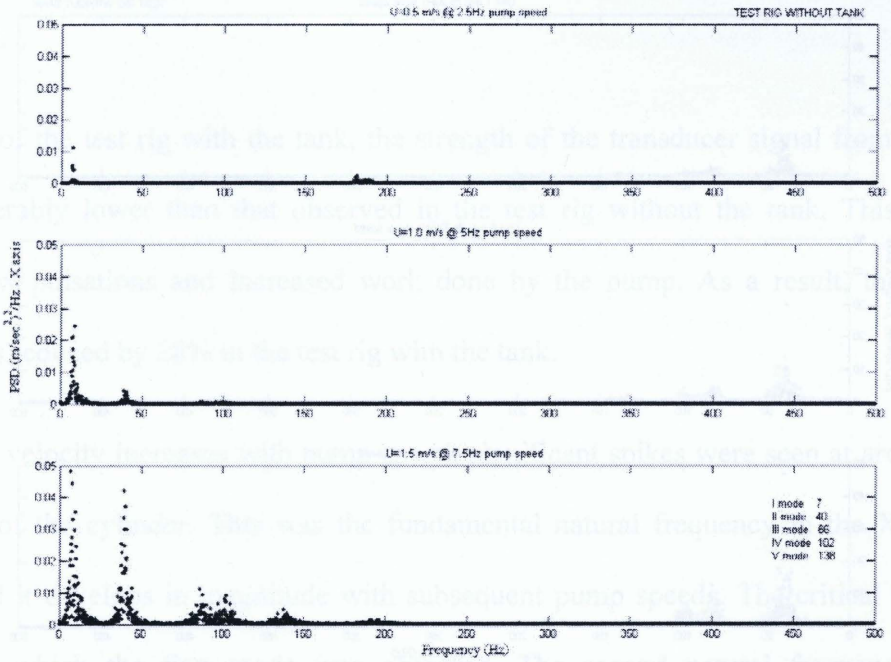

Figure 3.2-4 Cylinder X axis response in the test rig without the tank up to U = 1.5 m /s

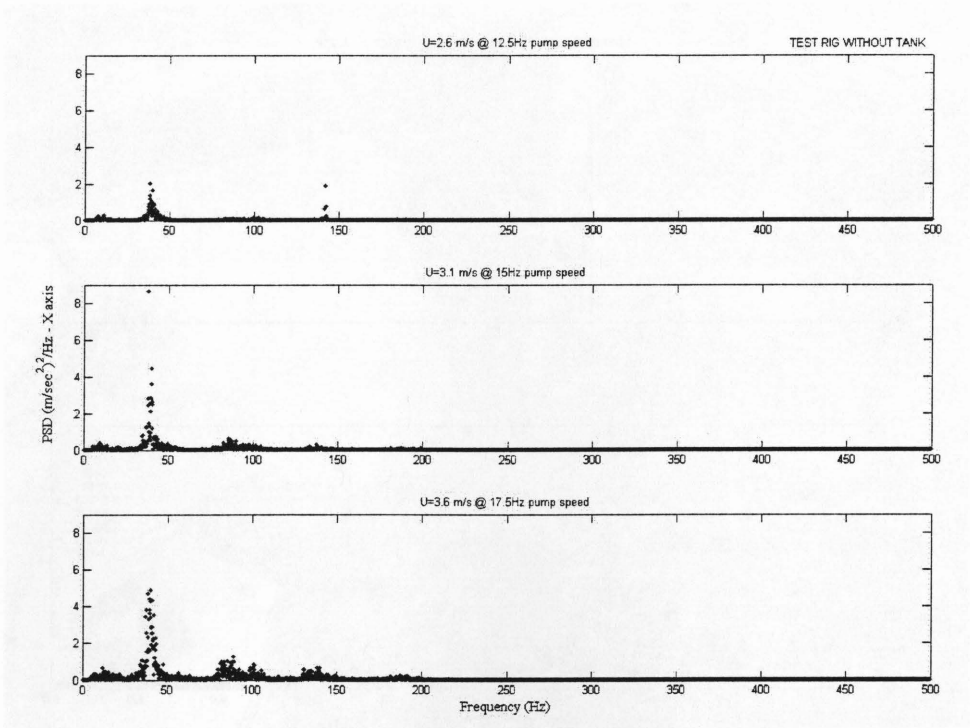

Figure 3.2-5 Cylinder X axis response in the test rig without the tank up to U = 3.6 m /s

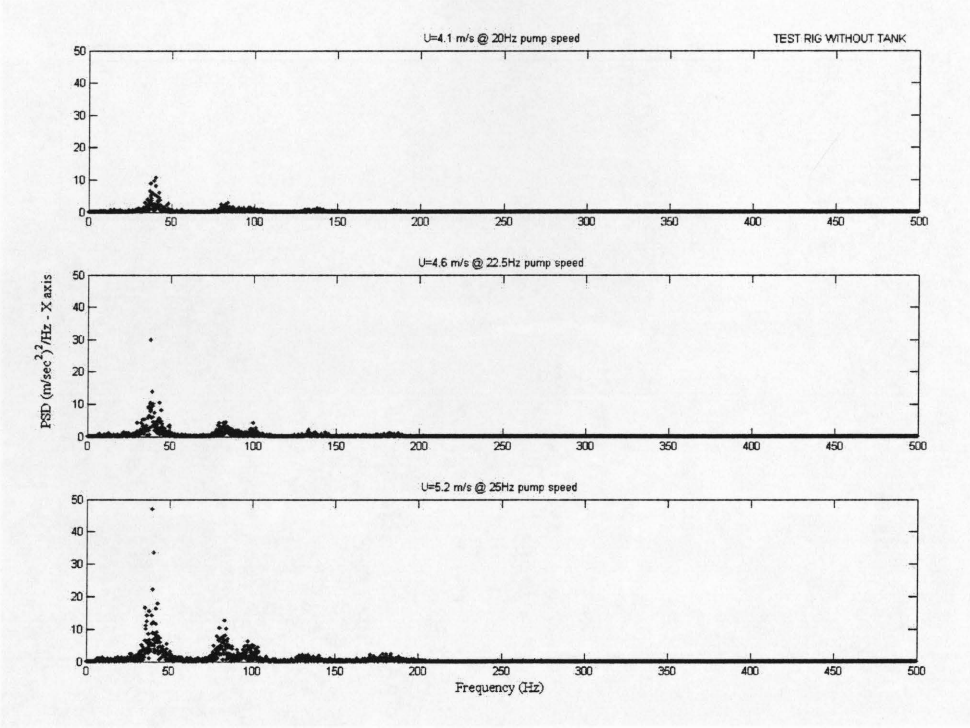

Figure 3.2-6 Cylinder X axis response in the test rig without the tank up to U = 5.2 m /s

The magnitudes of these modal amplitudes were dependent on the turbulence in flow which in turn is a function of the mean flow velocity.

It was also observed that the test rig without the tank has a large spike when the pump shaft operates between 7.5 Hz and 12.5 Hz speeds. The reason for this was the acoustic-structure resonance as mentioned in the previous section. The test rig system has a resonant frequency of approximately 140 Hz. Due to the lack of rigid supports and pipe clamps, this response was picked up by the embedded accelerometer in the cylinder in both axes, as this was integrated with the test rig. It was also observed that at these pump frequencies the response due to the flow induced vibration was dominated by the test rig resonance.

The pump delivers turbulent flow that was highly pulsational in the test rig without the tank. It was observed from the acceleration plots that the blade passing frequencies were dominant till the 20 Hz pump speed. The pump shaft frequency was strong and noticeable beyond the 20 Hz pump speed.

In the case of the test rig with the tank, the strength of the transducer signal from the cylinder was considerably lower than that observed in the test rig without the tank. This was due to reduced flow pulsations and increased work done by the pump. As a result, the mean flow velocity was reduced by 28% in the test rig with the tank.

As the flow velocity increases with pump speed, significant spikes were seen at around 7 Hz in the X axis of the cylinder. This was the fundamental natural frequency in the X axis of the cylinder and it develops in magnitude with subsequent pump speeds. The critical velocity was 0.4 m/s, at which the first mode was observed. The second natural frequency was seen developing in the X axis of the cylinder at 40 Hz, its magnitude increases with the increase in

flow velocity. The critical velocity was observed to be 0.7 m/s when the second natural frequency was observed. Close observation of modal dynamics in these plots shows that the second mode takes over the first at a flow velocity of 1.6m/s while higher modes develop and dominate in magnitude as the flow velocity increases.

The third mode was observed to be around 86 Hz at a critical flow velocity of 1.15 m/s. The fourth mode at 102 Hz was observed at a critical velocity of 1.23 m/s. The fifth mode was observed around 138 Hz at critical velocity of 1.4 m/s. Around 196 Hz, the sixth mode was observed at a critical velocity of 1.5 m/s. The amplitudes of these six dominant modes increase with the increase in the flow velocity.

Figure 3.2-7, Figure 3.2-8 and Figure 3.2-9 show the evolution of different modes of cylinder in X axis caused by turbulent flow in test rig with the tank. As the mean flow velocity increases the trend shifts from first mode to second and third resonant frequencies. At low mean flow velocities, the energy was concentrated in the first and second modes. At high mean flow velocities, the maximum concentration of energy was noticed in second, third and fourth modes. Again close observation of these figures shows the concentration of energy by a factor of 5 times in the test rig without the tank to that of the test rig with the tank. From the above analysis, the effect of mean flow velocity and hence turbulence on excitation of the higher resonant frequencies can be seen.

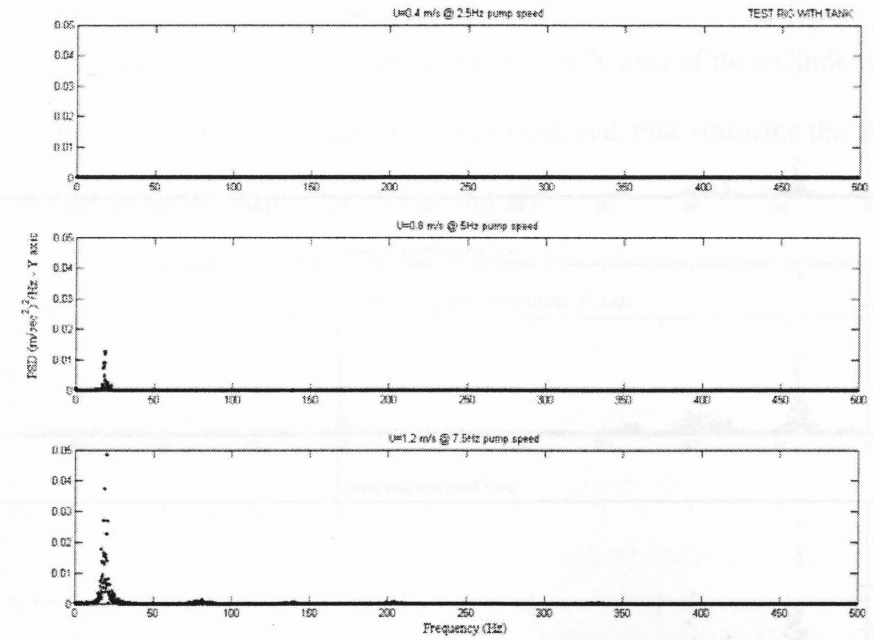

Figure 3.2-7 Cylinder X axis response in the test rig with the tank up to U = 1.2 m /s

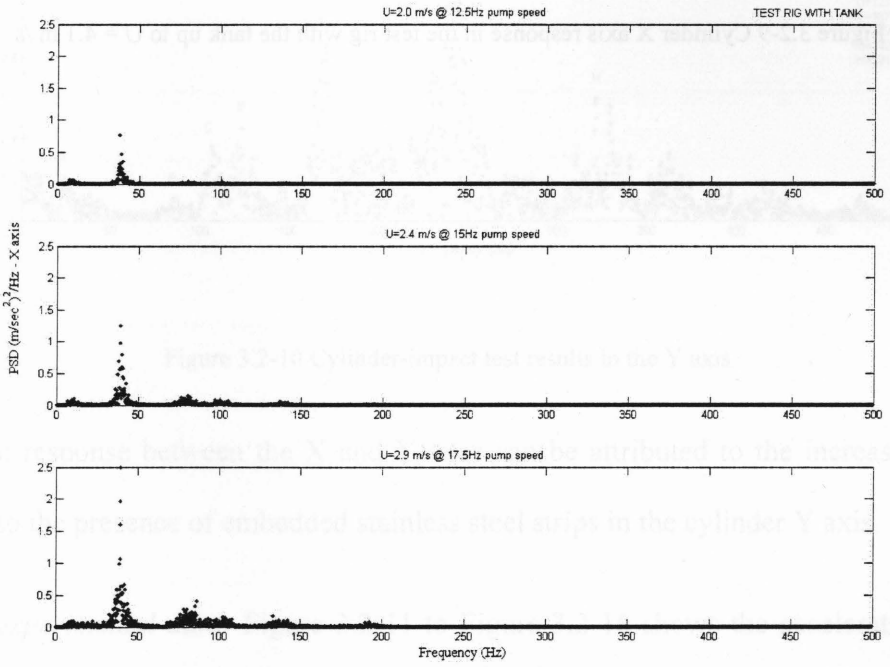

Figure 3.2-8 Cylinder X axis response in the test rig with the tank up to U = 2.9 m /s

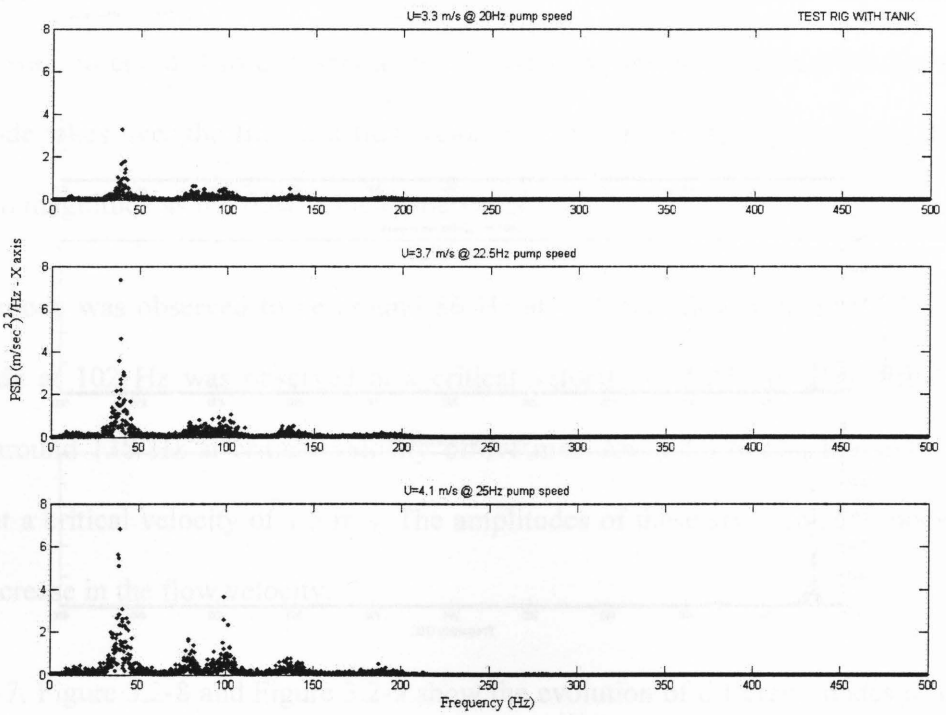

Figure 3.2-9 Cylinder X axis response in the test rig with the tank up to U = 4.1 m /s

3.2.2. Cylinder Y-Axis

Analysis of impact test data: The impact test results for the Y axis of the cylinder in the time and frequency domain shown in Figure 3.2-10. It was observed that resonant the frequencies are embedded in a wide frequency band of 20 Hz to 300 Hz.

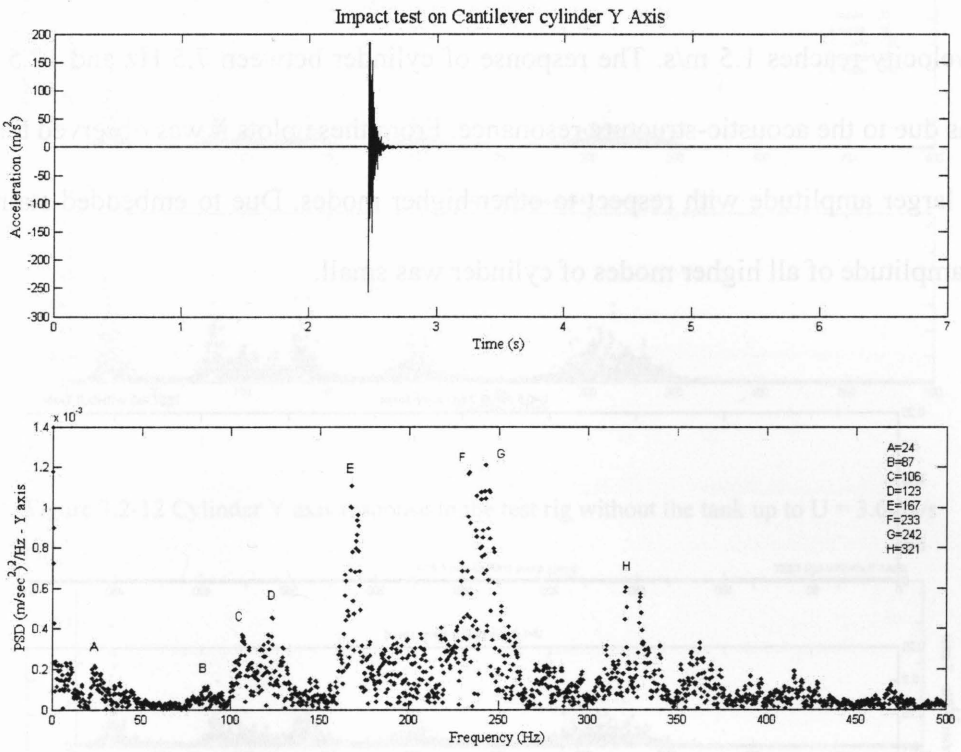

Figure 3.2-10 Cylinder-impact test results in the Y axis

The offset in response between the X and Y axes can be attributed to the increase in flexural rigidity due to the presence of embedded stainless steel strips in the cylinder Y axis.

Analysis of experimental data: Figure 3.2-11 to Figure 3.2-16 shows the acceleration response over the entire flow velocity spectrum in both test rigs with and without the tank. These plots show identical response with an exception that the magnitude in the test rig without the tank is higher than the test rig with the tank.

At flow velocity of 0.6 m/s the onset of first resonant frequency in the Y axis of cylinder which is at 20 Hz was noticed and its magnitude increases as the flow velocity increases. With flow velocity reaching 1.0 m/s the second mode occurs at 86 Hz just above the threshold noise level. When the flow reaches 1.3 m/s three more modes at ~ 133 Hz, 201 Hz and 310 Hz make their appearance above the noise threshold level. First mode peak amplitude attains maximum when the flow velocity reaches 1.5 m/s. The response of cylinder between 7.5 Hz and 12.5 Hz pump speeds was due to the acoustic-structure resonance. From these plots it was observed that the first mode has larger amplitude with respect to other higher modes. Due to embedded stainless steel strips the amplitude of all higher modes of cylinder was small.

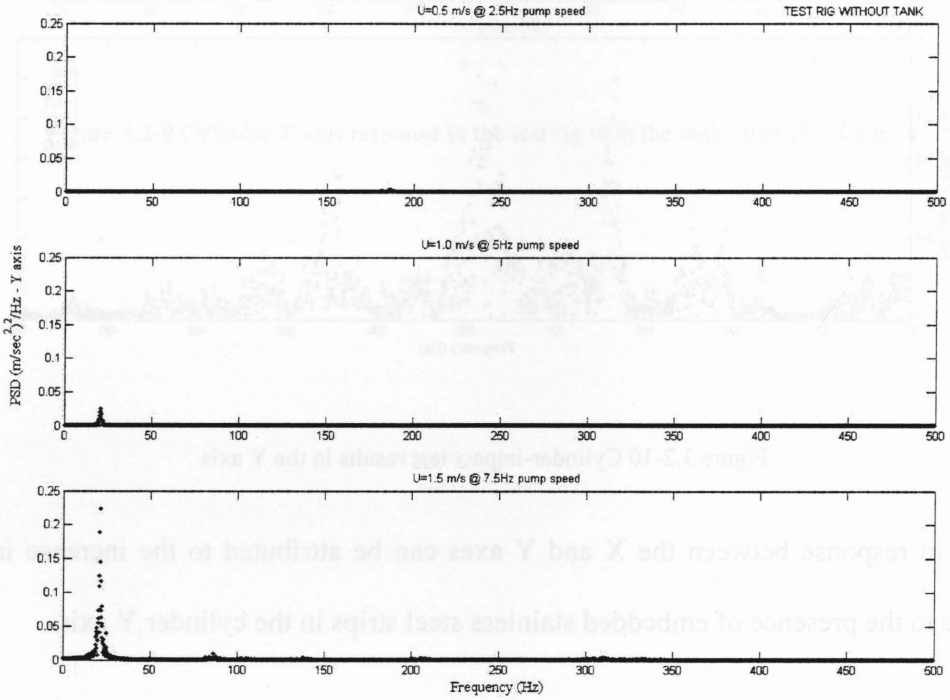

Figure 3.2-11 Cylinder Y axis response in the test rig without the tank up to U = 1.5 m /s

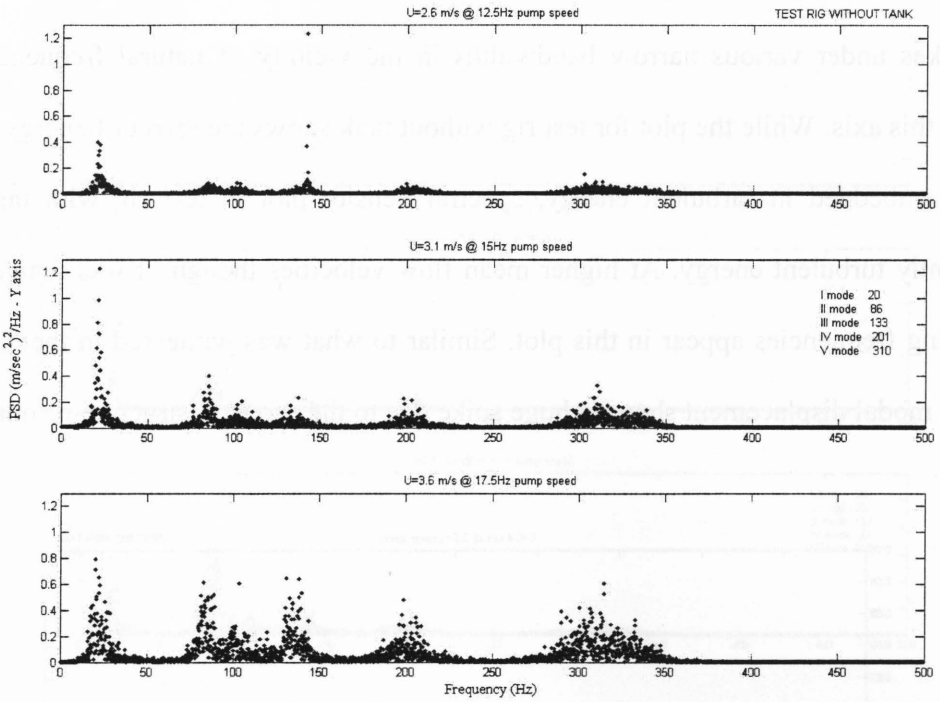

Figure 3.2-12 Cylinder Y axis response in the test rig without the tank up to U = 3.6 m /s

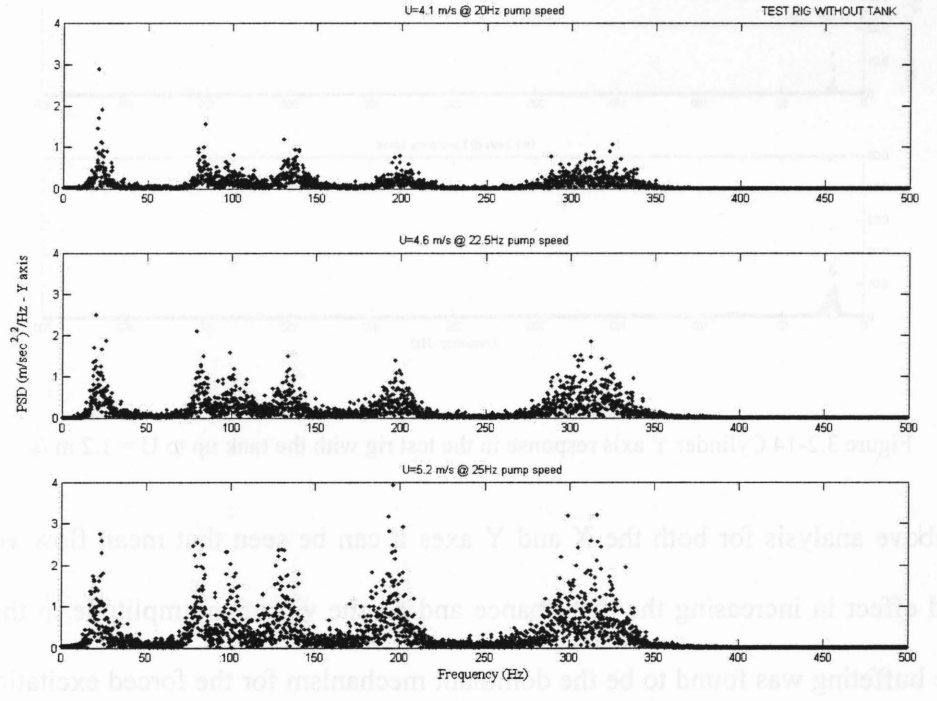

Figure 3.2-13 Cylinder Y axis response in the test rig without the tank up to U = 5.2 m /s

Once again the flow pulsations play a dominant role as can be seen from the accumulation of energy spikes under various narrow bandwidths in the vicinity of natural frequencies of the cylinder in this axis. While the plot for test rig without tank shows the effect of energy from flow pulsations embedded in turbulent energy, spectral density plot in test rig with tank reflects predominantly turbulent energy. At higher mean flow velocities though, it was noticed that the blade passing frequencies appear in this plot. Similar to what was witnessed in the X axis; at ~ 135 Hz the modal displacement shows a huge spike due to the acoustic-structure resonance.

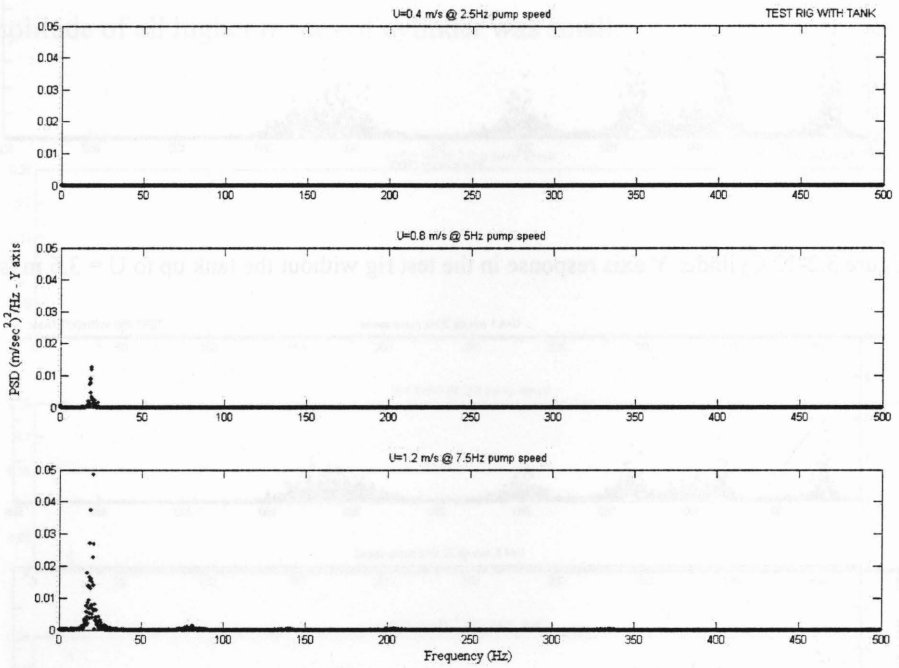

Figure 3.2-14 Cylinder Y axis response in the test rig with the tank up to U = 1.2 m /s

From the above analysis for both the X and Y axes it can be seen that mean flow velocity has pronounced effect in increasing the disturbance and on the vibration amplitude in the cylinder. Turbulence buffeting was found to be the dominant mechanism for the forced excitations in both the X and Y axes of cylinder in both the test rig configurations.

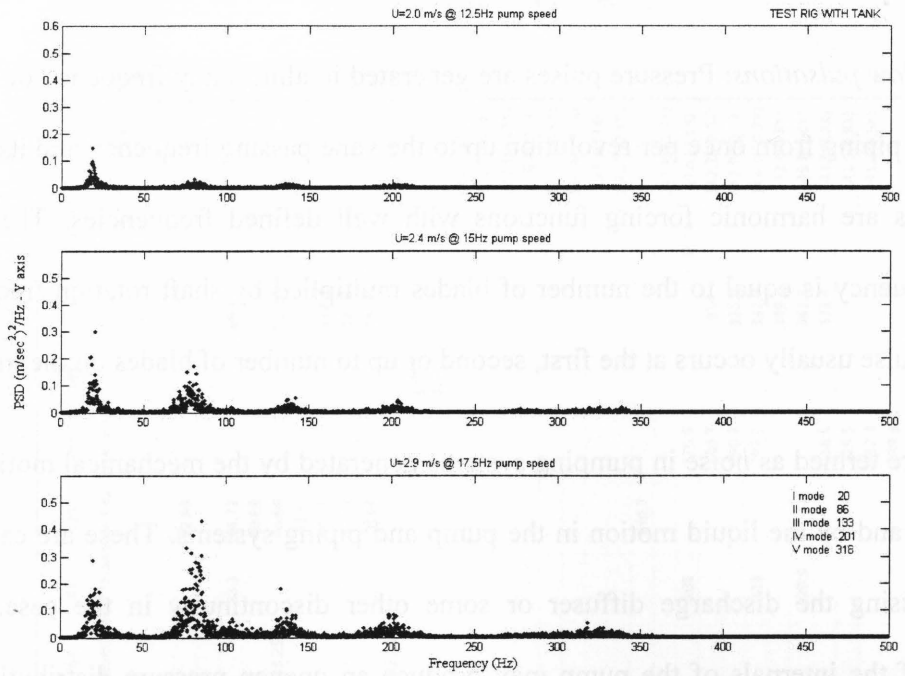

Figure 3.2-15 Cylinder Y axis response in the test rig with the tank up to U = 2.9 m /s

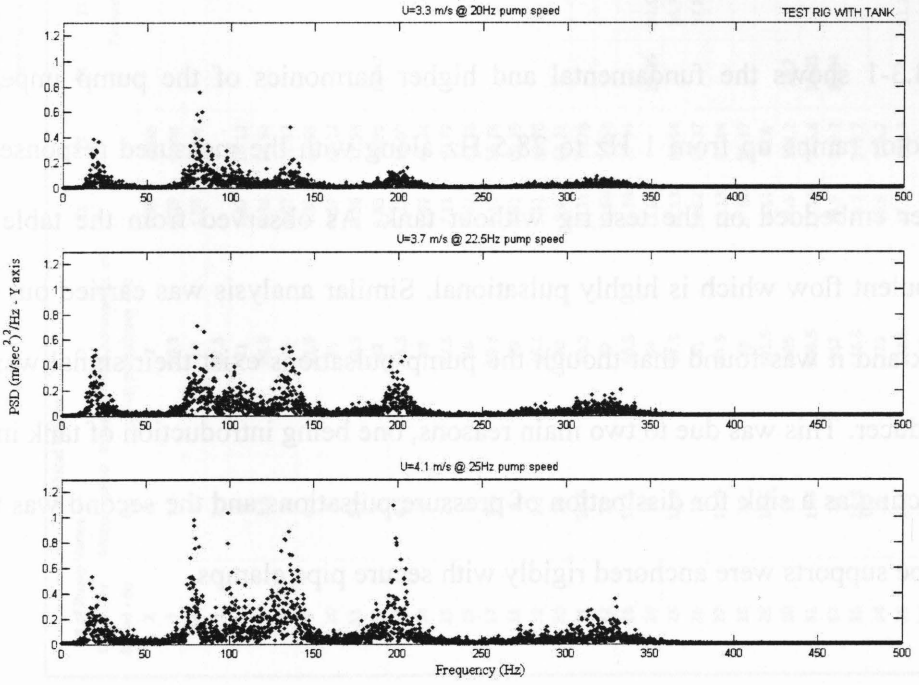

Figure 3.2-16 Cylinder Y axis response in the test rig with the tank up to U = 4.1 m /s

3.3. Flow pulsations - test rig response

Sources of flow pulsations: Pressure pulses are generated in almost any frequency of vibration of the pump or piping from once per revolution up to the vane passing frequency and its harmonics. These pulses are harmonic forcing functions with well defined frequencies. The first blade passing frequency is equal to the number of blades multiplied by shaft rotation frequency. The prominent pulse usually occurs at the first, second or up to number of blades on the impeller.

Pulsations are termed as noise in pumping systems generated by the mechanical motion of pump components and by the liquid motion in the pump and piping systems. These are caused by the impeller passing the discharge diffuser or some other discontinuity in the case. Any non-symmetry of the internals of the pump may produce an uneven pressure distribution that can result in forces applied to the rotor there by causing unbalance in shaft rotation thereby generating pressure pulses [15].

The Table-3.3-1 shows the fundamental and higher harmonics of the pump impeller as the induction motor ramps up from 1 Hz to 28.5 Hz along with the measured responses from the accelerometer embedded on the test rig without tank. As observed from the table the pump delivers turbulent flow which is highly pulsational. Similar analysis was carried out on the test rig with tank and it was found that though the pump pulsations exist their signal was too weak for the transducer. This was due to two main reasons, one being introduction of tank in to the test rig system acting as a sink for dissipation of pressure pulsations and the second was the test rig pipes and pipe supports were anchored rigidly with secure pipe clamps.

Table-3.3-1 Theoretical pump shaft speed and higher harmonics *vs.* experiment values – the test rig without the tank

Flow Pulsations - Test Rig without tank
theoritical vs. experimental values

Theoritical Values																
# of Pump Vanes -->		7	1X	7X	2X	3X	4X	5X	6X	8X	12X	14X	18X	24X	28X	
Controller Speed - Hz	Motor speed - Hz.	Impeller vane harmonics or pump pulsations - Hz	Experimental Data reading predominantly 7X and back calculating 1X													Non integer
2	1	7	0.89	none												
3	1.5	10.5	1.39	none												
4	2	14	1.88	none							22.65					
5	2.5	17.5														
6	3	21	2.87	20.12						23.1	34.72			69.29		
7	3.5	24.5	3.36	23.54							40.68					
8	4	28	3.87	27.12					23.25		46.64			93.28		
9	4.5	31.5	4.36	30.55							52.6					
10	5	35	4.87	34.12							58.71			117.3		
11	5.5	38.5	5.36	37.55			21.46				64.67			129.3		
12	6	42	5.85	40.98	11.47		23.4				70.63			141.3		
13	6.5	45.5	6.15	43.07					37.25							
14	7	49	6.62	46.34									119.1			
15	7.5	52.5	7.11	49.77				36.96					129.3			
16	8	56	7.62	53.35												133.7 (17.5X)
17	8.5	59.5	8.11	56.78												135.2(16.7X)
18	9	63	8.62	60.35												136.1(15.8X)
19	9.5	66.5	9.11	63.78												136.8(15X)
20	10	70	9.6	67.21												137.7(14.3X)
21	10.5	73.5	10.11	70.78												138.6(13.7X)
22	11	77	10.64	74.51												139.3(13X)
23	11.5	80.5	11.13	77.94												140.7(12.6X)
24	12	84	11.62		23.25	34.87					140.7					
25	12.5	87.5	12.13	84.94		36.36										141.9(11.7X)
26	13	91	12.62	88.37		37.85	50.52			101		176.6			353.6	142(12.6X)
27	13.5	94.5	13.13	91.94			52.45					183.7		314		142.2(10.8X)
28	14	98	13.62	95.37								190.7		325.9		142.9(10.5X)
29	14.5	101.5	14.11	98.8			56.48			113		197.6		337.7		144.4(10.2X)
30	15	105	14.6	102.2	29.2		58.4							349.6		143.4(9.8X)
31	15.5	108.5	15.11	105.8	30.25		60.5			120.9				361.5		145.6(9.6X)
32	16	112	15.6	109.2	31.14							218.5		373.4		143.8(9.2X)
33	16.5	115.5	16.1	112.7			64.37					225.5				141.6(8.8X)
34	17	119	16.6	116.2			67.5					232.3				141.3(8.5X)
35	17.5	122.5	17.1	119.7		51.26						239.3				
36	18	126	17.58	123.1	36.21	52.75	71.53			141.3		246.3				
37	18.5	129.5	18.07	126.5	36.21	54.24						253				

Flow Pulsations - Test Rig without tank
theoritical vs. experimental values

Theoritical Values															
# of Pump Vanes -->		7	1X	7X	2X	3X	4X	5X	6X	8X	12X	14X	18X	24X	28X	
Controller Speed - Hz	Motor speed - Hz.	Impeller vane harmonics or pump pulsations - Hz	Experimental Data reading predominantly 7X and back calculating 1X													Non integer
38	19	133	18.55	129.9	37.11	55.73				147.8		259.9				
39	19.5	136.5	19.05	133.4	38.15	57.07			114.3		232.6					
40	20	140	19.54	136.8	39.04	58.56		100.4	119.2							
41	20.5	143.5	20.01	140.1		60.05			120.1							
42	21	147	20.5	143.5	40.98	61.54			123.1							
43	21.5	150.5	20.98	146.9		63.03						293.9				
44	22	154	21.48	150.4		64.37										
45	22.5	157.5	21.97	153.8		65.87										
46	23	161	22.45	157.2		67.36										
47	23.5	164.5	22.94	160.6		68.85										
48	24	168	23.44	164.1		70.34			140.4	187.5		328				
49	24.5	171.5	23.93	167.5		71.68		118	143.5	191.3						
50	25	175	24.41	170.9		73.17		122								
51	25.5	178.5	24.9	174.3	49.77	74.66										
52	26	182	25.4	177.8	50.81	76.15										
53	26.5	185.5	25.88	181.2	51.71	77.64										
54	27	189	26.37	184.6	52.75	79.13	105.5									
55	27.5	192.5	26.87	188.1	53.65		107.4									
56	28	196	27.35	191.5	54.69		109.4									
57	28.5	199.5	27.84	194.9	55.73		111.3									

Table-3.3-1 contd.

3.3.1. Test rig without and with the tank – X axis:

From the Table-3.3-1 it was seen that the measured first blade passing frequency was lagging behind its theoretical counterpart. This can be explained as the combined effect of load on the pump shaft and frequency resolution in data processing. The frequency resolution in the present experiment was 0.15 Hz with a sampling rate of 10,000 Hz and a record length of 131,072 samples.

The experimental shaft frequency was back calculated by dividing the measured first blade passing frequency with number of vanes (in this case the pump impeller has 7 vanes). The reason for back calculating the shaft frequency was due to the dominant first blade passing frequency at all the shaft speeds during entire experiment in test rig without tank. At various mean flow velocities Fourier transform for acceleration showed dominant peaks. The subsequent columns on the experiment side in the table explain the measured shaft frequency and its multiples.

From 1 Hz to 14 Hz theoretical pump speed as shown in Figure 3.3.1-1 the shaft frequency was not as dominant as compared to the first blade passing frequency. While from 15 Hz to 28 Hz theoretical pump speed the signal for measured shaft frequency, 2X, 3X, 4X, 5X, 6X, 7X and higher multiples of shaft frequency were quite strong depicting the pulsational nature of flow.

Between 7.5 Hz and 12.5 Hz the test rig has acoustic-structure resonance at around 140 Hz as identified in previous sections. As the pump speed increases the flow pulses were observed in the test rig at all the blade passing frequencies and their harmonics.

The flow pulsations from the pump rotation and blade passing frequencies were significantly lower in the test rig with tank as seen in Figure 3.3.1-2.

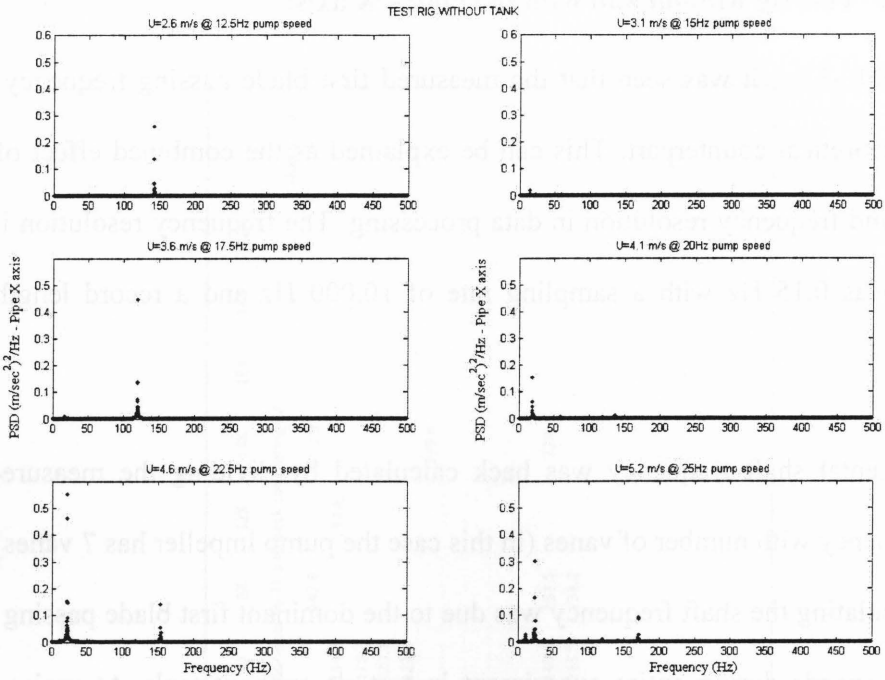

Figure 3.3.1-1 Response from the test rig in the X axis – without the tank

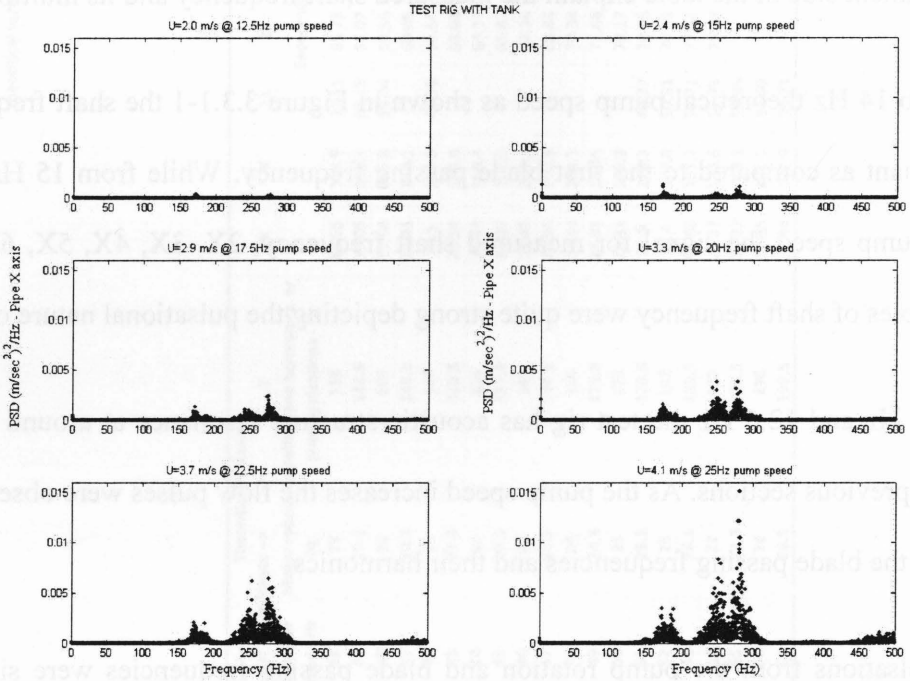

Figure 3.3.1-2 Response from the test rig in the X axis – with the tank

3.3.2. Test rig without and with the tank – Y axis:

It was observed for the test rig that in the radial plane (the Y axis) the flow pulsations were stronger as compared to their counter parts in the tangential plane (the X axis). Similar to electrical noise the flow pulsations have very low damping and they appear as narrow spikes in these plots thus making them easily distinguishable from other structural vibrations. The plot for the rig without tank in Figure 3.3.2-3 shows fundamental blade passing frequency and its higher harmonics with 7X being predominant. The spikes in the plots show that test rig exposed to flow turbulence thereby experience resonant vibration at all its natural frequencies.

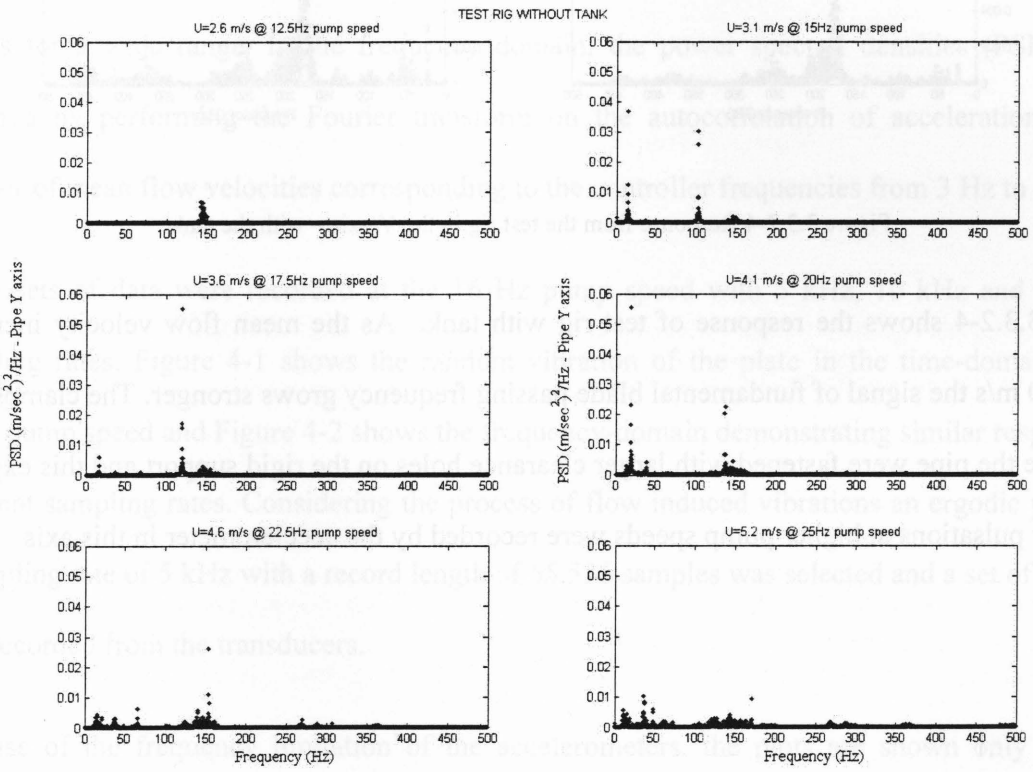

Figure 3.3.2-3 Response from the test rig in the Y axis – without the tank

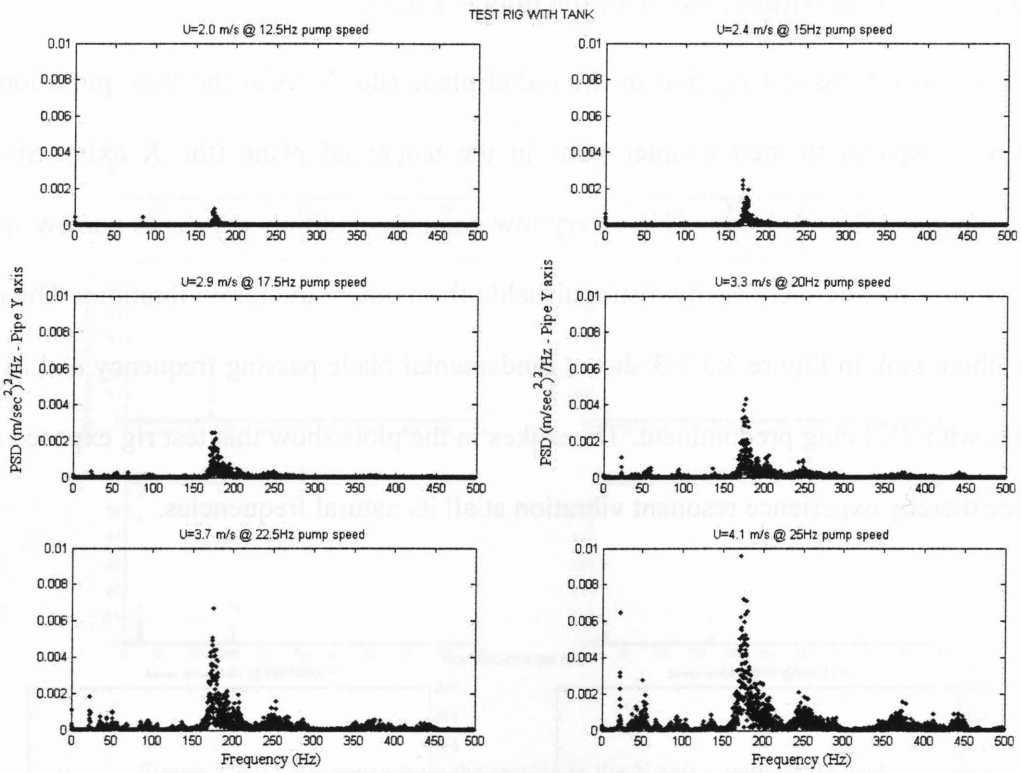

Figure 3.3.2-4 Response from the test rig in the Y axis – with the tank

Figure 3.3.2-4 shows the response of test rig with tank. As the mean flow velocity increases from 2.0 m/s the signal of fundamental blade passing frequency grows stronger. The clamps used to secure the pipe were fastened with larger clearance holes on the rigid support and this explains the flow pulsations at higher pump speeds were recorded by the accelerometer in this axis.

Chapter 4

AXIAL FLOW INDUCED VIBRATION OF A THIN PLATE

In this Chapter, a series of experiments were performed on a plate in axial flow. The motion of the plate was picked up using MEMS-based tri-axial accelerometers installed at a distance of one-fifth of the length from the fixed end, sampled using a data acquisition system (HS4), and processed using MATLAB. Two transducers glued to the plate with the measuring axis parallel to plate thickness were called as X1 at top and X2 in the bottom.

The time-domain rms accelerations of the plate motion are plotted against the mean flow velocity U m/s for a wide range. In the frequency domain, the power spectral densities (PSD's) are obtained by performing the Fourier transform on the autocorrelation of accelerations for a number of mean flow velocities corresponding to the controller frequencies from 3 Hz to 40 Hz.

Three sets of data were recorded at the 16 Hz pump speed with 5 kHz, 10 kHz and 20 kHz sampling rates. Figure 4-1 shows the random vibration of the plate in the time-domain for a given pump speed and Figure 4-2 shows the frequency-domain demonstrating similar response at different sampling rates. Considering the process of flow induced vibrations an ergodic process, a sampling rate of 5 kHz with a record length of 65,536 samples was selected and a set of 38 data files recorded from the transducers.

Because of the frequency limitation of the accelerometers, the plots are shown only for the frequency range from 0 to 500 Hz. Coincidentally, an upper limit of 500 Hz is sufficient for understanding low-frequency plate behavior in axial flow. Most of the industrial applications have seen low frequency applications or problems.

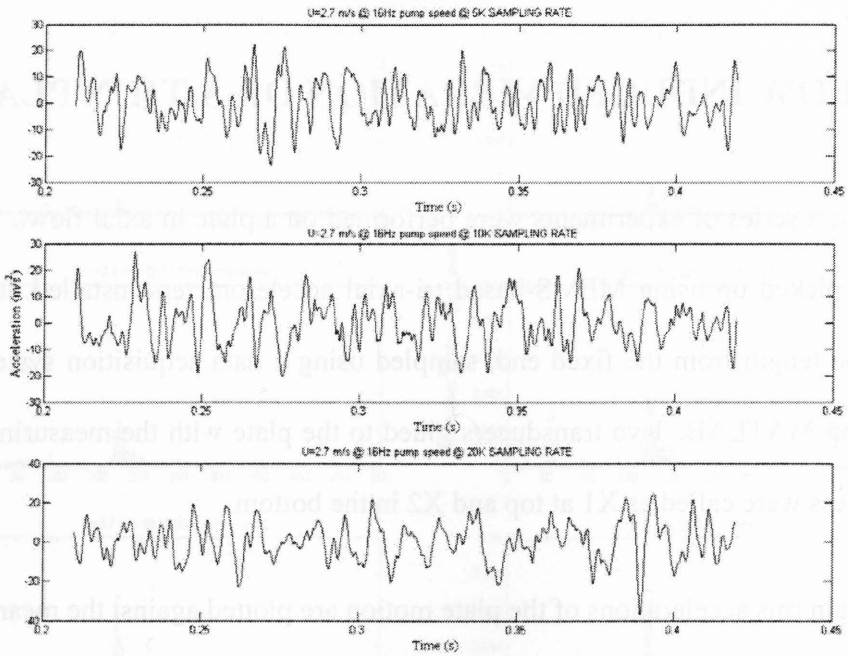

Figure 4-1 Time-domain for different sampling rates

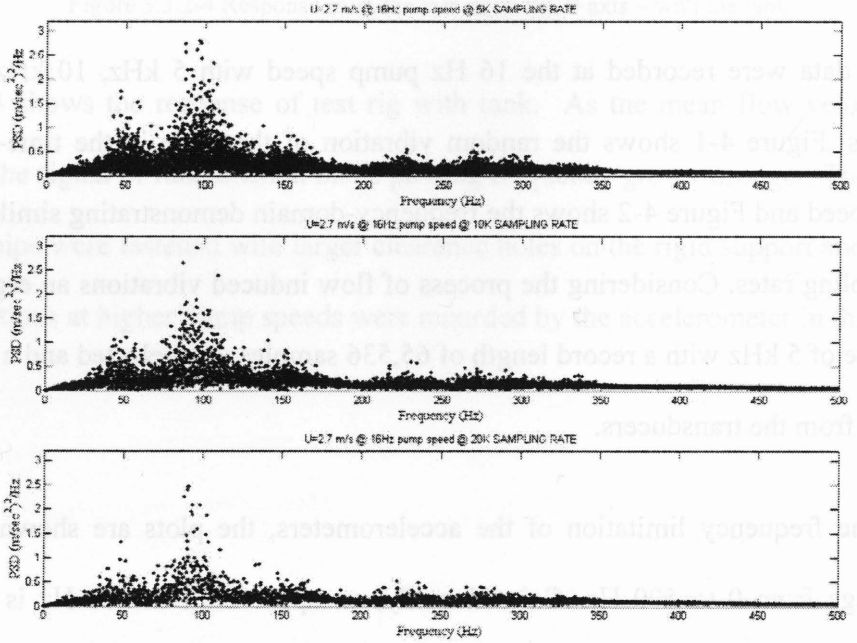

Figure 4-2 Frequency-domain PSD plots for different sampling rates

From the no flow condition, the signals from the accelerometers were recorded to establish a threshold value for noise. Figure 4-3 shows the noise generated by the entire system (including of transducer, power supply, leads and data acquisition system). The noise was quite negligible and was around ±0.1 mV or ±0.01 m/s^2 in terms of acceleration.

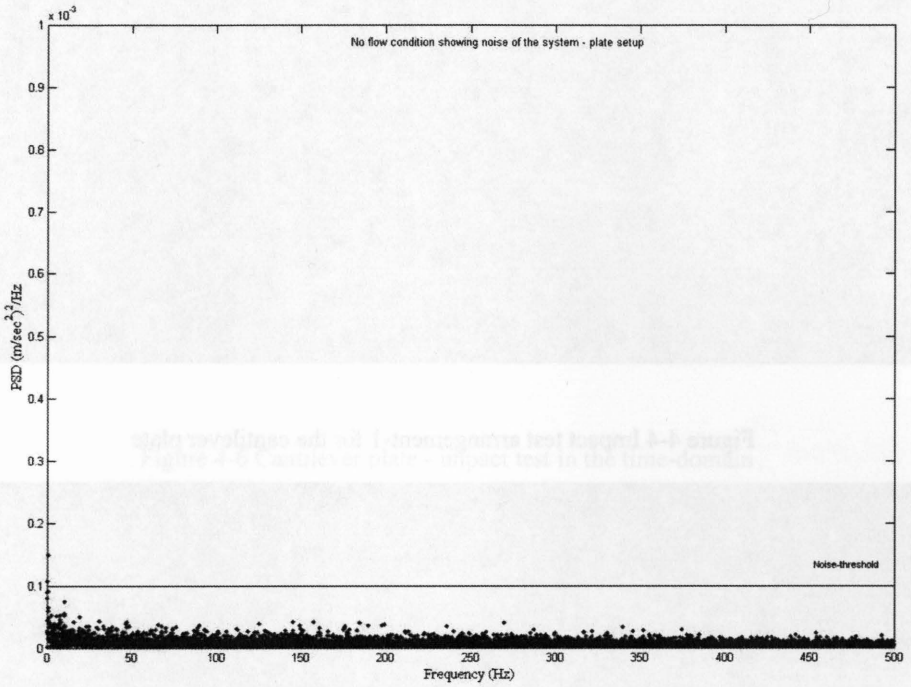

Figure 4-3 Noise level in the no-flow condition

Analysis of impact test data: A rubber mallet was used to strike gently on the test rig pipe support at various locations close to the plate specimen, shown in Figure 4-4, to carry out the impact test as shown by arrows in Figure 4-5. As the test was done in air with no water in the test rig, the spectrum in the frequency domain showed higher resonating frequencies due to the absence of the added mass effect. The time-domain plot for the impact test is shown in Figure 4-6. The plate has few resonant frequencies between in a bandwidth of 32 Hz to 350 Hz as seen from the power spectral density plot shown in Figure 4-7. Much noticeable peaks were at 33 Hz and 64 Hz.

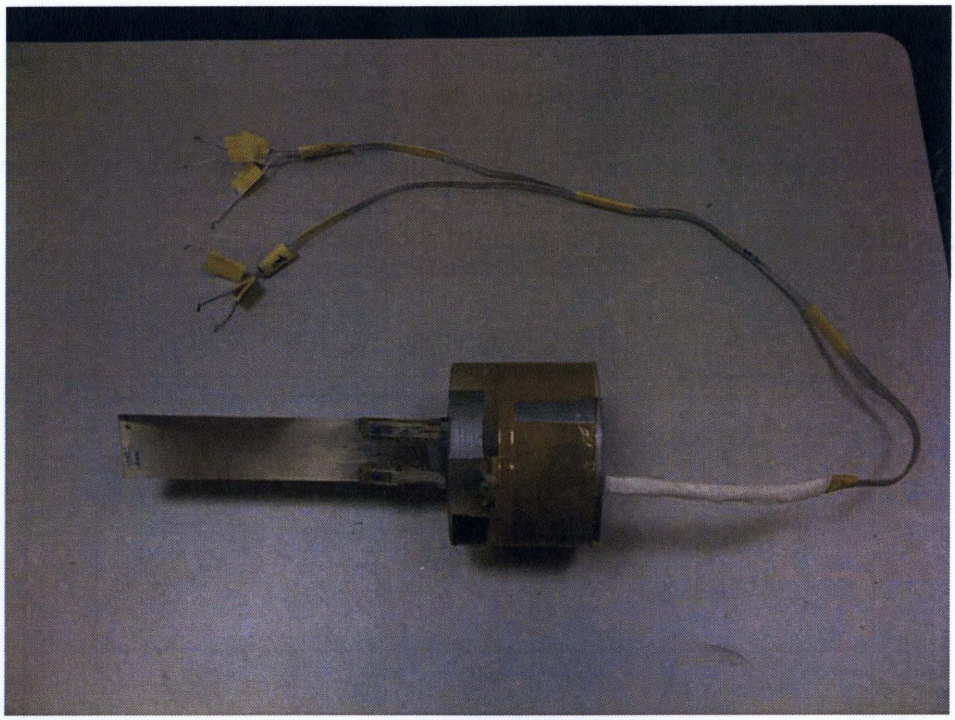

Figure 4-4 Impact test arrangement-1 for the cantilever plate

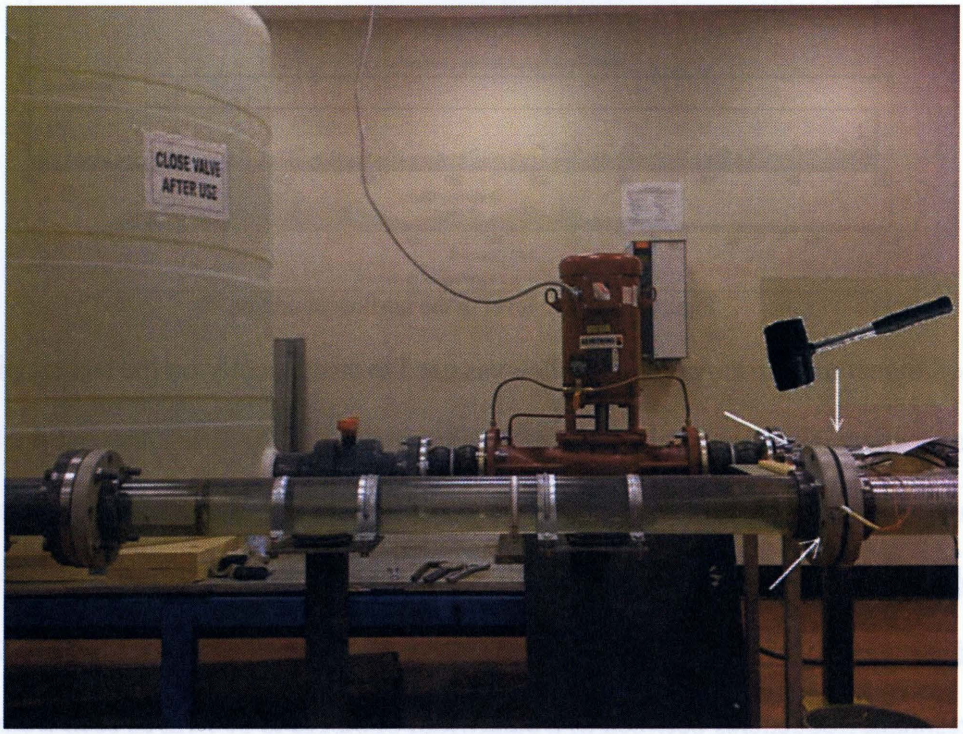

Figure 4-5 Impact test arrangement-2 for the cantilever plate

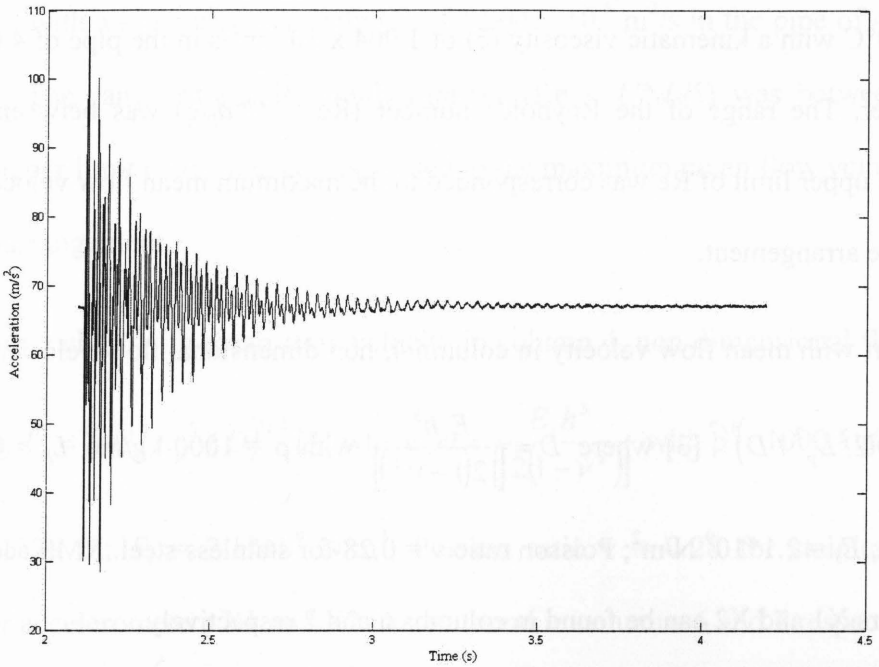

Figure 4-6 Cantilever plate - impact test in the time-domain

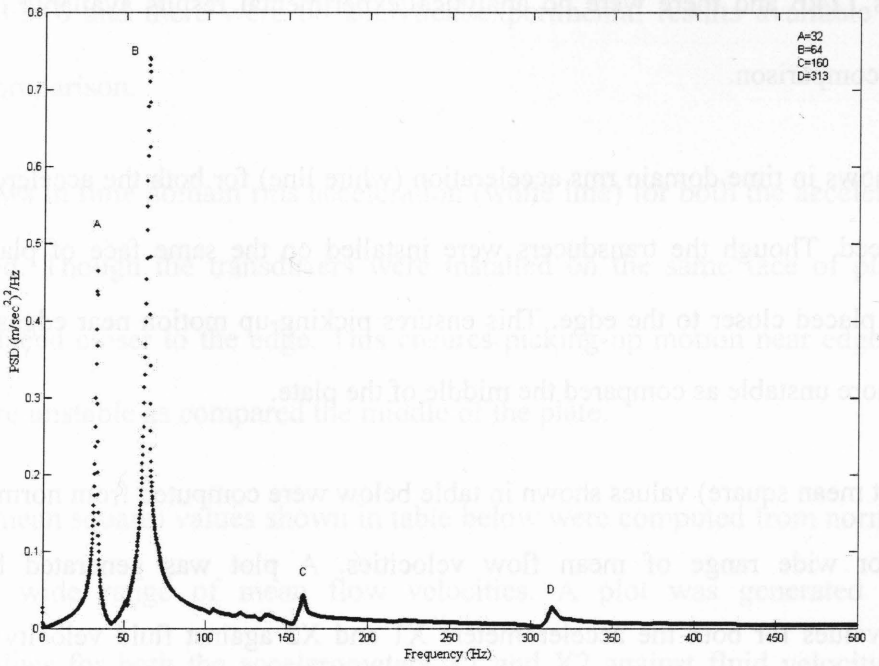

Figure 4-7 Cantilever plate - impact test results in the frequency-domain

Analysis of experimental data: The temperature in the tank and test rig filled with lukewarm water was 20°C with a kinematic viscosity (ξ) of 1.004 x 10^{-6} m^2/s in the pipe of 4.0 inch (101.6 mm) diameter. The range of the Reynolds number (Re = U^*d_p/ξ) was between 20,000 and 350,000. The upper limit of Re was corresponded to the maximum mean flow velocity of 3.8 m/s with this plate arrangement.

shows a chart with mean flow velocity in column 4, non dimensional flow velocity in column 5 using $\bar{U} = \left(\rho U^2 {L_p}^3 / D\right)^{1/2}$ [3] where $D = \frac{E_s h^3}{\left[12\left(1-\nu^2\right)\right]}$ with ρ = 1000 kg/m^3; L_p = 0.175 m; h = 0.0001778 m; $E_s = 2.1*10^9$ N/m^2; Poisson ratio ν = 0.28 for stainless steel. RMS acceleration for accelerometers X1 and X2 can be found in columns 6 and 7 respectively.

The mass ratio $\mu^* = \frac{\rho L_p}{\rho_p h}$ [3] with ρ_p = 7900 kg/m^3 was computed for the cantilever plate in water. It was 124.6 and there were no analytical/experimental results available in the known literature for comparison.

Figure 4-8 shows in time domain rms acceleration (white line) for both the accelerometers at 15 Hz pump speed. Though the transducers were installed on the same face of plate they were intentionally placed closer to the edge. This ensures picking-up motion near edges in flow that tends to be more unstable as compared the middle of the plate.

The rms (root mean square) values shown in table below were computed from norm(x)/sqrt(n) in MATLAB for wide range of mean flow velocities. A plot was generated between rms acceleration values for both the accelerometers X1 and X2 against fluid velocity as shown in Figure 4-9. This increase in rms acceleration values with respect to increase in flow velocity can

Analysis of experimental data: The temperature in the tank and test rig filled with lukewarm water was 20°C with a kinematic viscosity (ξ) of 1.004 x 10^{-6} m^2/s in the pipe of 4.0 inch (101.6 mm) diameter. The range of the Reynolds number (Re = U^*d_p/ξ) was between 20,000 and 350,000. The upper limit of Re was corresponded to the maximum mean flow velocity of 3.8 m/s with this plate arrangement.

Table-4-1 shows a chart with mean flow velocity in column 4, non dimensional flow velocity in column 5 using $\bar{U} = \left(\rho U^2 L_p{}^3 / D\right)^{1/2}$ [3] where $D = \frac{E_s h^3}{\left[12\left(1-\nu^2\right)\right]}$ with ρ = 1000 kg/m^3; L_p = 0.175 m; h = 0.0001778 m; E_s = 2.1*10^9 N/m^2; Poisson ratio ν = 0.28 for stainless steel. RMS acceleration for accelerometers X1 and X2 can be found in columns 6 and 7 respectively.

The mass ratio $\mu^* = \frac{\rho L_p}{\rho_p h}$ [3] with ρ_p = 7900 kg/m^3 was computed for the cantilever plate in water. It was 124.6 and there were no analytical/experimental results available in the known literature for comparison.

Figure 4-8 shows in time domain rms acceleration (white line) for both the accelerometers at 15 Hz pump speed. Though the transducers were installed on the same face of plate they were intentionally placed closer to the edge. This ensures picking-up motion near edges in flow that tends to be more unstable as compared the middle of the plate.

The rms (root mean square) values shown in table below were computed from norm(x)/sqrt(n) in MATLAB for wide range of mean flow velocities. A plot was generated between rms acceleration values for both the accelerometers X1 and X2 against fluid velocity as shown in Figure 4-9. This increase in rms acceleration values with respect to increase in flow velocity can

be explained as the combined effect of turbulent flow, longitudinal and transverse frictional forces, viscous and structural (hysteretic) damping and tension in the plate [3]. The difference in response curves between these transducers could be due to imperfections in manufacturing the plate and installing the transducers along with their leads. As the mean flow velocity increases with the increase pump speed it was observed that there was an increase in response from both the accelerometers.

Table-4-1 Mean flow velocity, non dimensional velocity and rms accelerations for the cantilever plate

Controller Speed - Hz	Motor speed - Hz.	Q m3/hr	U m/s	U-non dimensionalised	RMSACC X1 (m/s^2)	RMSACCE X2 (m/s^2)
3	1.5	6.50	0.223	1.578	0.087	0.089
4	2	9.00	0.308	2.185	0.096	0.097
5	2.5	11.50	0.394	2.792	0.109	0.110
6	3	14.00	0.480	3.399	0.149	0.149
7	3.5	16.50	0.565	4.006	0.202	0.193
8	4	19.00	0.651	4.613	0.274	0.259
9	4.5	21.70	0.743	5.269	0.350	0.340
10	5	24.10	0.826	5.851	0.452	0.424
11	5.5	26.60	0.911	6.458	0.605	0.565
12	6	28.30	0.970	6.871	0.680	0.635
13	6.5	30.50	1.045	7.405	0.859	0.802
14	7	33.00	1.131	8.012	1.099	1.028
15	7.5	35.50	1.216	8.619	1.328	1.192
16	8	37.90	1.299	9.202	1.607	1.376
17	8.5	40.60	1.391	9.857	1.983	1.631
18	9	43.20	1.480	10.489	2.329	1.928
19	9.5	45.60	1.562	11.071	2.632	2.189
20	10	48.30	1.655	11.727	3.139	2.549
21	10.5	50.70	1.737	12.309	3.460	2.822
22	11	53.20	1.823	12.916	3.916	3.324
23	11.5	55.70	1.908	13.523	4.418	3.692
24	12	58.30	1.998	14.155	4.865	4.163
25	12.5	60.90	2.087	14.786	5.344	4.585
26	13	63.40	2.172	15.393	6.147	5.304
27	13.5	66.00	2.261	16.024	6.617	5.777
28	14	68.50	2.347	16.631	7.391	6.280
29	14.5	71.00	2.433	17.238	8.233	6.978
30	15	73.50	2.518	17.845	9.014	7.539
31	15.5	75.80	2.597	18.404	9.748	7.935
32	16	78.10	2.676	18.962	10.780	8.799
33	16.5	81.10	2.779	19.690	11.105	9.310
34	17	83.50	2.861	20.273	13.140	10.379
35	17.5	86.20	2.953	20.929	13.686	11.088
36	18	88.50	3.032	21.487	14.777	12.396
37	18.5	91.10	3.121	22.118	14.797	13.345
38	19	93.70	3.210	22.749	17.526	14.154
39	19.5	96.20	3.296	23.356	18.526	15.278
40	20	98.60	3.378	23.939	20.067	16.150

be explained as the combined effect of turbulent flow, longitudinal and transverse frictional forces, viscous and structural (hysteretic) damping and tension in the plate [3]. The difference in response curves between these transducers could be due to imperfections in manufacturing the plate and installing the transducers along with their leads. As the mean flow velocity increases with the increase pump speed it was observed that there was an increase in response from both the accelerometers.

Table-4-1 Mean flow velocity, non dimensional velocity and rms accelerations for the cantilever plate

Controller Speed - Hz	Motor speed - Hz.	Q m3/hr	U m/s	U-non dimensionalised	RMSACC X1 (m/s^2)	RMSACCE X2 (m/s^2)
3	1.5	6.50	0.223	1.578	0.087	0.089
4	2	9.00	0.308	2.185	0.096	0.097
5	2.5	11.50	0.394	2.792	0.109	0.110
6	3	14.00	0.480	3.399	0.149	0.149
7	3.5	16.50	0.565	4.006	0.202	0.193
8	4	19.00	0.651	4.613	0.274	0.259
9	4.5	21.70	0.743	5.269	0.350	0.340
10	5	24.10	0.826	5.851	0.452	0.424
11	5.5	26.60	0.911	6.458	0.605	0.565
12	6	28.30	0.970	6.871	0.680	0.635
13	6.5	30.50	1.045	7.405	0.859	0.802
14	7	33.00	1.131	8.012	1.099	1.028
15	7.5	35.50	1.216	8.619	1.328	1.192
16	8	37.90	1.299	9.202	1.607	1.376
17	8.5	40.60	1.391	9.857	1.983	1.631
18	9	43.20	1.480	10.489	2.329	1.928
19	9.5	45.60	1.562	11.071	2.632	2.189
20	10	48.30	1.655	11.727	3.139	2.549
21	10.5	50.70	1.737	12.309	3.460	2.822
22	11	53.20	1.823	12.916	3.916	3.324
23	11.5	55.70	1.908	13.523	4.418	3.692
24	12	58.30	1.998	14.155	4.865	4.163
25	12.5	60.90	2.087	14.786	5.344	4.585
26	13	63.40	2.172	15.393	6.147	5.304
27	13.5	66.00	2.261	16.024	6.617	5.777
28	14	68.50	2.347	16.631	7.391	6.280
29	14.5	71.00	2.433	17.238	8.233	6.978
30	15	73.50	2.518	17.845	9.014	7.539
31	15.5	75.80	2.597	18.404	9.748	7.935
32	16	78.10	2.676	18.962	10.780	8.799
33	16.5	81.10	2.779	19.690	11.105	9.310
34	17	83.50	2.861	20.273	13.140	10.379
35	17.5	86.20	2.953	20.929	13.686	11.088
36	18	88.50	3.032	21.487	14.777	12.396
37	18.5	91.10	3.121	22.118	14.797	13.345
38	19	93.70	3.210	22.749	17.526	14.154
39	19.5	96.20	3.296	23.356	18.526	15.278
40	20	98.60	3.378	23.939	20.067	16.150

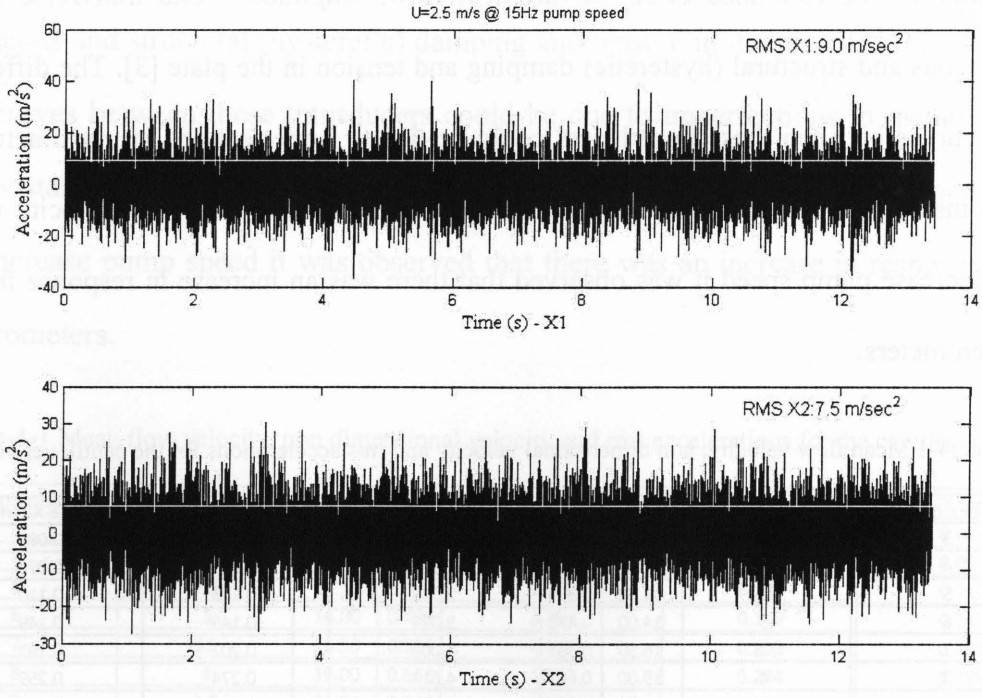

Figure 4-8 Time-domain plot for the flow velocity U=2.5 m/s at 15Hz pump speed

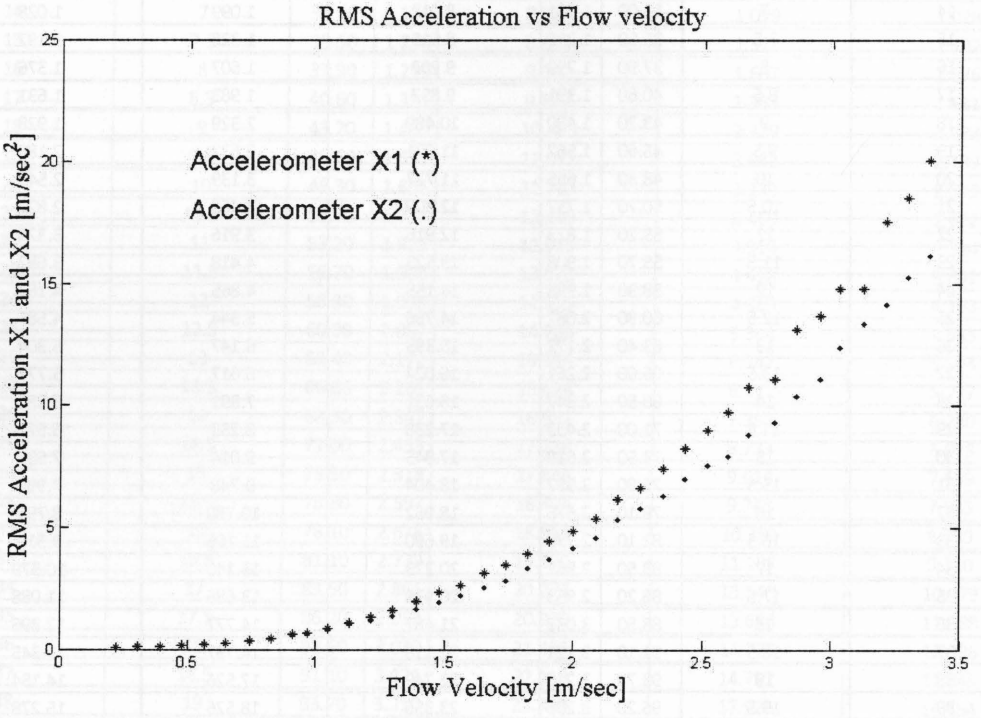

Figure 4-9 RMS acceleration (X1 and X2) *vs.* flow velocity (U)

Acceleration response in time-domain at various speeds was shown in the Figure 4-10 . Please note the scale for ordinate was not adjusted in order to present the magnitude of acceleration and its dependency with the flow velocity. A close observation of the below plot shows that the development of peak-peak acceleration magnitude from ~0.5 m/s^2 at 0.3 m/s flow velocity to 50 m/s^2 at 3.4 m/s flow velocity.

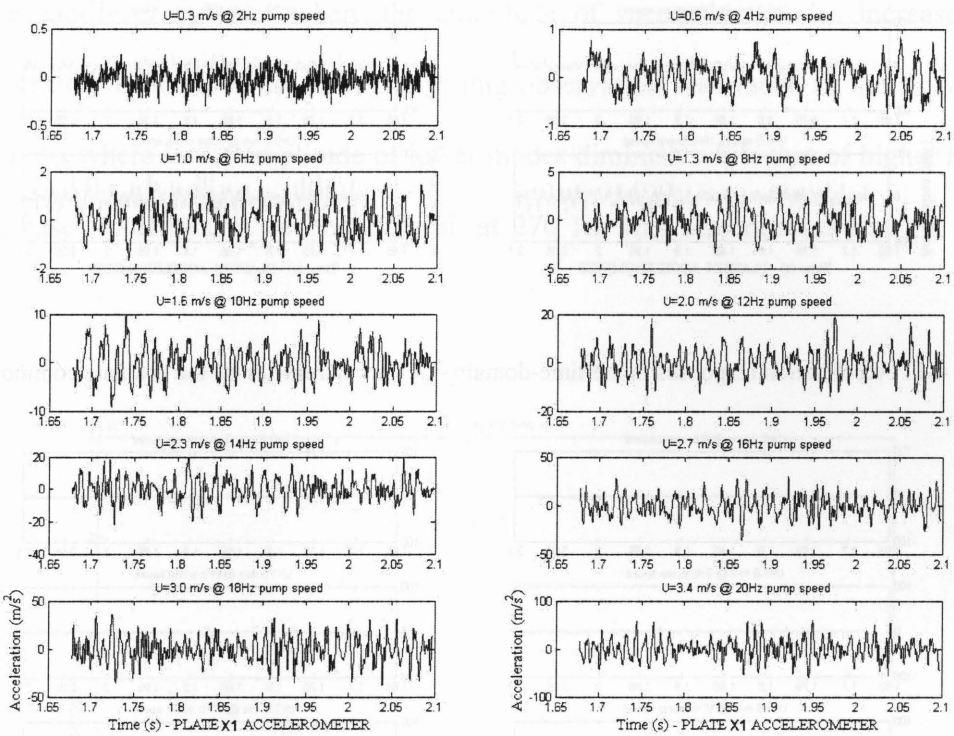

Figure 4-10 Acceleration responses on the time-domain - X1 accelerometer with the ordinate auto scale

Figure 4-11 and Figure 4-12 show the time-domain response for the accelerometers X1 and X2 on common scale. It was observed that the influence of flow velocity was quite significant on the magnitude of acceleration amplitude. From these plots it was evident that the 100 fold increase in magnitude of acceleration amplitude for an approximately ten fold increase in flow velocity.

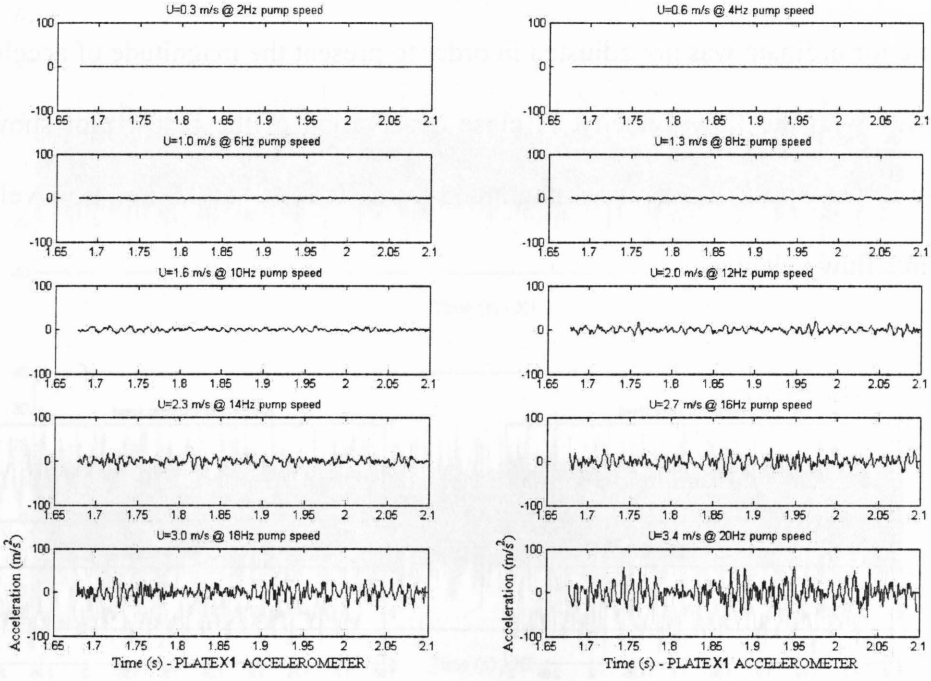

Figure 4-11 Acceleration responses in the time-domain – X1 accelerometer on the ordinate common scale

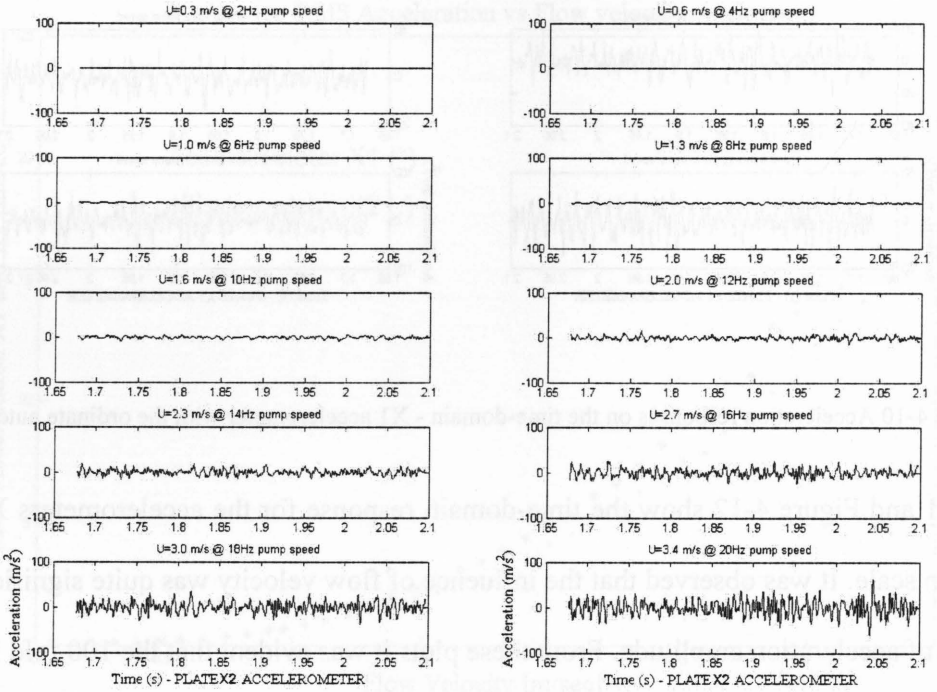

Figure 4-12 Acceleration responses in the time-domain – X2 accelerometer on the ordinate common scale

Following the similar responses from both the accelerometers ongoing analysis was carried out considering one accelerometer. Figure 4-13 to Figure 4-18 depicts the behavior of natural frequencies of cantilever plate from the mean flow velocity of 0.6 m/s (or pump speed 4 Hz) to 3.4 m/s (or pump speed 20 Hz). As the flow velocity increases the dynamic response of the plate changes drastically from zero acceleration to almost 3 m/s^2. The different modes were seen with increasing magnitude as seen successive power spectral density plots. The results were similar to that of the cantilever cylinder where the amplitude of successive modes increases at their respective critical flow velocities. But one strong observation was made as the flow increases beyond 3.0 m/s where in the amplitude of lower modes diminish while that of higher mode (100 Hz in this case) increases. A secondary peak at 270 Hz was also observed at the high flow velocities.

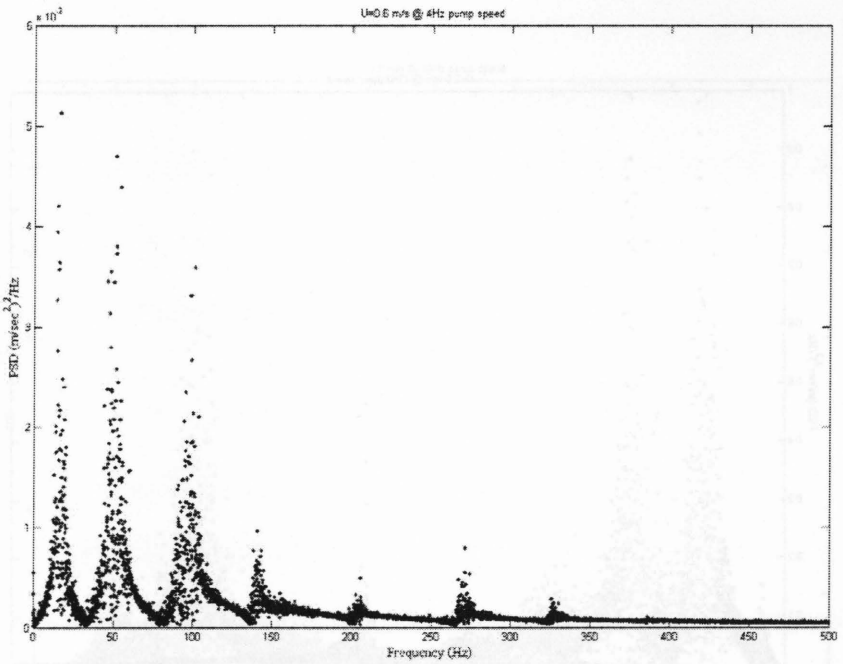

Figure 4-13 PSD at U=0.6 m/s

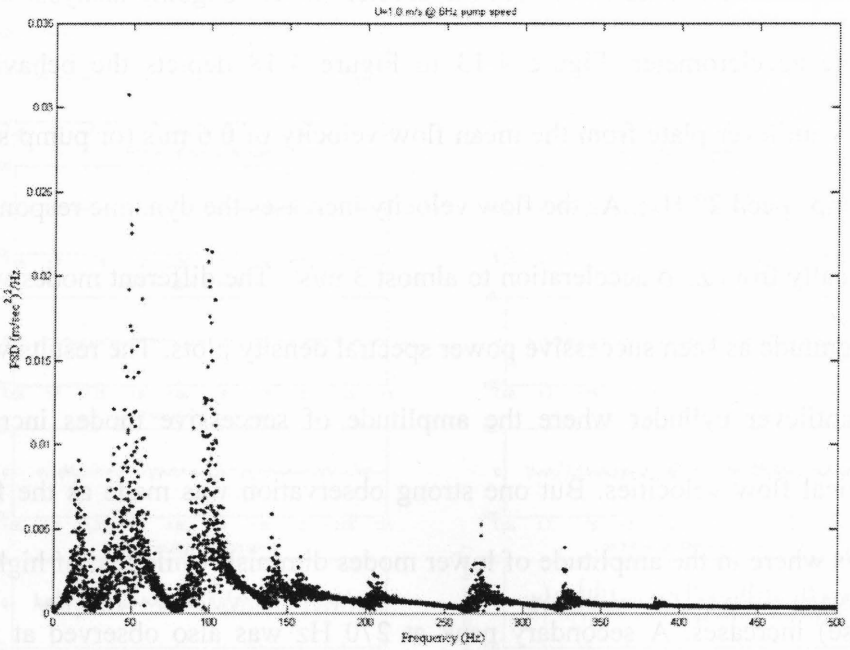

Figure 4-14 PSD at U=1 m/s

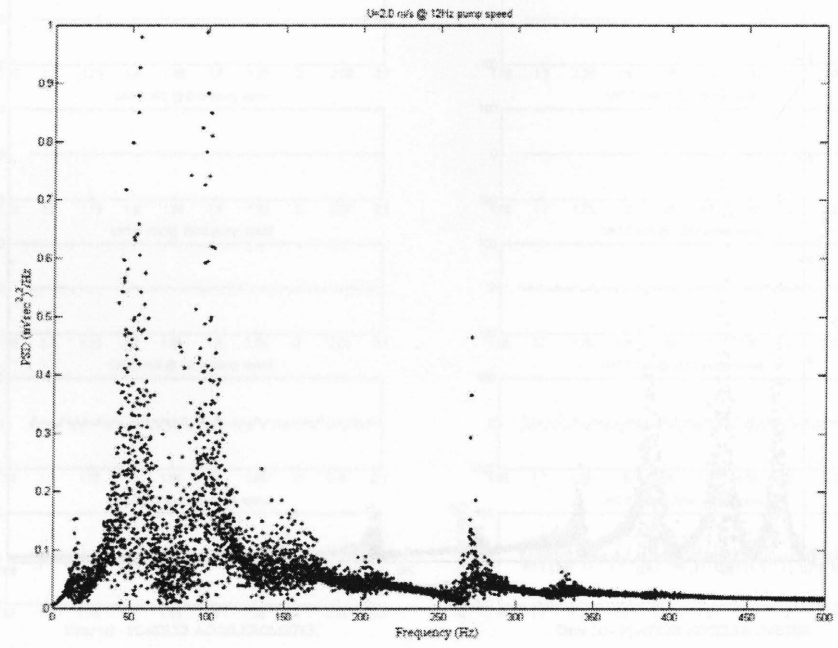

Figure 4-15 PSD at U=2 m/s

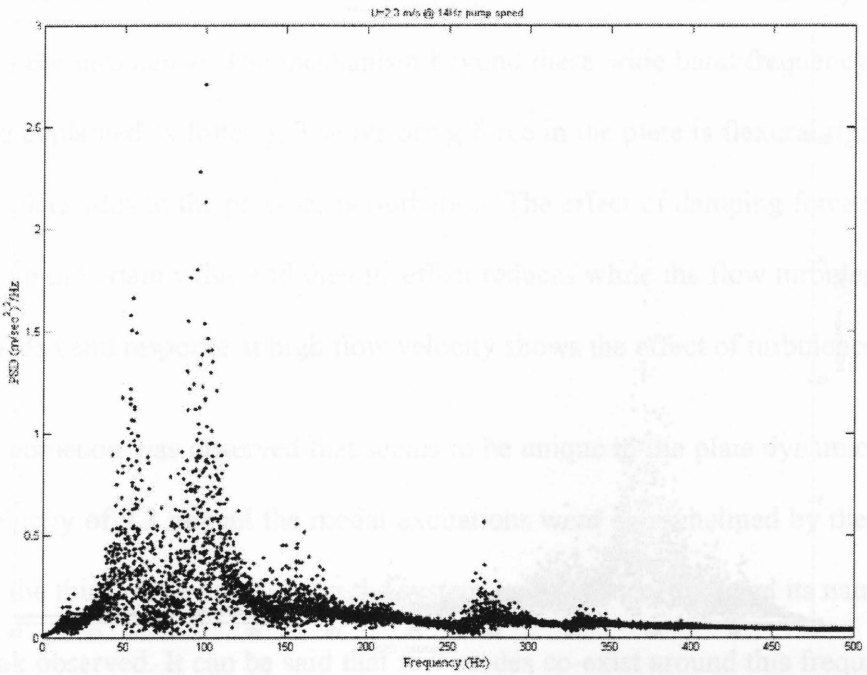

Figure 4-16 PSD at U=2.3 m/s

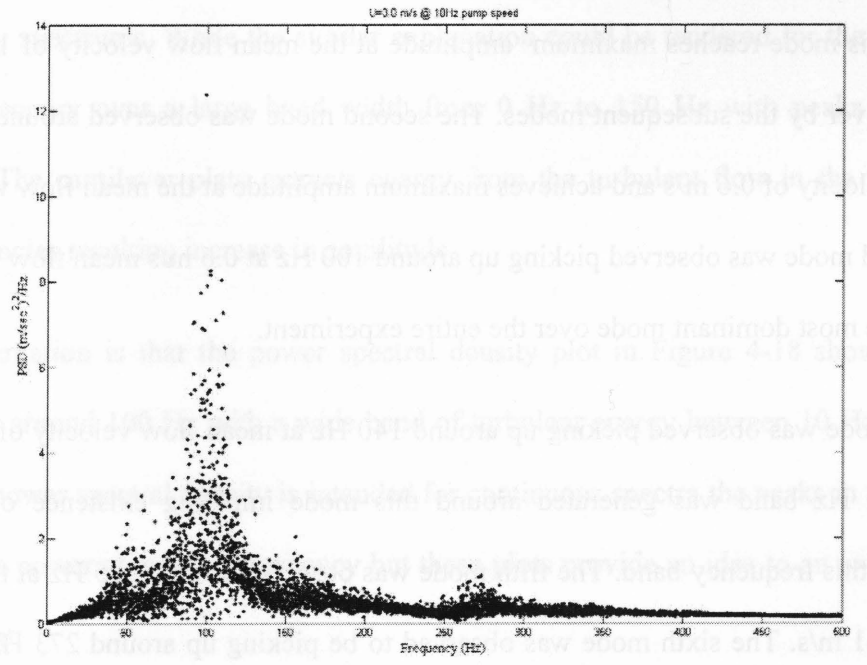

Figure 4-17 PSD at U=3.0 m/s

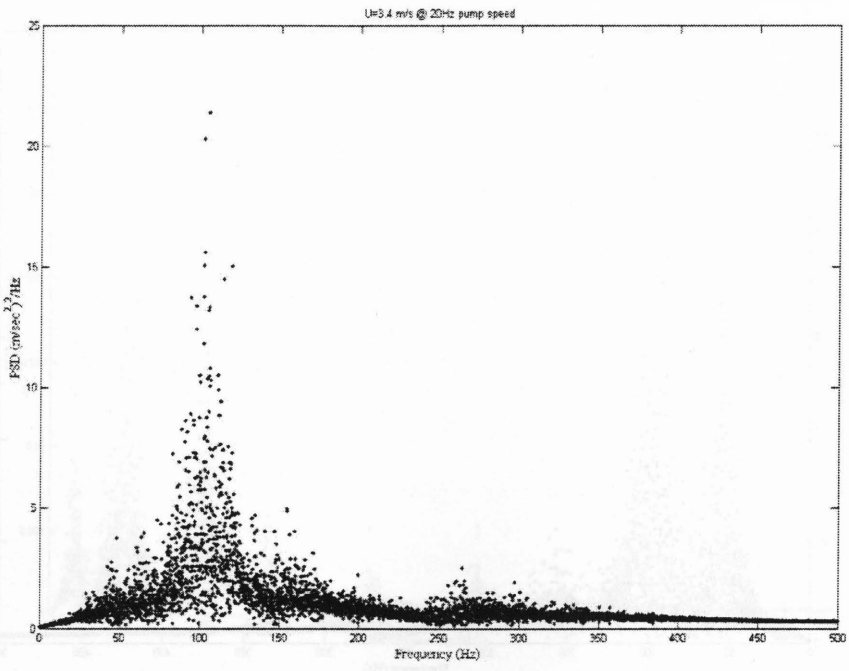

Figure 4-18 PSD at U=3.4 m/s

The first mode was observed around 15 Hz at the mean flow velocity of 0.48 m/s above the noise threshold. This mode reaches maximum amplitude at the mean flow velocity of 1.6 m/s before being taken over by the subsequent modes. The second mode was observed around 54 Hz at the mean flow velocity of 0.6 m/s and achieves maximum amplitude at the mean flow velocity of 3.2 m/s. The third mode was observed picking up around 100 Hz at 0.6 m/s mean flow velocity. This mode was the most dominant mode over the entire experiment.

The fourth mode was observed picking up around 140 Hz at mean flow velocity of 1 m/s. In the process a 30 Hz band was generated around this mode implying existence of few modes embedded in this frequency band. The fifth mode was observed around 205 Hz at the mean flow velocity of 1.1 m/s. The sixth mode was observed to be picking up around 273 Hz at the mean flow velocity of 0.82 m/s.

With the turbulence being a function of mean flow velocity the modal instability increases with the increase in the turbulence. The mechanism beyond these wide band frequency response due to flow can be explained as follows. The restoring force in the plate is flexural rigidity while the tension in the plate adds to the pressure perturbation. The effect of damping force increases with flow velocity up to certain value and then its effect reduces while the flow turbulence takes over the system. Wide band response at high flow velocity shows the effect of turbulence [3].

A strange phenomenon was observed that seems to be unique to the plate dynamics. Beyond the mean flow velocity of 2.3 m/s all the modal excitations were overwhelmed by the turbulence in flow. Around the third mode i.e., 100 Hz the system extracts energy around its natural frequency and hence peak observed. It can be said that few modes co-exist around this frequency resulting in the wide band excitation 70 Hz to 130 Hz.

It was observed the amplitude of the first, second and third modes dominate over the entire power density spectrums. While the similar explanation could be tendered for the accumulation of turbulent energy over a large band width from 0 Hz to 150 Hz with peaks at the modal frequencies. The cantilever plate extracts energy from the turbulent flow in the vicinity of its modal frequencies resulting increase in amplitude.

Another observation is that the power spectral density plot in Figure 4-18 shows the energy concentration around 100 Hz with a wide band of turbulent energy between 10 Hz and 300 Hz. Though this power spectral density is intended for continuous spectra the peaks in the spectra do not reflect the power at a given frequency but these plots provide an idea to an extent about the energy content.

Finally a 3D plot with power spectral density, mean flow velocity and frequency as the respective axes was shown in Figure 4-19 to visualize the Fluid-Structure interaction with the flow developing around the plate.

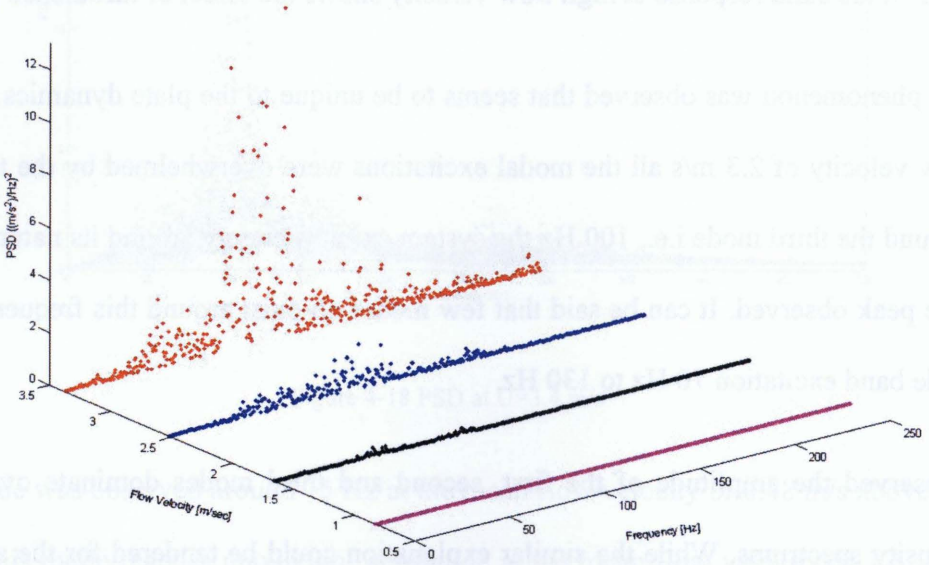

Figure 4-19 Acceleration amplitude *vs.* flow velocity *vs.* frequency

From the above analysis of responses of the cantilever plate it can be seen that the effect of mean flow velocity on excitation of the various resonant frequencies. Also the magnitudes of these resonating frequencies were directly proportional to the mean flow velocity. With the increase in the mean flow velocity it was seen that the plate vibration becomes unstable. This was clear from these plots the excitation of wide band of frequencies at higher mean flow velocities. In contrast to cylinder experiment where multiple modes still exist with increasingly stronger amplitude, in the plate experiment it was observed that beyond a critical mean flow velocity (3.0 m/s in this case) the plate tends to come to an equilibrium position which in this case was around 100 Hz.

Chapter 5

CONCLUSIONS AND FUTURE WORK

5.1 Conclusions

In this thesis, the axial pipe flow induced vibrations of a beam and a plate are investigated experimentally. Use of MEMS based transducers allows the direct and accurate measurement of acceleration without altering the flows surrounding the transducers. A large number of experiments covering the two structures, a test rig without and with a large water tank for reducing the acoustic-induced vibrations, were carried out over a wide range of mean flow velocities. These comprehensive studies and experimental results are useful to power and process industries where pipe flow induced vibrations in various components (e.g., butterfly valves) are often encountered.

The flow in the test rig with and without the tank was both turbulent and pulsational at all pump speeds. At 27 Hz pump speed for the cantilever cylinder the mean flow velocity was 5.7 m/s in the test rig without the tank and the magnitude of rms acceleration in the X axis was 4.3g while in the Y axis it was 3.3g. For the same pump speed the mean flow velocity was 4.7 m/s in the test rig with the tank and the maximum values of rms acceleration in the X and Y axes were 1.5g to 2g for the cylinder. It was noticed that the active frequency band for the cylinder where resonances occur for different modes in the X axis was from 7 Hz till 200 Hz. The response of the cylinder in the Y axis was different from that of the X axis due to the presence of steel strips acting as stiffeners. The active frequency band where resonances occur for different modes in the cylinder Y axis was from 19 Hz to 360 Hz. These results show the turbulent flow causes excitation of first and higher modes in both the axes for the cylinder.

For the cantilever plate the maximum rms acceleration was approximately 2g at 3.4 m/s mean flow velocity. Vibrations observed in the cantilever plate can be categorized as high-frequency low-amplitude type that was observed as common phenomenon in thinner plates. These plots depict the evolution of the plate higher modes as mean flow velocity increases. The flow upstream to plate is highly turbulent and the radial studs holding the plate in the fixture-adaptor make the flow further more complex. The flow turbulence is the driving mechanism for these vibrations as was seen from energy concentration over wide band frequency from 10 Hz to 200 Hz.

5.2 Future Work

Developing a computational fluid dynamics model for simulating the three dimensional flow surrounding the flexible structures in an axial pipe flow is recommended.

Appendix A

Cylinder and plate preparation process for the experiments

A.1 Preparation of cylinder

A length of 220 mm of 12.7 mm diameter silicon rubber chord stock was cut to ensure minimum radius of curvature when in free state and ends are ensured square to the longitudinal axis. A hole of 8.2 mm diameter was drilled for 5 mm deep along the axis at one end using an end mill at high spindle speed. Along longitudinal axis two grooves were sliced for 4mm deep for a length of 152.5 mm with a professional stainless steel knife on either side of the XOZ plane along the Y axis as shown in the Figure A.1-1.

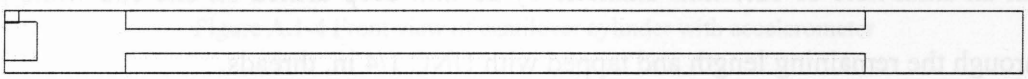

Figure A.1-1 Sectional view of silicon rubber cylinder after machining

Two thin strips of 3.9 mm wide by 152.5 mm long were cut from 0.010 in. thick shim stock of AISI316 (stainless steel) manufactured by Maudlin & Sons Mfg Co., Inc., Texas. A thin layer of silicon rubber adhesive (Sil-Poxy from Smooth-On Inc., Easton, PA) was evenly applied on either side of these strips. These strips were then carefully inserted in to the groves made on the silicon rubber cylinder specimen as shown in Figure A.1-2. (Sil-Poxy, the silicon rubber adhesive is a one-component adhesive made specifically for bonding RTV silicone rubber to silicone rubber and other materials with a work time of 5 minute and cure time of 12 minutes).

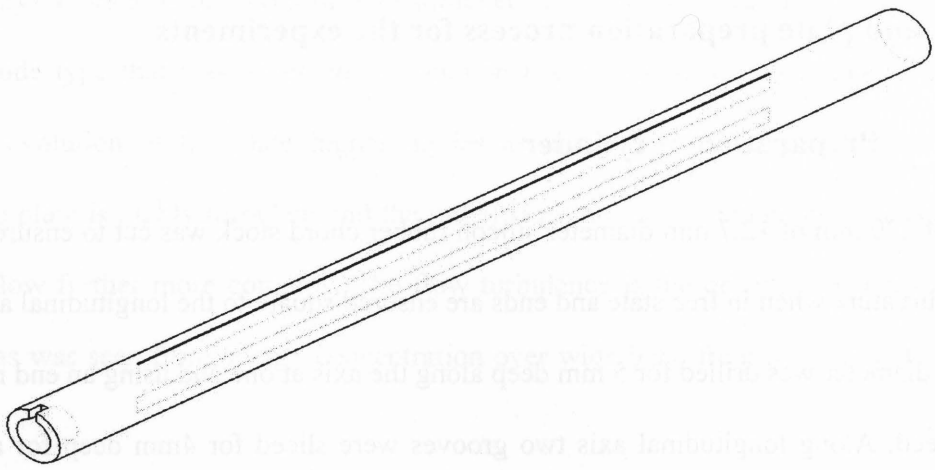

Figure A.1-2 Isometric view of silicon rubber cylinder with SS Strips

A 16 mm diameter by 40 mm long fixture was machined from 20 mm diameter Al 6061 bar stock with an axial hole of 12.7 mm diameter by 25 mm deep drilled on one end while a hole drilled through the remaining length and tapped with UNC 1/4 in. threads.

Commercially available five minute epoxy prepared and applied evenly inside the surface of this 12.7 mm diameter hole and the silicon rubber cylinder with the blunt end inserted in to this hole allowing the epoxy to cure thus forming rigid joint between the fixture and silicon rubber cylinder.

An adapter machined out of Al 6061 with 16 mm diameter by 50 mm long with four M4x0.7 radial holes tapped through all the wall thickness. This was then clamped to the fixture-silicon rubber cylinder using a ¼ in-20 socket cap screw of 7/8 inch long as shown in Figure A.1-3. Figure A.1-4 shows the layout of the accelerometer at the free end and the four ribbon cables lay out along the longitudinal axis. Figure A.1-5 shows the cantilever cylinder along with the test

fixture and the transducer installed. The harnesses were routed in such a way that they contribute minimal flow disturbance.

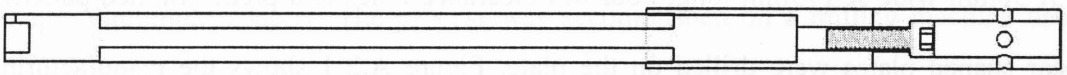

Figure A.1-3 Sectional view of permanent assembly of cantilever cylinder

Figure A.1-4 Front view of cantilever cylinder with accelerometer

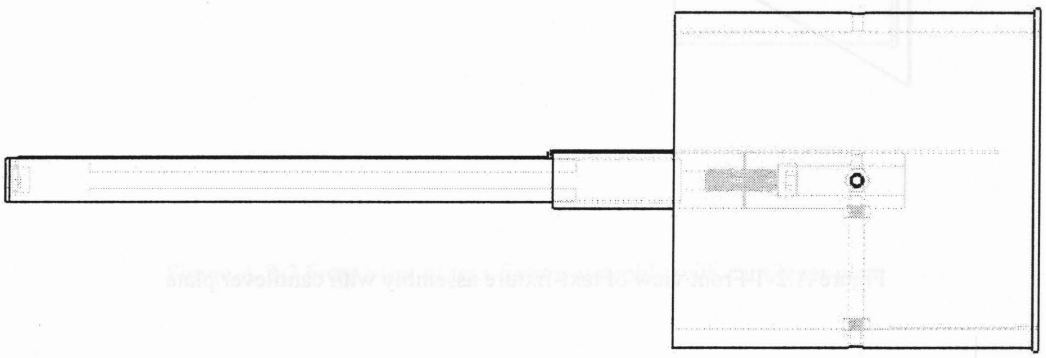

Figure A.1-5 Front view of text-fixture assembly with cantilever cylinder

A.2 Preparation of thin plate

For this experiment, the clamped-free or cantilevered AISI316 (stainless steel) plate, 0.178mm thick X 36mm wide X 175mm long. Four M4 clearance holes at a predetermined pattern using the pear shaped plates were drilled on the plate. Figure A.2-1 shows the manufacturing and assembly of the stainless steel plate. The assembly contains two half pear shaped aluminum plates clamping the plate with the help of M4x0.7 socket head flat screws.

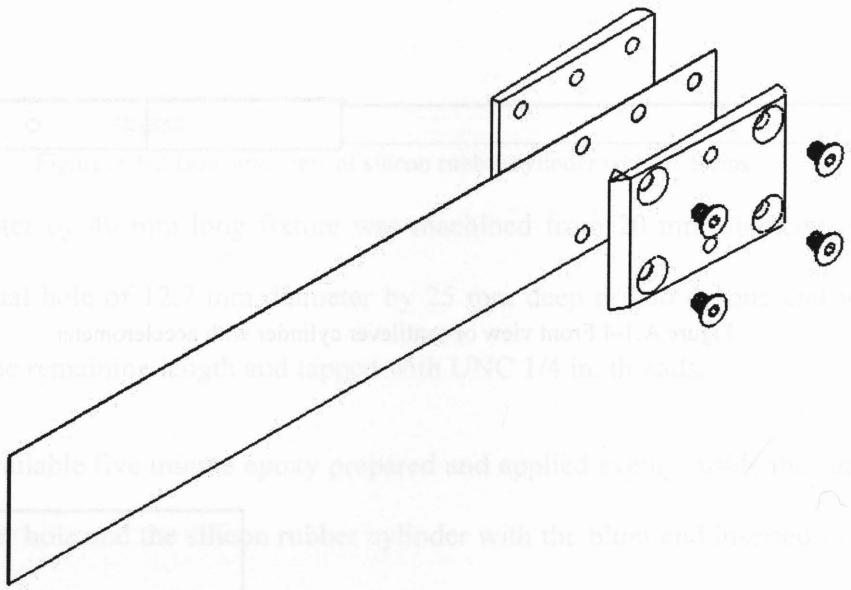

Figure A.2-1 Front view of text-fixture assembly with cantilever plate

Test-fixture for cantilever plate: In order to place the cantilever plate along the axis of the test section of pipe in the water circulating test rig, a simple test-fixture was designed with a 4 inch (101.6 mm) outside diameter (OD) and 3½ inch (88.9 mm) inside diameter (ID) of 3.5 inch (88.9 mm) polycarbonate tube. The OD of the tube was machined down to 100 mm diameter for a

length of 86 mm leaving a shoulder so that it can slide into the test section of the pipe without interference. Two radial holes drilled through all the wall thickness of the tube and tapped with M4x0.7 threads at a predetermined position(s) by transferring the clearance-hole pattern from the pear shaper aluminum adapter. The process was accomplished on a milling machine using an indexing head.

The cantilever plate – aluminum adapter was then secured along the axis of the tube with the help of four M4x0.7 stainless steel studs and four pairs of M4x0.7 hexagonal nuts with an endeavor to achieve zero DOF at the fixed end of the cantilever as shown in Figure A.2-2.

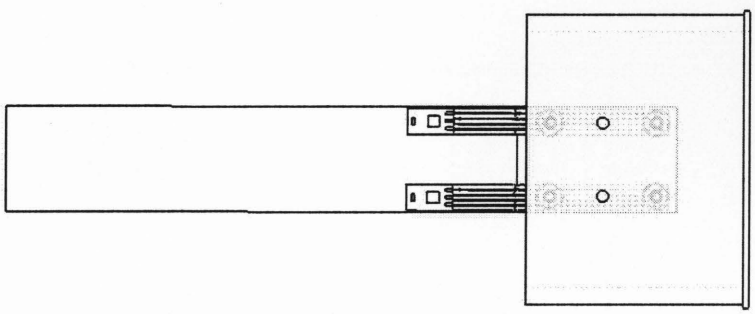

Figure A.2-2 Front view of text-fixture assembly with cantilever plate

Appendix B

Data sheet for ADXL321 bi-axial accelerometer used in cylinder

Small and Thin ±18 *g* Accelerometer

ADXL321

FEATURES

Small and thin
4 mm × 4 mm × 1.45 mm LFCSP package
3 mg resolution at 50 Hz
Wide supply voltage range: 2.4 V to 6 V
Low power: 350 µA at V_S = 2.4 V (typ)
Good zero *g* bias stability
Good sensitivity accuracy
X-axis and Y-axis aligned to within 0.1° (typ)
BW adjustment with a single capacitor
Single-supply operation
10,000 *g* shock survival
Compatible with Sn/Pb and Pb-free solder processes

APPLICATIONS

Vibration monitoring and compensation
Abuse event detection
Sports equipment

GENERAL DESCRIPTION

The ADXL321 is a small and thin, low power, complete dual-axis accelerometer with signal conditioned voltage outputs, which is all on a single monolithic IC. The product measures acceleration with a full-scale range of ±18 *g* (typical). It can also measure both dynamic acceleration (vibration) and static acceleration (gravity).

The ADXL321's typical noise floor is 320 µg/√Hz, allowing signals below 3 mg to be resolved in tilt-sensing applications using narrow bandwidths (<50 Hz).

The user selects the bandwidth of the accelerometer using capacitors C_X and C_Y at the X_{OUT} and Y_{OUT} pins. Bandwidths of 0.5 Hz to 2.5 kHz may be selected to suit the application.

The ADXL321 is available in a very thin 4 mm × 4 mm × 1.45 mm, 16-lead, plastic LFCSP.

FUNCTIONAL BLOCK DIAGRAM

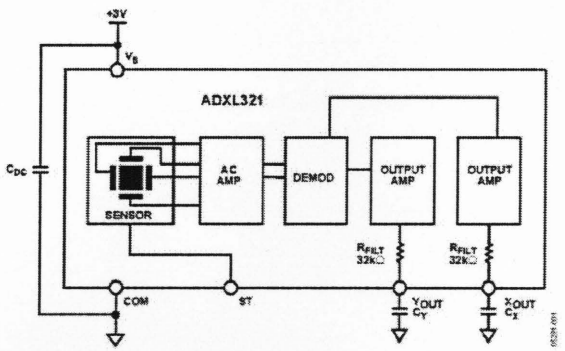

Figure 1.

One Technology Way, P.O. Box 9106, Norwood, MA 02062-9106, U.S.A.
Tel: 781.329.4700 **www.analog.com**
Fax: 781.326.8703

TABLE OF CONTENTS

REVISION HISTORY

12/04—Revision 0: Initial Version

SPECIFICATIONS[1]

T_A = 25°C, V_S = 3 V, C_X = C_Y = 0.1 µF, Acceleration = 0 *g*, unless otherwise noted.

Table 1.

Parameter	Conditions	Min	Typ	Max	Unit
SENSOR INPUT	Each axis				
Measurement Range			±18		*g*
Nonlinearity	% of full scale		±0.2		%
Package Alignment Error			±1		Degrees
Alignment Error	X sensor to Y sensor		±0.1		Degrees
Cross Axis Sensitivity			±2		%
SENSITIVITY (RATIOMETRIC)[2]	Each axis				
Sensitivity at X_{OUT}, Y_{OUT}	V_S = 3 V	51	57	63	mV/*g*
Sensitivity Change due to Temperature[3]	V_S = 3 V		0.01		%/°C
ZERO *g* BIAS LEVEL (RATIOMETRIC)	Each axis				
0 *g* Voltage at X_{OUT}, Y_{OUT}	V_S = 3 V	1.4	1.5	1.6	V
0 *g* Offset vs. Temperature			±2		mg/°C
NOISE PERFORMANCE					
Noise Density	@ 25°C		320		µg/√Hz rms
FREQUENCY RESPONSE[4]					
C_X, C_Y Range[5]		0.002		10	µF
R_{FILT} Tolerance			32 ± 15%		kΩ
Sensor Resonant Frequency			5.5		kHz
SELF-TEST[6]					
Logic Input Low			0.6		V
Logic Input High			2.4		V
ST Input Resistance to Ground			50		kΩ
Output Change at X_{OUT}, Y_{OUT}	Self-test 0 to 1		18		mV
OUTPUT AMPLIFIER					
Output Swing Low	No load		0.3		V
Output Swing High	No load		2.6		V
POWER SUPPLY					
Operating Voltage Range		2.4		6	V
Quiescent Supply Current			0.49		mA
Turn-On Time[7]			20		ms
TEMPERATURE					
Operating Temperature Range		−20		+70	°C

[1] All minimum and maximum specifications are guaranteed. Typical specifications are not guaranteed.
[2] Sensitivity is essentially ratiometric to V_S.
[3] Defined as the change from ambient-to-maximum temperature or ambient-to-minimum temperature.
[4] Actual frequency response controlled by user-supplied external capacitor (C_X, C_Y).
[5] Bandwidth = 1/(2 × π × 32 kΩ × C). For C_X, C_Y = 0.002 µF, bandwidth = 2500 Hz. For C_X, C_Y = 10 µF, bandwidth = 0.5 Hz. Minimum/maximum values are not tested.
[6] Self-test response changes cubically with V_S.
[7] Larger values of C_X, C_Y increase turn-on time. Turn-on time is approximately 160 × C_X or C_Y + 4 ms, where C_X, C_Y are in µF.

ABSOLUTE MAXIMUM RATINGS

Table 2.

Parameter	Rating
Acceleration (Any Axis, Unpowered)	10,000 *g*
Acceleration (Any Axis, Powered)	10,000 *g*
V_S	−0.3 V to +7.0 V
All Other Pins	(COM − 0.3 V) to (V_S + 0.3 V)
Output Short-Circuit Duration (Any Pin to Common)	Indefinite
Operating Temperature Range	−55°C to +125°C
Storage Temperature	−65°C to +150°C

Stresses above those listed under Absolute Maximum Ratings may cause permanent damage to the device. This is a stress rating only; functional operation of the device at these or any other conditions above those indicated in the operational section of this specification is not implied. Exposure to absolute maximum rating conditions for extended periods may affect device reliability.

ESD CAUTION

ESD (electrostatic discharge) sensitive device. Electrostatic charges as high as 4000 V readily accumulate on the human body and test equipment and can discharge without detection. Although this product features proprietary ESD protection circuitry, permanent damage may occur on devices subjected to high energy electrostatic discharges. Therefore, proper ESD precautions are recommended to avoid performance degradation or loss of functionality.

PIN CONFIGURATION AND FUNCTION DESCRIPTIONS

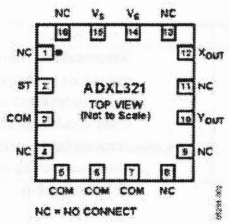

Figure 2. Pin Configuration

Table 3. Pin Function Descriptions

Pin No.	Mnemonic	Description
1, 4, 8, 9, 11, 13, 16	NC	Do Not Connect
2	ST	Self-Test
3, 5 to 7	COM	Common
10	Y_{OUT}	Y Channel Output
12	X_{OUT}	X Channel Output
14, 15	V_S	2.4 V to 6 V

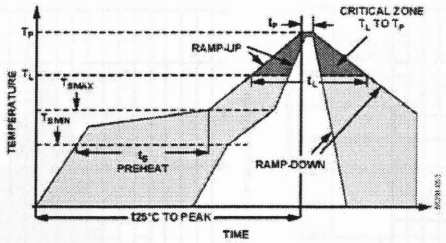

Figure 3. Recommended Soldering Profile

Table 4. Recommended Soldering Profile

Profile Feature	Sn63/Pb37	Pb-Free
Average Ramp Rate (T_L to T_P)	3°C/s max	3°C/s max
Preheat		
Minimum Temperature (T_{SMIN})	100°C	150°C
Minimum Temperature (T_{SMAX})	150°C	200°C
Time (T_{SMIN} to T_{SMAX}), t_S	60 s – 120 s	60 s – 150 s
T_{SMAX} to T_L		
Ramp-Up Rate	3°C/s	3°C/s
Time Maintained Above Liquidous (T_L)		
Liquidous Temperature (T_L)	183°C	217°C
Time (t_L)	60 s – 150 s	60 s – 150 s
Peak Temperature (T_P)	240°C + 0°C/–5°C	260°C + 0°C/–5°C
Time within 5°C of Actual Peak Temperature (t_P)	10 s – 30 s	20 s – 40 s
Ramp-Down Rate	6°C/s max	6°C/s max
Time 25°C to Peak Temperature	6 min max	8 min max

TYPICAL PERFORMANCE CHARACTERISTICS (V_S = 3.0 V)

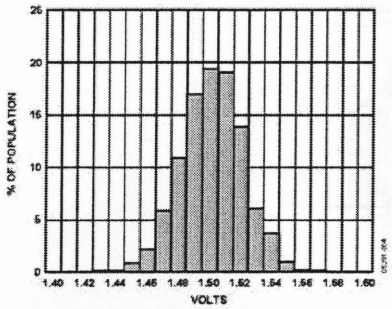

Figure 4. X-Axis Zero g Bias at 25°C

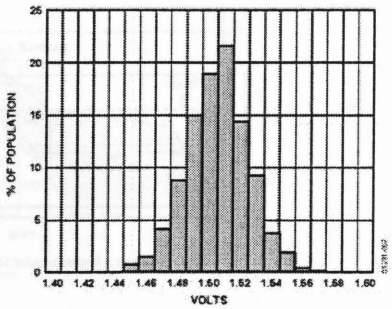

Figure 7. Y-Axis Zero g Bias at 25°C

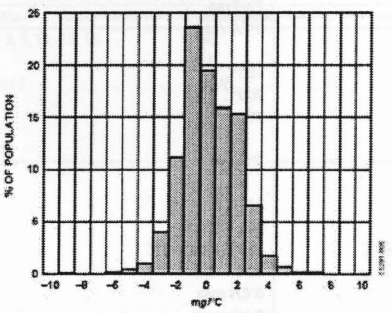

Figure 5. X-Axis Zero g Bias Temperature Coefficient

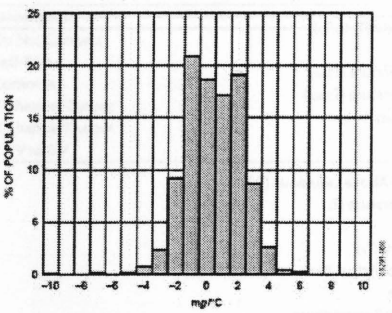

Figure 8. Y-Axis Zero g Bias Temperature Coefficient

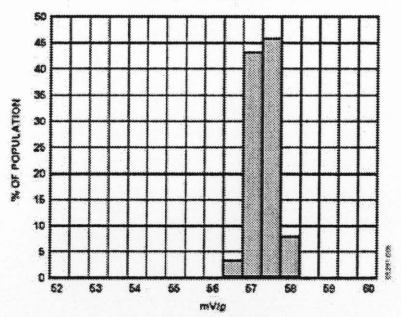

Figure 6. X-Axis Sensitivity at 25°C

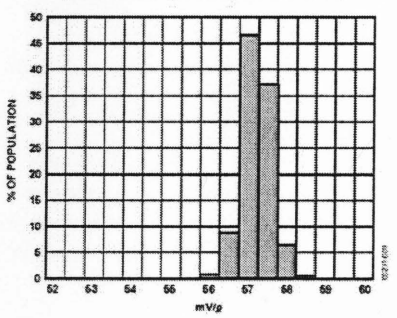

Figure 9. Y-Axis Sensitivity at 25°C

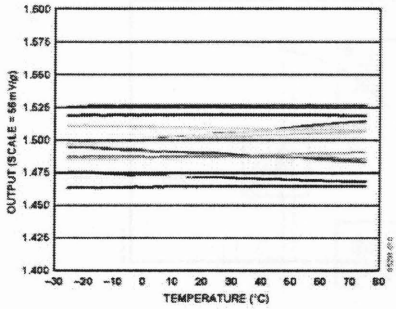

Figure 10. Zero g Bias vs. Temperature—Parts Soldered to PCB

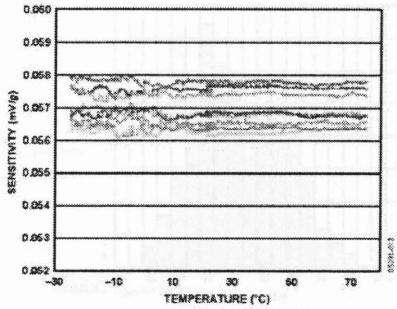

Figure 13. Sensitivity vs. Temperature—Parts Soldered to PCB

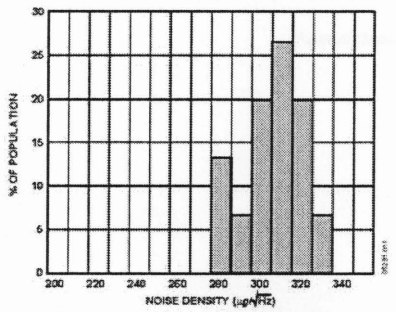

Figure 11. X-Axis Noise Density at 25°C

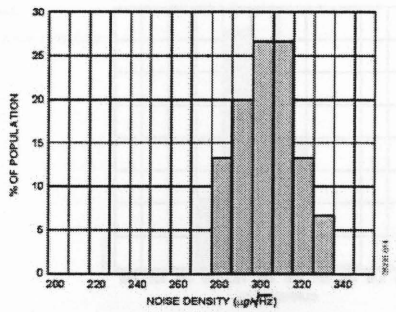

Figure 14. Y-Axis Noise Density at 25°C

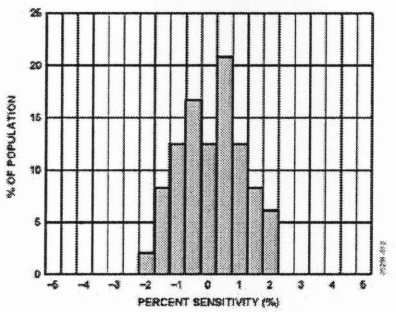

Figure 12. Z vs. X Cross-Axis Sensitivity

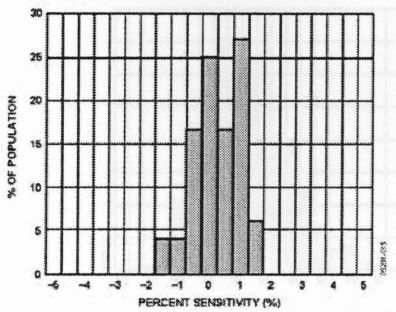

Figure 15. Z vs. Y Cross-Axis Sensitivity

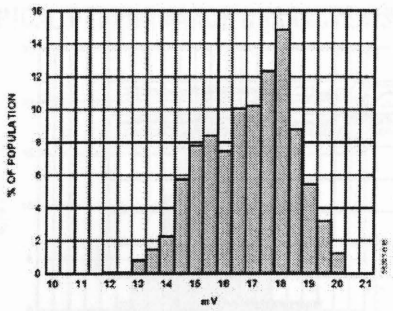

Figure 16. X-Axis Self-Test Response at 25°C

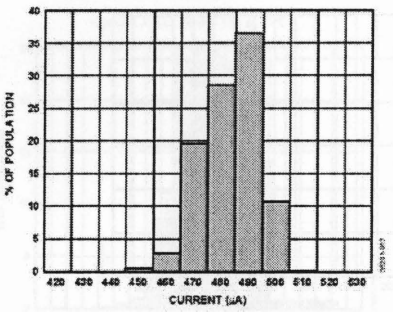

Figure 17. Supply Current at 25°C

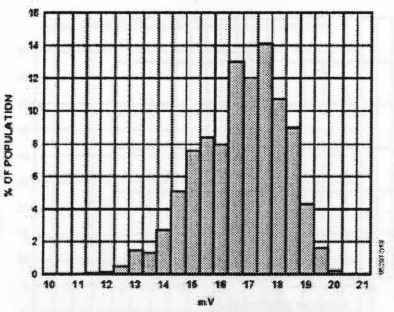

Figure 18. Y-Axis Self-Test Response at 25°C

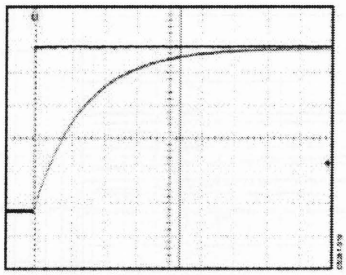

Figure 19. Turn-On Time—C_X, C_Y = 0.1 µF, Time Scale = 2 ms/DIV

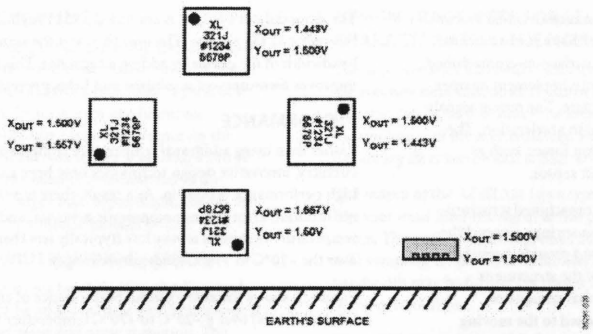

Figure 20. Output Response vs. Orientation (Top View)

THEORY OF OPERATION

The ADXL321 is a complete acceleration measurement system on a single monolithic IC. The ADXL321 has a measurement range of ±18 *g*. It contains a polysilicon surface-micromachined sensor and signal conditioning circuitry to implement an open-loop acceleration measurement architecture. The output signals are analog voltages that are proportional to acceleration. The accelerometer measures static acceleration forces, such as gravity, which allows it to be used as a tilt sensor.

The sensor is a polysilicon surface-micromachined structure built on top of a silicon wafer. Polysilicon springs suspend the structure over the surface of the wafer and provide a resistance against acceleration forces. Deflection of the structure is measured using a differential capacitor that consists of independent fixed plates and plates attached to the moving mass. The fixed plates are driven by 180° out-of-phase square waves. Acceleration deflects the beam and unbalances the differential capacitor, resulting in an output square wave whose amplitude is proportional to acceleration. Phase-sensitive demodulation techniques are then used to rectify the signal and determine the direction of the acceleration.

The demodulator's output is amplified and brought off-chip through a 32 kΩ resistor. The user then sets the signal bandwidth of the device by adding a capacitor. This filtering improves measurement resolution and helps prevent aliasing.

PERFORMANCE

Rather than using additional temperature compensation circuitry, innovative design techniques have been used to ensure high performance is built-in. As a result, there is neither quantization error nor nonmonotonic behavior, and temperature hysteresis is very low (typically less than 10 mg over the −20°C to +70°C temperature range).

Figure 10 shows the zero *g* output performance of eight parts (X- and Y-axis) over a −20°C to +70°C temperature range.

Figure 13 demonstrates the typical sensitivity shift over temperature for supply voltages of 3 V. This is typically better than ±1% over the −20°C to +70°C temperature range.

APPLICATIONS

POWER SUPPLY DECOUPLING

For most applications, a single 0.1 µF capacitor, C_{DC}, adequately decouples the accelerometer from noise on the power supply. However, in some cases, particularly where noise is present at the 140 kHz internal clock frequency (or any harmonic thereof), noise on the supply may cause interference on the ADXL321 output. If additional decoupling is needed, a 100 Ω (or smaller) resistor or ferrite bead may be inserted in the supply line. Additionally, a larger bulk bypass capacitor (in the 1 µF to 4.7 µF range) may be added in parallel to C_{DC}.

SETTING THE BANDWIDTH USING C_X AND C_Y

The ADXL321 has provisions for band-limiting the X_{OUT} and Y_{OUT} pins. Capacitors must be added at these pins to implement low-pass filtering for antialiasing and noise reduction. The equation for the 3 dB bandwidth is

$$F_{-3\,dB} = 1/(2\pi(32\ k\Omega) \times C_{(X,Y)})$$

or more simply,

$$F_{-3\,dB} = 5\ \mu F/C_{(X,Y)}$$

The tolerance of the internal resistor (R_{FILT}) typically varies as much as ±15% of its nominal value (32 kΩ), and the bandwidth varies accordingly. A minimum capacitance of 2000 pF for C_X and C_Y is required in all cases.

Table 5. Filter Capacitor Selection, C_X and C_Y

Bandwidth (Hz)	Capacitor (µF)
1	4.7
10	0.47
50	0.10
100	0.05
200	0.027
500	0.01

SELF-TEST

The ST pin controls the self-test feature. When this pin is set to V_S, an electrostatic force is exerted on the accelerometer beam. The resulting movement of the beam allows the user to test if the accelerometer is functional. The typical change in output is 315 mg (corresponding to 18 mV). This pin may be left open-circuit or connected to common (COM) in normal use.

The ST pin should never be exposed to voltages greater than V_S + 0.3 V. If this cannot be guaranteed due to the system design (for instance, if there are multiple supply voltages), then a low V_F clamping diode between ST and V_S is recommended.

DESIGN TRADE-OFFS FOR SELECTING FILTER CHARACTERISTICS: THE NOISE/BW TRADE-OFF

The accelerometer bandwidth selected ultimately determines the measurement resolution (smallest detectable acceleration). Filtering can be used to lower the noise floor, which improves the resolution of the accelerometer. Resolution is dependent on the analog filter bandwidth at X_{OUT} and Y_{OUT}.

The output of the ADXL321 has a typical bandwidth of 2.5 kHz. The user must filter the signal at this point to limit aliasing errors. The analog bandwidth must be no more than half the A/D sampling frequency to minimize aliasing. The analog bandwidth may be further decreased to reduce noise and improve resolution.

The ADXL321 noise has the characteristics of white Gaussian noise, which contributes equally at all frequencies and is described in terms of µg/√Hz (the noise is proportional to the square root of the accelerometer's bandwidth). The user should limit bandwidth to the lowest frequency needed by the application in order to maximize the resolution and dynamic range of the accelerometer.

With the single-pole, roll-off characteristic, the typical noise of the ADXL321 is determined by

$$rmsNoise = (320\ \mu g/\sqrt{Hz}) \times (\sqrt{BW \times 1.6})$$

At 100 Hz bandwidth the noise will be

$$rmsNoise = (320\ \mu g/\sqrt{Hz}) \times (\sqrt{100 \times 1.6}) = 4\ mg$$

Often, the peak value of the noise is desired. Peak-to-peak noise can only be estimated by statistical methods. A factor of 6 is generally used to convert rms to peak-to-peak. Table 6 is useful for estimating the probabilities of exceeding various peak values, given the rms value.

Table 6. Estimation of Peak-to-Peak Noise

Peak-to-Peak Value	% of Time That Noise Exceeds Nominal Peak-to-Peak Value
2 × rms	32
4 × rms	4.6
6 × rms	0.27
8 × rms	0.006

Peak-to-peak noise values give the best estimate of the uncertainty in a single measurement. Table 7 gives the typical noise output of the ADXL321 for various C_X and C_Y values.

Table 7. Filter Capacitor Selection (C_X, C_Y)

Bandwidth (Hz)	C_X, C_Y (μF)	RMS Noise (*mg*)	Peak-to-Peak Noise Estimate (*mg*)
10	0.47	1.3	7.8
50	0.1	2.9	17.4
100	0.047	4	24
500	0.01	9.1	54.6

USE WITH OPERATING VOLTAGES OTHER THAN 3 V

The ADXL321 is tested and specified at V_S = 3 V; however, it can be powered with V_S as low as 2.4 V or as high as 6 V. Note that some performance parameters change as the supply voltage is varied.

The ADXL321 output is ratiometric, so the sensitivity (or scale factor) varies proportionally to supply voltage. At V_S = 5 V, the sensitivity is typically 100 mV/*g*. At V_S = 2.4 V, the sensitivity is typically 45 mV/*g*.

The zero *g* bias output is also ratiometric, so the zero *g* output is nominally equal to $V_S/2$ at all supply voltages.

The output noise is not ratiometric but is absolute in volts; therefore, the noise density decreases as the supply voltage increases. This is because the scale factor (mV/*g*) increases while the noise voltage remains constant. At V_S = 5 V, the noise density is typically 190 μ*g*/√Hz, while at V_S = 2.4 V, the noise density is typically 400 μ*g*/√Hz.

Self-test response in *g* is roughly proportional to the square of the supply voltage. However, when ratiometricity of sensitivity is factored in with supply voltage, the self-test response in volts is roughly proportional to the cube of the supply voltage. For example, at V_S = 5 V, the self-test response for the ADXL321 is approximately 80 mV. At V_S = 2.4 V, the self-test response is approximately 8 mV.

The supply current decreases as the supply voltage decreases. Typical current consumption at V_S = 5 V is 750 μA, and typical current consumption at V_S = 2.4 V is 350 μA.

USE AS A DUAL-AXIS TILT SENSOR

An accelerometer is most sensitive to tilt when its sensitive axis is perpendicular to the force of gravity (that is, when it is parallel to the earth's surface). At this orientation, its sensitivity to changes in tilt is highest. When the accelerometer is oriented on axis to gravity (near its +1 *g* or −1 *g* reading), the change in output acceleration per degree of tilt is negligible. When the accelerometer is perpendicular to gravity, its output changes nearly 17.5 *mg* per degree of tilt. At 45°, its output changes at only 12.2 *mg* per degree of tilt, and resolution declines.

Converting Acceleration to Tilt

When the accelerometer is oriented so both its X-axis and Y-axis are parallel to the earth's surface, it can be used as a 2-axis tilt sensor with both a roll axis and pitch axis. Once the output signal from the accelerometer has been converted to an acceleration that varies between −1 *g* and +1 *g*, the output tilt in degrees is calculated as

$$PITCH = \arcsin(A_X/1\ g)$$

$$ROLL = \arcsin(A_Y/1\ g)$$

Be sure to account for overranges. It is possible for the accelerometers to output a signal greater than ±1 *g* due to vibration, shock, or other accelerations.

OUTLINE DIMENSIONS

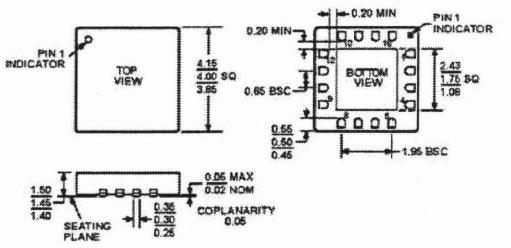

Figure 21. 16-Lead Lead Frame Chip Scale Package [LFCSP_LQ]
4 mm × 4 mm Body, Thick Quad
(CP-16-5a)*
Dimensions shown in millimeters
(Drawing Not to Scale)

ORDERING GUIDE

Model	Measurement Range	Specified Voltage (V)	Temperature Range	Package Description	Package Option
ADXL321JCP[1]	±18 *g*	3	−20°C to +70°C	16-Lead LFCSP_LQ	CP-16-5a
ADXL321JCP-REEL	±18 *g*	3	−20°C to +70°C	16-Lead LFCSP_LQ	CP-16-5a
ADXL321EB				Evaluation Board	

[1] Lead finish—Matte tin.

NOTES

NOTES

Appendix C

Data sheet for ADXL335 tri-axial accelerometer used on thin plate

Small, Low Power, 3-Axis ±3 *g* Accelerometer

ADXL335

FEATURES

- 3-axis sensing
- Small, low profile package
  - 4 mm × 4 mm × 1.45 mm LFCSP
- Low power : 350 µA (typical)
- Single-supply operation: 1.8 V to 3.6 V
- 10,000 *g* shock survival
- Excellent temperature stability
- BW adjustment with a single capacitor per axis
- RoHS/WEEE lead-free compliant

APPLICATIONS

- Cost sensitive, low power, motion- and tilt-sensing applications
  - Mobile devices
  - Gaming systems
  - Disk drive protection
  - Image stabilization
  - Sports and health devices

GENERAL DESCRIPTION

The ADXL335 is a small, thin, low power, complete 3-axis accelerometer with signal conditioned voltage outputs. The product measures acceleration with a minimum full-scale range of ±3 *g*. It can measure the static acceleration of gravity in tilt-sensing applications, as well as dynamic acceleration resulting from motion, shock, or vibration.

The user selects the bandwidth of the accelerometer using the C_X, C_Y, and C_Z capacitors at the X_{OUT}, Y_{OUT}, and Z_{OUT} pins. Bandwidths can be selected to suit the application, with a range of 0.5 Hz to 1600 Hz for the X and Y axes, and a range of 0.5 Hz to 550 Hz for the Z axis.

The ADXL335 is available in a small, low profile, 4 mm × 4 mm × 1.45 mm, 16-lead, plastic lead frame chip scale package (LFCSP_LQ).

FUNCTIONAL BLOCK DIAGRAM

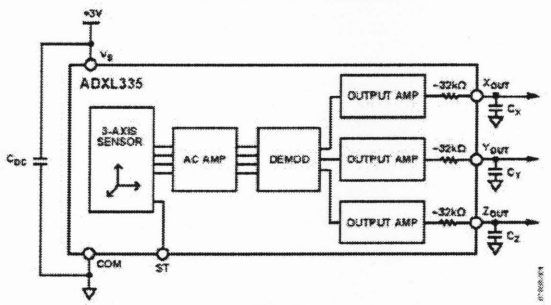

Figure 1.

One Technology Way, P.O. Box 9106, Norwood, MA 02062-9106, U.S.A.
Tel: 781.329.4700 www.analog.com
Fax: 781.461.3113

TABLE OF CONTENTS

REVISION HISTORY

1/09—Revision 0: Initial Version

SPECIFICATIONS

T_A = 25°C, V_S = 3 V, C_X = C_Y = C_Z = 0.1 µF, acceleration = 0 *g*, unless otherwise noted. All minimum and maximum specifications are guaranteed. Typical specifications are not guaranteed.

Table 1.

Parameter	Conditions	Min	Typ	Max	Unit
SENSOR INPUT	Each axis				
Measurement Range		±3	±3.6		*g*
Nonlinearity	% of full scale		±0.3		%
Package Alignment Error			±1		Degrees
Interaxis Alignment Error			±0.1		Degrees
Cross-Axis Sensitivity[1]			±1		%
SENSITIVITY (RATIOMETRIC)[2]	Each axis				
Sensitivity at X_{OUT}, Y_{OUT}, Z_{OUT}	V_S = 3 V	270	300	330	mV/*g*
Sensitivity Change Due to Temperature[3]	V_S = 3 V		±0.01		%/°C
ZERO *g* BIAS LEVEL (RATIOMETRIC)					
0 *g* Voltage at X_{OUT}, Y_{OUT}	V_S = 3 V	1.35	1.5	1.65	V
0 *g* Voltage at Z_{OUT}	V_S = 3 V	1.2	1.5	1.8	V
0 *g* Offset vs. Temperature			±1		mg/°C
NOISE PERFORMANCE					
Noise Density X_{OUT}, Y_{OUT}			150		µg/√Hz rms
Noise Density Z_{OUT}			300		µg/√Hz rms
FREQUENCY RESPONSE[4]					
Bandwidth X_{OUT}, Y_{OUT}[5]	No external filter		1600		Hz
Bandwidth Z_{OUT}[5]	No external filter		550		Hz
R_{FILT} Tolerance			32 ± 15%		kΩ
Sensor Resonant Frequency			5.5		kHz
SELF-TEST[6]					
Logic Input Low			+0.6		V
Logic Input High			+2.4		V
ST Actuation Current			+60		µA
Output Change at X_{OUT}	Self-Test 0 to Self-Test 1	−150	−325	−600	mV
Output Change at Y_{OUT}	Self-Test 0 to Self-Test 1	+150	+325	+600	mV
Output Change at Z_{OUT}	Self-Test 0 to Self-Test 1	+150	+550	+1000	mV
OUTPUT AMPLIFIER					
Output Swing Low	No load		0.1		V
Output Swing High	No load		2.8		V
POWER SUPPLY					
Operating Voltage Range		1.8		3.6	V
Supply Current	V_S = 3 V		350		µA
Turn-On Time[7]	No external filter		1		ms
TEMPERATURE					
Operating Temperature Range		−40		+85	°C

[1] Defined as coupling between any two axes.
[2] Sensitivity is essentially ratiometric to V_S.
[3] Defined as the output change from ambient-to-maximum temperature or ambient-to-minimum temperature.
[4] Actual frequency response controlled by user-supplied external filter capacitors (C_X, C_Y, C_Z).
[5] Bandwidth with external capacitors = 1/(2 × π × 32 kΩ × C). For C_X, C_Y = 0.003 µF, bandwidth = 1.6 kHz. For C_Z = 0.01 µF, bandwidth = 500 Hz. For C_X, C_Y, C_Z = 10 µF, bandwidth = 0.5 Hz.
[6] Self-test response changes cubically with V_S.
[7] Turn-on time is dependent on C_X, C_Y, C_Z and is approximately 160 × C_X or C_Y or C_Z + 1 ms, where C_X, C_Y, C_Z are in microfarads (µF).

ABSOLUTE MAXIMUM RATINGS

Table 2.

Parameter	Rating
Acceleration (Any Axis, Unpowered)	10,000 *g*
Acceleration (Any Axis, Powered)	10,000 *g*
V_S	−0.3 V to +3.6 V
All Other Pins	(COM − 0.3 V) to (V_S + 0.3 V)
Output Short-Circuit Duration (Any Pin to Common)	Indefinite
Temperature Range (Powered)	−55°C to +125°C
Temperature Range (Storage)	−65°C to +150°C

Stresses above those listed under Absolute Maximum Ratings may cause permanent damage to the device. This is a stress rating only; functional operation of the device at these or any other conditions above those indicated in the operational section of this specification is not implied. Exposure to absolute maximum rating conditions for extended periods may affect device reliability.

ESD CAUTION

ESD (electrostatic discharge) sensitive device. Charged devices and circuit boards can discharge without detection. Although this product features patented or proprietary protection circuitry, damage may occur on devices subjected to high energy ESD. Therefore, proper ESD precautions should be taken to avoid performance degradation or loss of functionality.

PIN CONFIGURATION AND FUNCTION DESCRIPTIONS

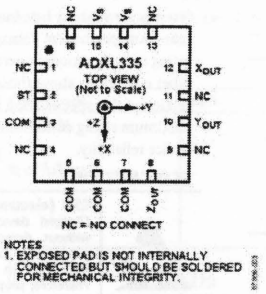

Figure 2. Pin Configuration

Table 3. Pin Function Descriptions

Pin No.	Mnemonic	Description
1	NC	No Connect[1].
2	ST	Self-Test.
3	COM	Common.
4	NC	No Connect[1].
5	COM	Common.
6	COM	Common.
7	COM	Common.
8	Z_{OUT}	Z Channel Output.
9	NC	No Connect[1].
10	Y_{OUT}	Y Channel Output.
11	NC	No Connect[1].
12	X_{OUT}	X Channel Output.
13	NC	No Connect[1].
14	V_S	Supply Voltage (1.8 V to 3.6 V).
15	V_S	Supply Voltage (1.8 V to 3.6 V).
16	NC	No Connect[1].
EP	Exposed Pad	Not internally connected. Solder for mechanical integrity.

[1]NC pins are not internally connected and can be tied to COM pins, unless otherwise noted.

TYPICAL PERFORMANCE CHARACTERISTICS

N > 1000 for all typical performance plots, unless otherwise noted.

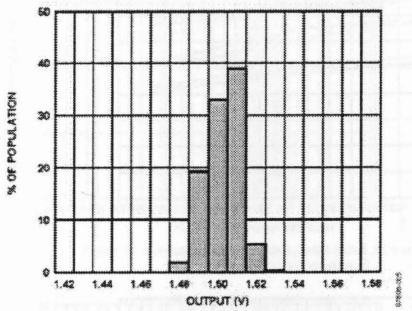

Figure 3. X-Axis Zero g Bias at 25°C, V_S = 3 V

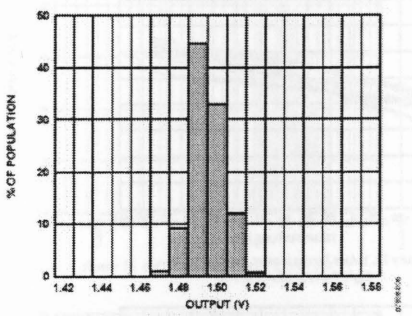

Figure 4. Y-Axis Zero g Bias at 25°C, V_S = 3 V

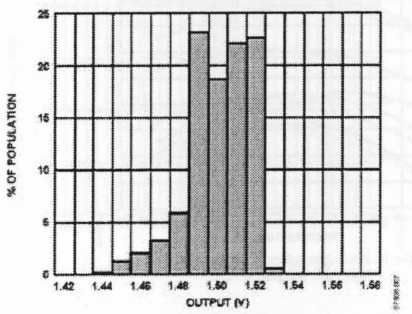

Figure 5. Z-Axis Zero g Bias at 25°C, V_S = 3 V

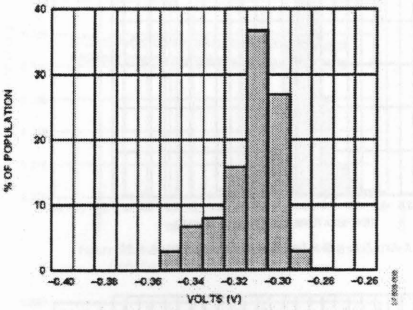

Figure 6. X-Axis Self-Test Response at 25°C, V_S = 3 V

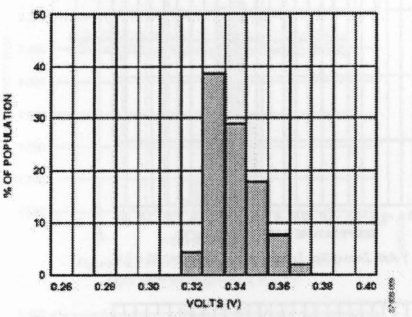

Figure 7. Y-Axis Self-Test Response at 25°C, V_S = 3 V

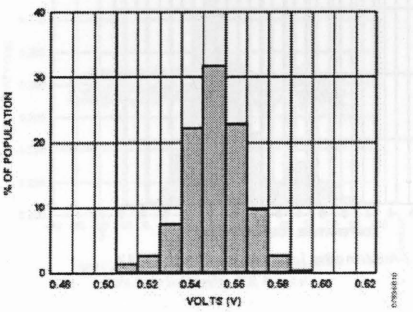

Figure 8. Z-Axis Self-Test Response at 25°C, V_S = 3 V

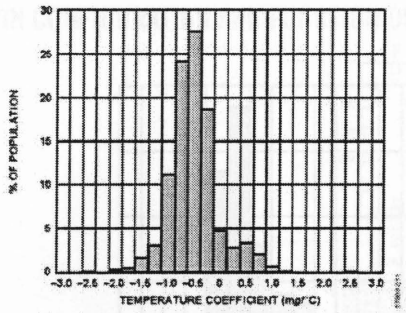

Figure 9. X-Axis Zero g Bias Temperature Coefficient, V_S = 3 V

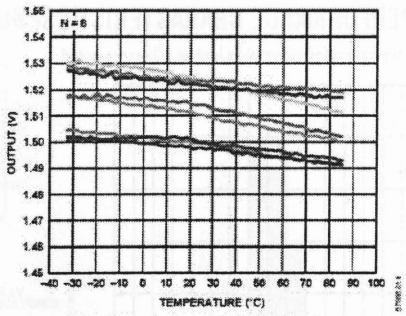

Figure 12. X-Axis Zero g Bias vs. Temperature—Eight Parts Soldered to PCB

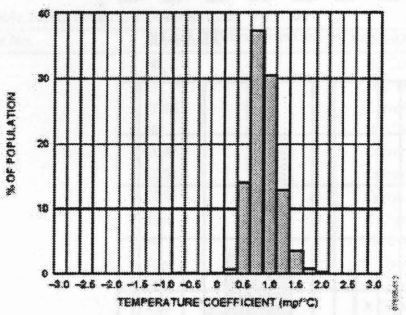

Figure 10. Y-Axis Zero g Bias Temperature Coefficient, V_S = 3 V

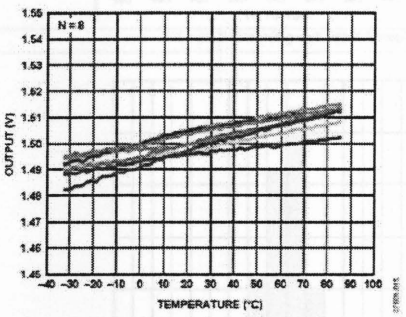

Figure 13. Y-Axis Zero g Bias vs. Temperature—Eight Parts Soldered to PCB

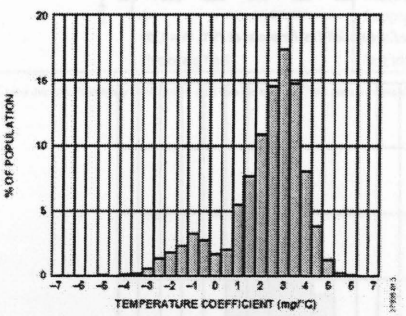

Figure 11. Z-Axis Zero g Bias Temperature Coefficient, V_S = 3 V

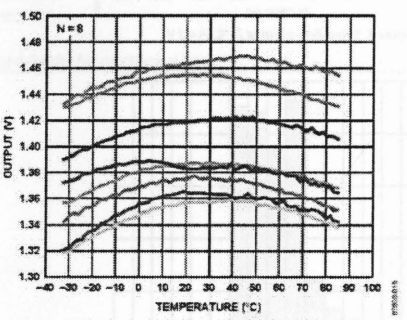

Figure 14. Z-Axis Zero g Bias vs. Temperature—Eight Parts Soldered to PCB

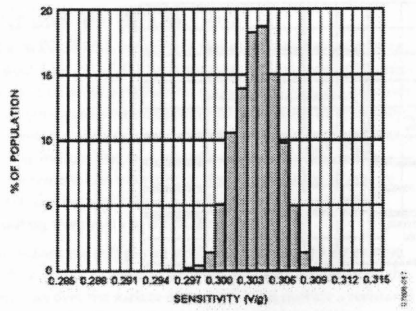

Figure 15. X-Axis Sensitivity at 25°C, V_S = 3 V

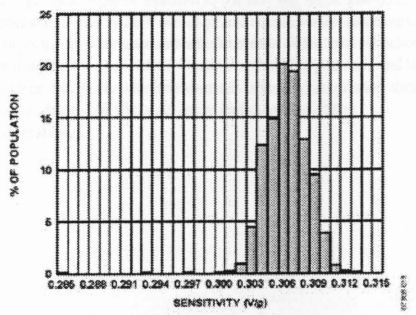

Figure 16. Y-Axis Sensitivity at 25°C, V_S = 3 V

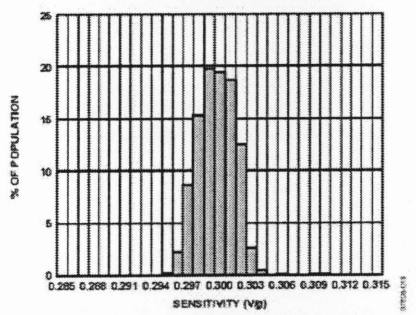

Figure 17. Z-Axis Sensitivity at 25°C, V_S = 3 V

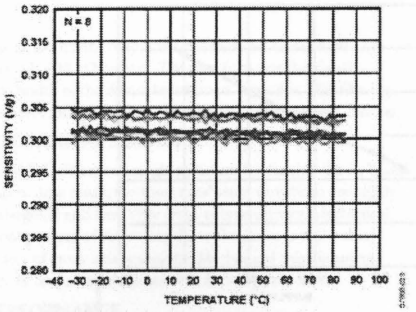

Figure 18. X-Axis Sensitivity vs. Temperature—Eight Parts Soldered to PCB, V_S = 3 V

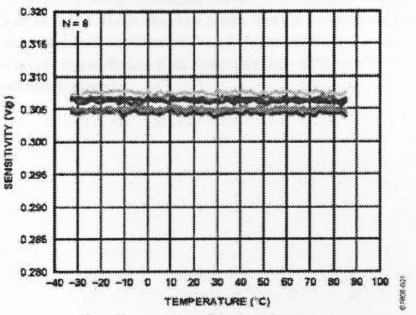

Figure 19. Y-Axis Sensitivity vs. Temperature—Eight Parts Soldered to PCB, V_S = 3 V

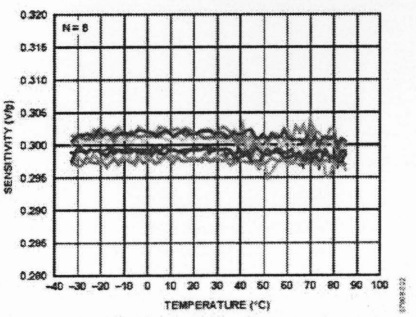

Figure 20. Z-Axis Sensitivity vs. Temperature—Eight Parts Soldered to PCB, V_S = 3 V

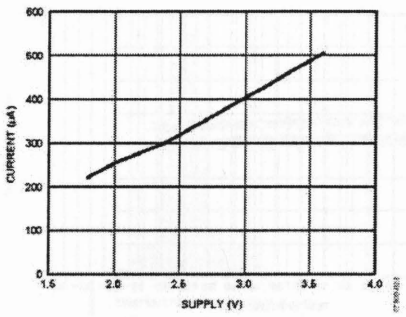

Figure 21. Typical Current Consumption vs. Supply Voltage

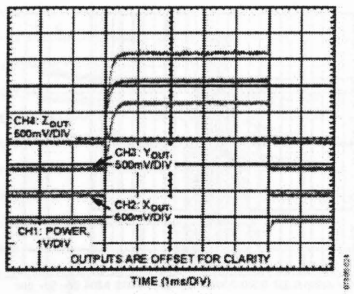

Figure 22. Typical Turn-On Time, V_S = 3 V

THEORY OF OPERATION

The ADXL335 is a complete 3-axis acceleration measurement system. The ADXL335 has a measurement range of ±3 g minimum. It contains a polysilicon surface-micromachined sensor and signal conditioning circuitry to implement an open-loop acceleration measurement architecture. The output signals are analog voltages that are proportional to acceleration. The accelerometer can measure the static acceleration of gravity in tilt-sensing applications as well as dynamic acceleration resulting from motion, shock, or vibration.

The sensor is a polysilicon surface-micromachined structure built on top of a silicon wafer. Polysilicon springs suspend the structure over the surface of the wafer and provide a resistance against acceleration forces. Deflection of the structure is measured using a differential capacitor that consists of independent fixed plates and plates attached to the moving mass. The fixed plates are driven by 180° out-of-phase square waves. Acceleration deflects the moving mass and unbalances the differential capacitor resulting in a sensor output whose amplitude is proportional to acceleration. Phase-sensitive demodulation techniques are then used to determine the magnitude and direction of the acceleration.

The demodulator output is amplified and brought off-chip through a 32 kΩ resistor. The user then sets the signal bandwidth of the device by adding a capacitor. This filtering improves measurement resolution and helps prevent aliasing.

MECHANICAL SENSOR

The ADXL335 uses a single structure for sensing the X, Y, and Z axes. As a result, the three axes' sense directions are highly orthogonal and have little cross-axis sensitivity. Mechanical misalignment of the sensor die to the package is the chief source of cross-axis sensitivity. Mechanical misalignment can, of course, be calibrated out at the system level.

PERFORMANCE

Rather than using additional temperature compensation circuitry, innovative design techniques ensure that high performance is built in to the ADXL335. As a result, there is no quantization error or nonmonotonic behavior, and temperature hysteresis is very low (typically less than 3 mg over the −25°C to +70°C temperature range).

APPLICATIONS INFORMATION

POWER SUPPLY DECOUPLING

For most applications, a single 0.1 µF capacitor, C_{DC}, placed close to the ADXL335 supply pins adequately decouples the accelerometer from noise on the power supply. However, in applications where noise is present at the 50 kHz internal clock frequency (or any harmonic thereof), additional care in power supply bypassing is required because this noise can cause errors in acceleration measurement.

If additional decoupling is needed, a 100 Ω (or smaller) resistor or ferrite bead can be inserted in the supply line. Additionally, a larger bulk bypass capacitor (1 µF or greater) can be added in parallel to C_{DC}. Ensure that the connection from the ADXL335 ground to the power supply ground is low impedance because noise transmitted through ground has a similar effect to noise transmitted through V_S.

SETTING THE BANDWIDTH USING C_X, C_Y, AND C_Z

The ADXL335 has provisions for band limiting the X_{OUT}, Y_{OUT}, and Z_{OUT} pins. Capacitors must be added at these pins to implement low-pass filtering for antialiasing and noise reduction. The equation for the 3 dB bandwidth is

$$F_{-3\,dB} = 1/(2\pi(32\ k\Omega) \times C_{(X,Y,Z)})$$

or more simply

$$F_{-3\,dB} = 5\ \mu F/C_{(X,Y,Z)}$$

The tolerance of the internal resistor (R_{FILT}) typically varies as much as ±15% of its nominal value (32 kΩ), and the bandwidth varies accordingly. A minimum capacitance of 0.0047 µF for C_X, C_Y, and C_Z is recommended in all cases.

Table 4. Filter Capacitor Selection, C_X, C_Y, and C_Z

Bandwidth (Hz)	Capacitor (µF)
1	4.7
10	0.47
50	0.10
100	0.05
200	0.027
500	0.01

SELF-TEST

The ST pin controls the self-test feature. When this pin is set to V_S, an electrostatic force is exerted on the accelerometer beam. The resulting movement of the beam allows the user to test if the accelerometer is functional. The typical change in output is −1.08 *g* (corresponding to −325 mV) in the X-axis, +1.08 *g* (or +325 mV) on the Y-axis, and +1.83 *g* (or +550 mV) on the Z-axis. This ST pin can be left open-circuit or connected to common (COM) in normal use.

Never expose the ST pin to voltages greater than V_S + 0.3 V. If this cannot be guaranteed due to the system design (for instance, if there are multiple supply voltages), then a low V_F clamping diode between ST and V_S is recommended.

DESIGN TRADE-OFFS FOR SELECTING FILTER CHARACTERISTICS: THE NOISE/BW TRADE-OFF

The selected accelerometer bandwidth ultimately determines the measurement resolution (smallest detectable acceleration). Filtering can be used to lower the noise floor to improve the resolution of the accelerometer. Resolution is dependent on the analog filter bandwidth at X_{OUT}, Y_{OUT}, and Z_{OUT}.

The output of the ADXL335 has a typical bandwidth of greater than 500 Hz. The user must filter the signal at this point to limit aliasing errors. The analog bandwidth must be no more than half the analog-to-digital sampling frequency to minimize aliasing. The analog bandwidth can be further decreased to reduce noise and improve resolution.

The ADXL335 noise has the characteristics of white Gaussian noise, which contributes equally at all frequencies and is described in terms of µg/√Hz (the noise is proportional to the square root of the accelerometer bandwidth). The user should limit bandwidth to the lowest frequency needed by the application to maximize the resolution and dynamic range of the accelerometer.

With the single-pole, roll-off characteristic, the typical noise of the ADXL335 is determined by

$$rms\ Noise = Noise\ Density \times (\sqrt{BW \times 1.6})$$

It is often useful to know the peak value of the noise. Peak-to-peak noise can only be estimated by statistical methods. Table 5 is useful for estimating the probabilities of exceeding various peak values, given the rms value.

Table 5. Estimation of Peak-to-Peak Noise

Peak-to-Peak Value	% of Time That Noise Exceeds Nominal Peak-to-Peak Value
2 × rms	32
4 × rms	4.6
6 × rms	0.27
8 × rms	0.006

USE WITH OPERATING VOLTAGES OTHER THAN 3 V

The ADXL335 is tested and specified at V_S = 3 V; however, it can be powered with V_S as low as 1.8 V or as high as 3.6 V. Note that some performance parameters change as the supply voltage is varied.

The ADXL335 output is ratiometric, therefore, the output sensitivity (or scale factor) varies proportionally to the supply voltage. At V_S = 3.6 V, the output sensitivity is typically 360 mV/*g*. At V_S = 2 V, the output sensitivity is typically 195 mV/*g*.

The zero *g* bias output is also ratiometric, thus the zero *g* output is nominally equal to V_S/2 at all supply voltages.

The output noise is not ratiometric but is absolute in volts; therefore, the noise density decreases as the supply voltage increases. This is because the scale factor (mV/*g*) increases while the noise voltage remains constant. At V_S = 3.6 V, the X-axis and Y-axis noise density is typically 120 μ*g*/√Hz, whereas at V_S = 2 V, the X-axis and Y-axis noise density is typically 270 μ*g*/√Hz.

Self-test response in *g* is roughly proportional to the square of the supply voltage. However, when ratiometricity of sensitivity is factored in with supply voltage, the self-test response in volts is roughly proportional to the cube of the supply voltage. For example, at V_S = 3.6 V, the self-test response for the ADXL335 is approximately −560 mV for the X-axis, +560 mV for the Y-axis, and +950 mV for the Z-axis.

At V_S = 2 V, the self-test response is approximately −96 mV for the X-axis, +96 mV for the Y-axis, and −163 mV for the Z-axis.

The supply current decreases as the supply voltage decreases. Typical current consumption at V_S = 3.6 V is 375 μA, and typical current consumption at V_S = 2 V is 200 μA.

AXES OF ACCELERATION SENSITIVITY

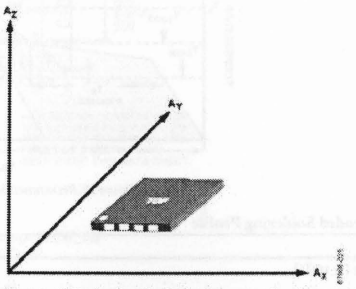

Figure 23. Axes of Acceleration Sensitivity; Corresponding Output Voltage Increases When Accelerated Along the Sensitive Axis.

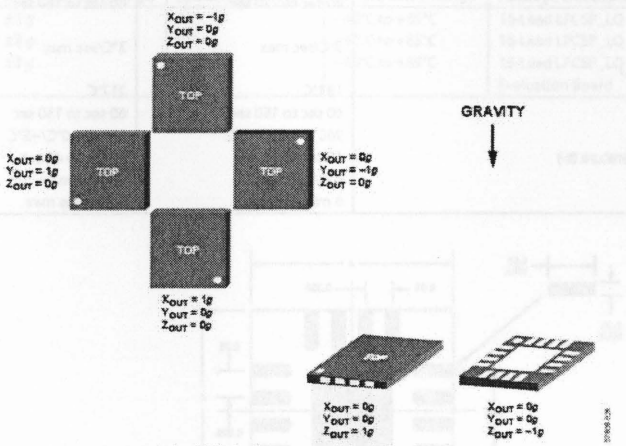

Figure 24. Output Response vs. Orientation to Gravity

LAYOUT AND DESIGN RECOMMENDATIONS

The recommended soldering profile is shown in Figure 25 followed by a description of the profile features in Table 6. The recommended PCB layout or solder land drawing is shown in Figure 26.

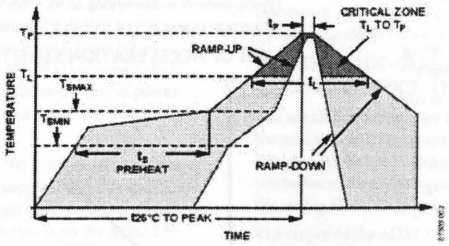

Figure 25. Recommended Soldering Profile

Table 6. Recommended Soldering Profile

Profile Feature	Sn63/Pb37	Pb-Free
Average Ramp Rate (T_L to T_P)	3°C/sec max	3°C/sec max
Preheat		
Minimum Temperature (T_{SMIN})	100°C	150°C
Maximum Temperature (T_{SMAX})	150°C	200°C
Time (T_{SMIN} to T_{SMAX})(t_S)	60 sec to 120 sec	60 sec to 180 sec
T_{SMAX} to T_L		
Ramp-Up Rate	3°C/sec max	3°C/sec max
Time Maintained Above Liquidous (T_L)		
Liquidous Temperature (T_L)	183°C	217°C
Time (t_L)	60 sec to 150 sec	60 sec to 150 sec
Peak Temperature (T_P)	240°C + 0°C/−5°C	260°C + 0°C/−5°C
Time Within 5°C of Actual Peak Temperature (t_P)	10 sec to 30 sec	20 sec to 40 sec
Ramp-Down Rate	6°C/sec max	6°C/sec max
Time 25°C to Peak Temperature	6 minutes max	8 minutes max

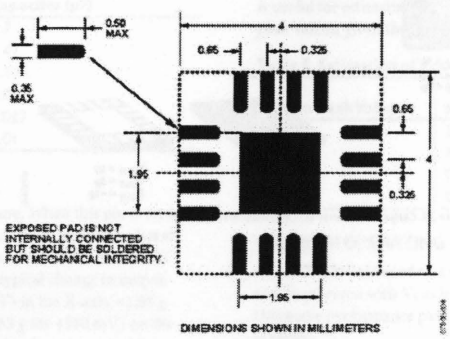

Figure 26. Recommended PCB Layout

OUTLINE DIMENSIONS

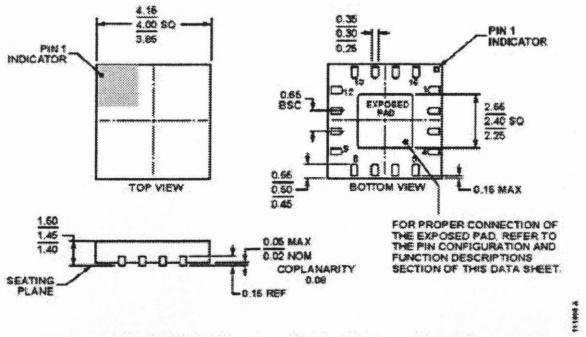

Figure 27. 16-Lead Lead Frame Chip Scale Package [LFCSP_LQ]
4 mm × 4 mm Body, 1.45 mm Thick Quad
(CP-16-14)
Dimensions shown in millimeters

ORDERING GUIDE

Model	Measurement Range	Specified Voltage	Temperature Range	Package Description	Package Option
ADXL335BCPZ[1]	±3 *g*	3 V	−40°C to +85°C	16-Lead LFCSP_LQ	CP-16-14
ADXL335BCPZ-RL[1]	±3 *g*	3 V	−40°C to +85°C	16-Lead LFCSP_LQ	CP-16-14
ADXL335BCPZ-RL7[1]	±3 *g*	3 V	−40°C to +85°C	16-Lead LFCSP_LQ	CP-16-14
EVAL-ADXL335Z[2]				Evaluation Board	

[1] Z = RoHS Compliant Part.

NOTES

NOTES

Appendix D

Tensile test results and technical data for Silicone 70 cord stock

The density of the material was determined by using two samples of different cut lengths and weighed on an electronic balance with least count of 1 micro gram obtaining three readings each. Average density was found to be 1590.5 Kg/m^3.

Similarly, a tensile test was carried out on a United Testing Systems machine of 50 kN capacity. Extensiometer was set to 2 inch in length and attached to the silicon rubber chord stock of 8 inch-long specimen and clamped in the jaws while the specimen was subjected to axial load. Application of load was continued till the specimen failed while the extensiometer was removed at 20% strain and the data was plotted to construct the stress-strain curve. Numerically a linear regression was carried on the data and a best fit curve plotted as shown in below Figure D-1. Young's modulus of elasticity was determined to be 1006.6 PSi ~ 6.94 MPa

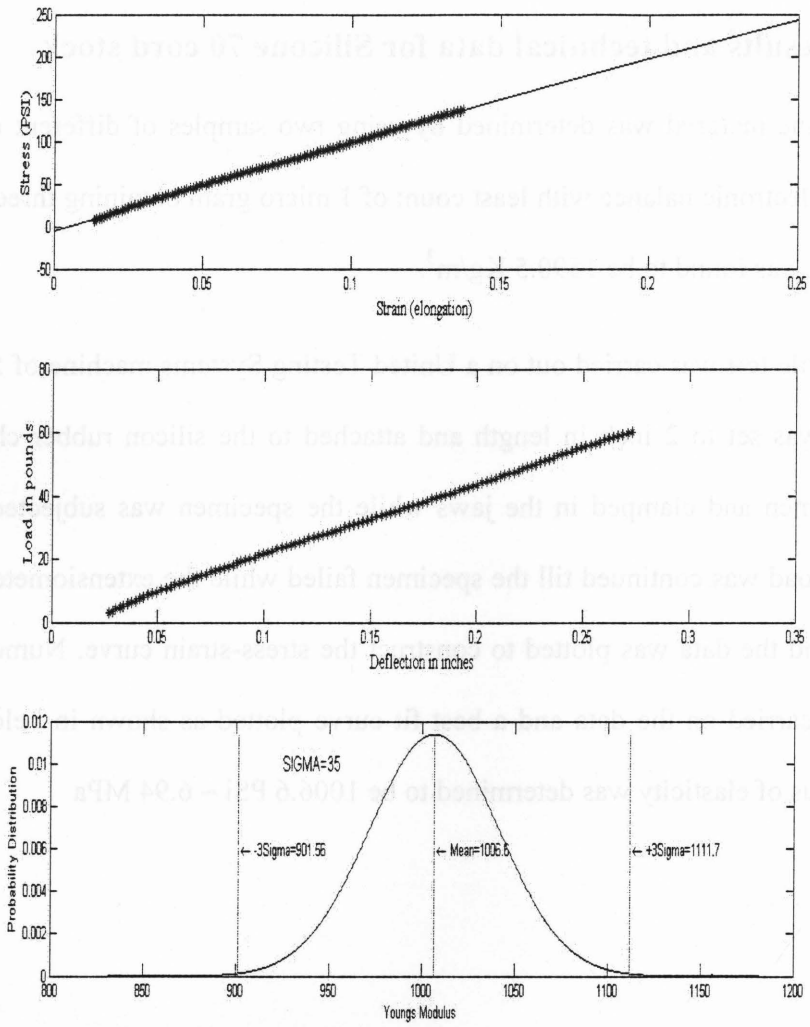

Figure D-1 Experimental values of modulus of elasticity for silicon rubber-70 durormeter

Global Rubber Products Ltd.
7-515 MILNER AVENUE, SCARBOROUGH, ONTARIO M1B 2K4 CANADA
TEL: (416) 293-1990 FAX: (416) 293-1286 EMAIL: info@globalrubber.com
CANADA WIDE 1-800-838-1160

TECHNICAL REPORT

S70 - 70 DUROMETER SILICONE COMPOUND

ASTM D2000 M5GE706 A19 B37 A14 EO16 EO36 C12 F19

ASTM DESIGNATION		ASTM D2000 SPECIFICATION	S70 TYPICAL PROPERTIES
	ORIGINAL PROPERTIES		
	Hardness, Shore A Points	70 +-5	71
	Tensile Strength, psi (mpa)	870 (6)	929 (6.41)
	Ultimate Elongation, %	150	166
	HEAT AGING RESISTANCE (ASTM D573), 70 HRS. @ 225 C (437 F)		
A19	Hardness Change, Shore A Points	+10	+3.0
	Tensile Strength Change, %	-25	+0.3
	Ultimate Elongation Change, %	-30	-22.3
	COMPRESSION SET RESISTANCE (ASTM D395), 22 HRS. @ 175 C (347 F) Method B Plied		
B37	% of Original Deflection	25	22.8
	OZONE RESISTANCE (ASTM D1171), 72 HRS. @ 38C (100.4 F) Method A		
C12	100 mPa OZONE Pressure Zero Elongation	Must Not Crack	Passed
	LOW TEMPERATURE RESISTANCE		
F19	**Brittleness (ASTM D2137) Method A** 3 minutes @-55 C (-67 F)	Must Not Crack	Passed
	FLUID RESISTANCE (ASTM D471), 70 HRS. @ 150 C (302 F) ASTM #1OIL		
EO16	Hardness Change, Shore A Points	-0 to -15	-9.0
	Tensile Strength Change, %	-20	+7.6
	Ultimate Elongation Change, %	-20	-3.6
	Volume Change, %	0 to +10	+4.4
	FLUID RESISTANCE (ASTM D471), 70 HRS. @ 150 C (302 F) *IRM 903 Oil*		
EO36	Hardness Change, Shore A Points	-30	-28.0
	Volume Change, %	+60	+31.5

* IRM 903 903 Oil is the ASTM approved replacement for ASTM # 3 oil

Ingredients are on the FDA approved list and meets D2000M/SAE J200M 5GE 706 A19 B37 C12 EO16 EO36 F19 G11

Appendix E

Calibration process and charts for the bi- and tri-axial accelerometers

E.1 Calibration of bi-axial accelerometer for cylinder

A Dytran Instruments Inc. make calibrator (model 5350) was used to calibrate accelerometers at constant frequency, i.e., 100Hz for various amplitudes. The calibration setup contained a fixed frequency shaker unit (model 5350), a data acquisition system comprising a laptop (Oscilloscope software loaded) along USB Oscilloscope - Handyscope HS4 with 4 channels, sampling 195.3125 kHz at 16 bit resolution (from TiePie engineering, Netherlands), a 4.5 V DC battery pack with four port terminal strip and two Coaxial cables with BNC connectors on one end and the other end open.

Each accelerometer was mounted on the shaker head using bees wax while ensuring the axis coincident to shaker axis being calibrated. This was achieved by aligning the sides of square face of the accelerometer parallel / perpendicular to shaker base manually within ±1.0° accuracy. The positive and negative wires connected to that of battery pack with the help of terminal strip. Similarly the XOUT and YOUT from the accelerometer are connected to channel 1 and channel 2 of the oscilloscope through terminal strip and coaxial cables as shown in Figure E.1-1 and Figure E.1-2. With the oscilloscope connected to laptop through USB cable, the shaker was excited at various acceleration levels starting from 0.1g (PK) to 3.0g (PK). A total of 16 sets of readings were taken for each axis and the data processed for determining the sensitivity of accelerometer. The Figure E.1-3 and Figure E.1-4 show the linear response of accelerometer for various 'g' levels.

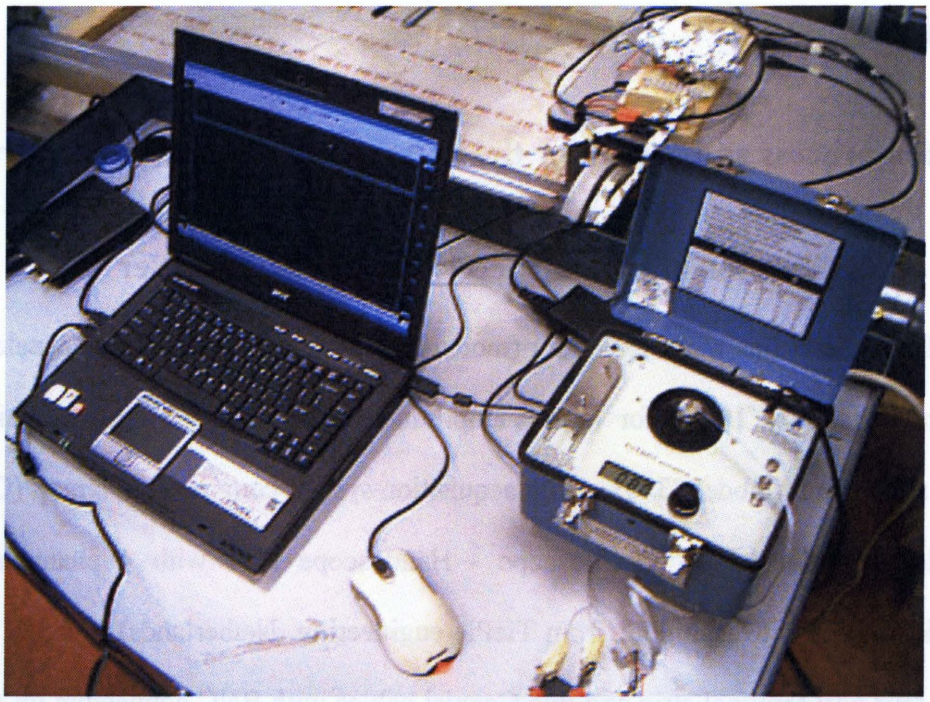

Figure E.1-1 Calibration setup for bi-axial accelerometer for cantilever cylinder in one axis

Figure E.1-2 Calibration setup for bi-axial accelerometer for cantilever cylinder in second axis

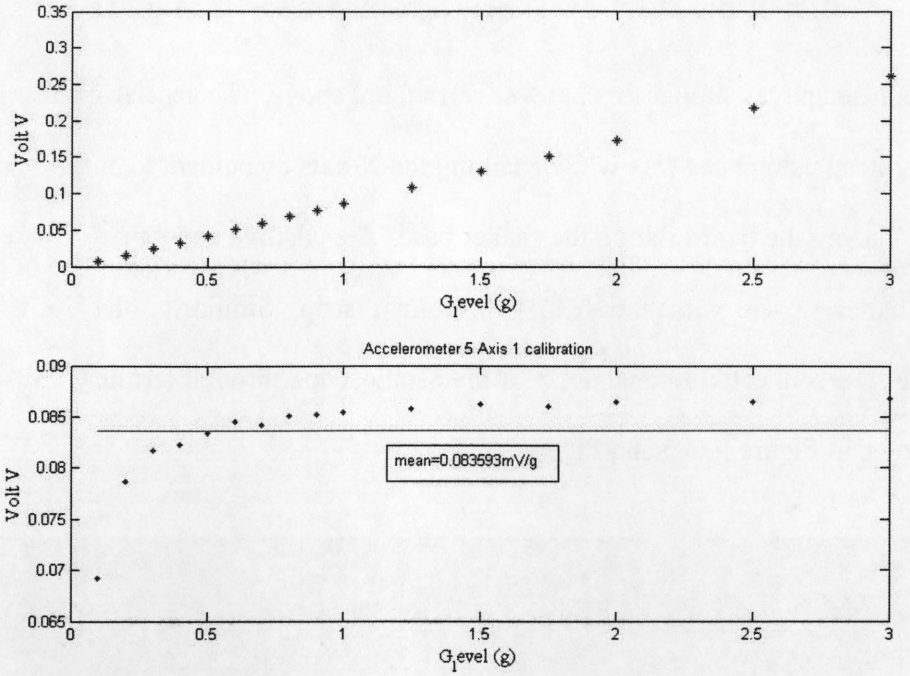

Figure E.1-3 Calibration of accelerometer - axis 1

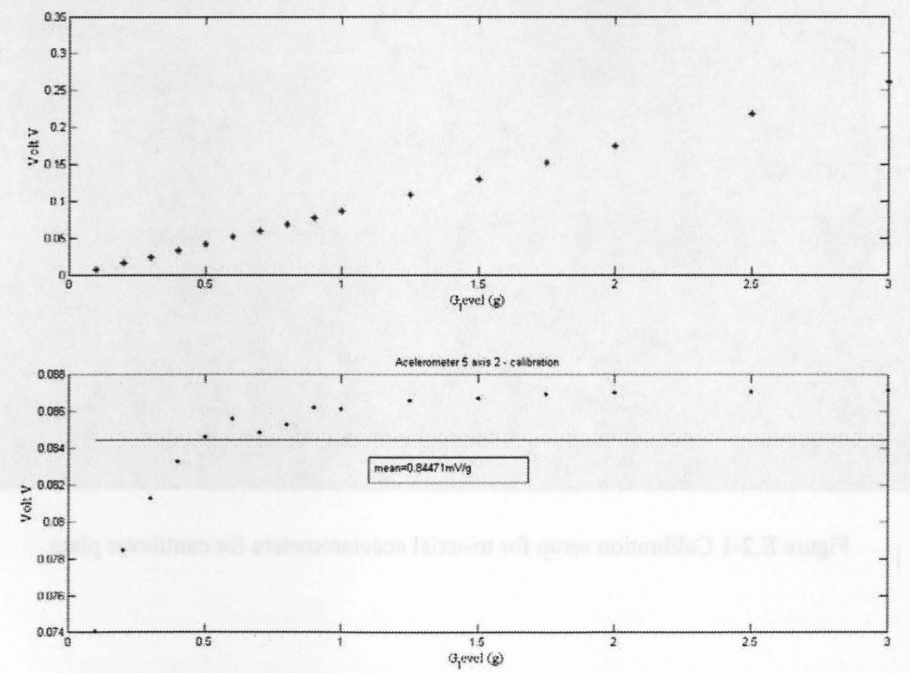

Figure E.1-4 Calibration of accelerometer - axis 2

E.2 Calibration of tri-axial accelerometer for thin plate

The calibration setup was similar to what was carried out above. The accelerometer was mounted on the shaker head using bees wax while ensuring the X-axis coincident to shaker axis. This was achieved by placing the board flat on the shaker base. The positive and negative wires connected to that of battery pack with the help of terminal strip. Similarly, the XOUT from the accelerometer are connected to channel 2 of the oscilloscope through terminal strip and coaxial cables as shown in Figure E.2-1 and Figure E.2-2.

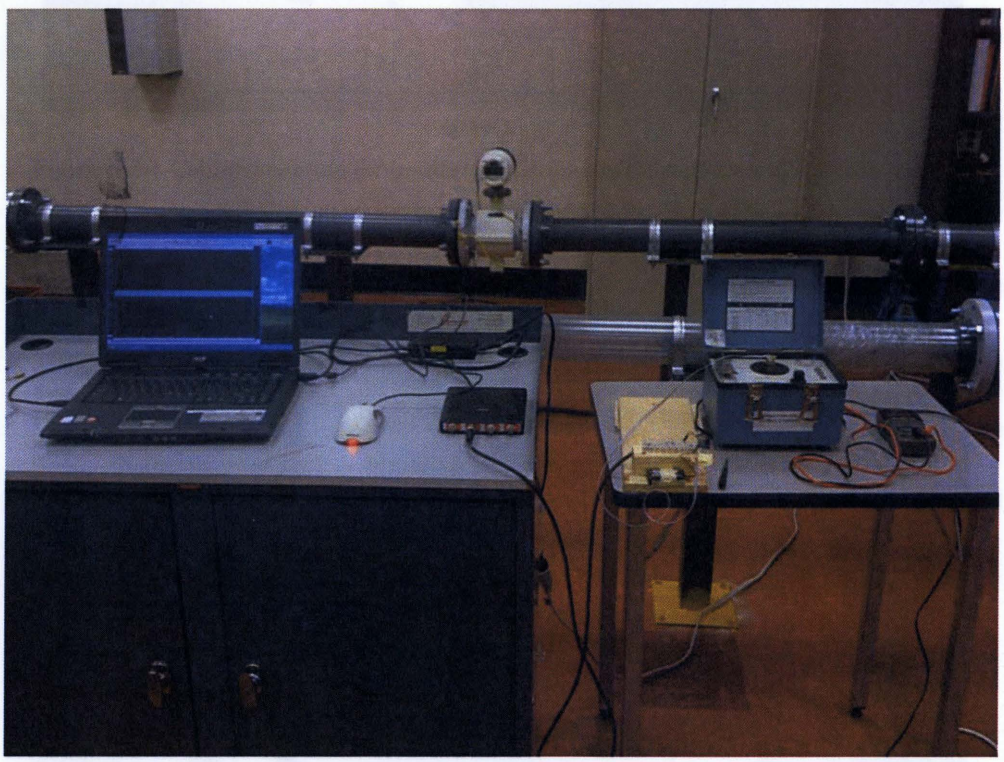

Figure E.2-1 Calibration setup for tri-axial accelerometers for cantilever plate

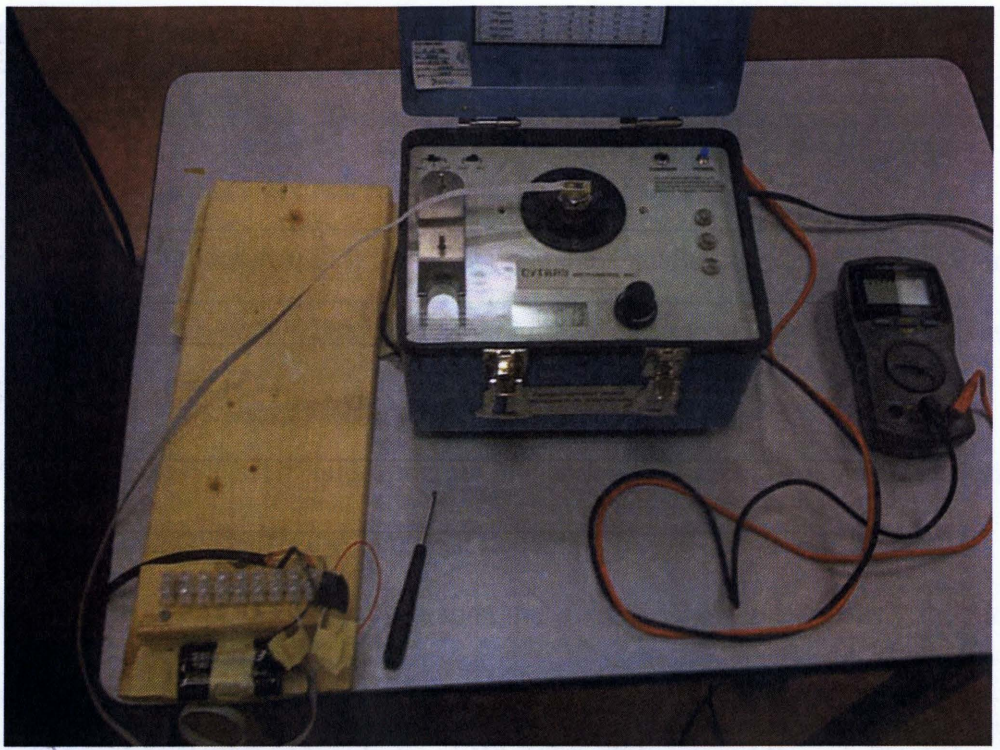

Figure E.2-2 Close-up view of calibration of tri-axial accelerometer for cantilever plate in one axis

With the oscilloscope connected to laptop through USB cable the shaker was excited at various acceleration levels starting from 0.1g (PK) to 2.8g (PK). A total of 19 sets of readings were taken and the data processed for determining the sensitivity of accelerometer in only X axis. The procedure was repeated for two accelerometers. Figure E.2-3 and Figure E.2-4 show the linear response of accelerometer for various 'g' levels.

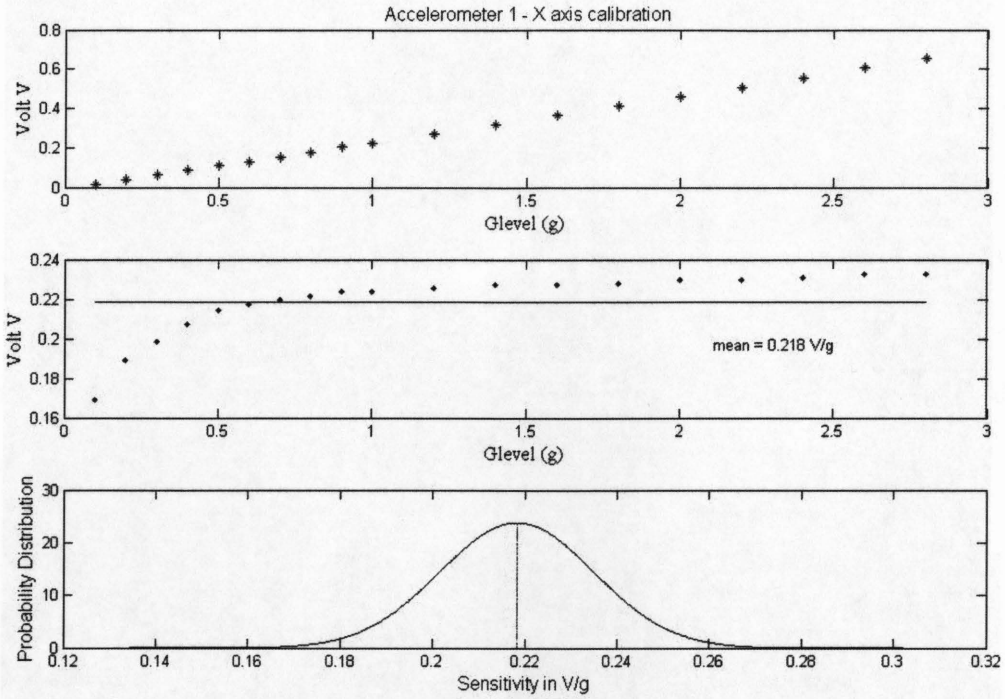

Figure E.2-3 Calibration of tri-axial accelerometer_1

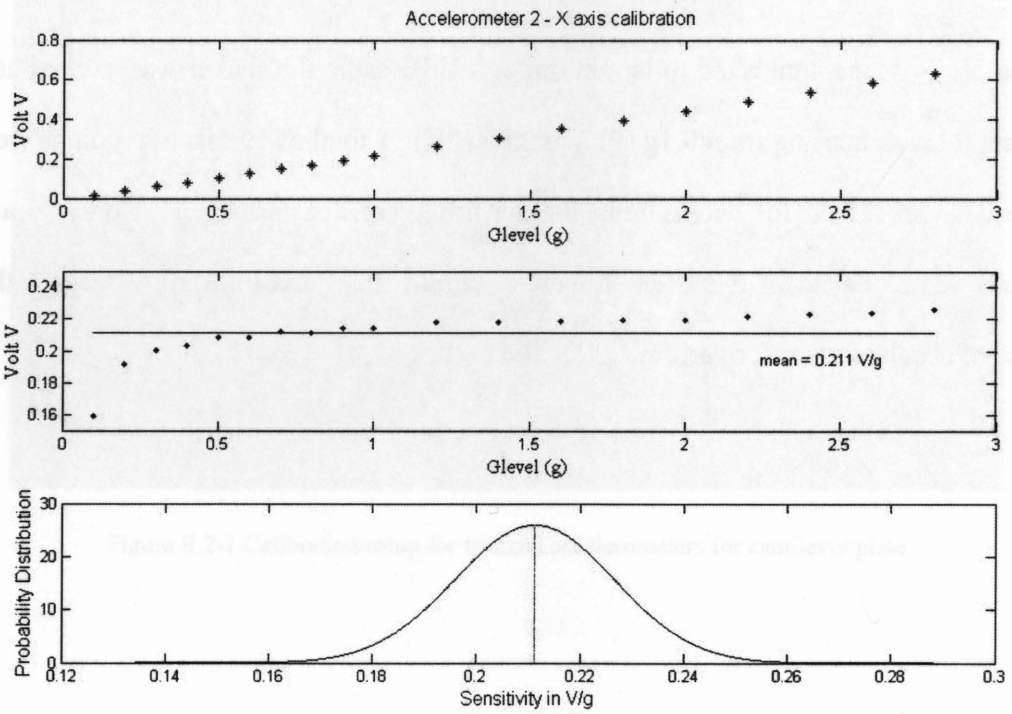

Figure E.2-4 Calibration of tri-axial accelerometer_2

References

1. Païdoussis, M. P. 1966b "Dynamics of flexible slender cylinders in axial flow. Part 2: experiments" Journal of Fluid Mechanics, 26, 737-752.
2. Pettigrew, M.J., Gorman, D.J. 1973 "Experimental studies on Flow Induced Vibration to support Steam Generator Design -1. Vibration of a Heated Cylinder in Two-Phase Axial Flow" Vib Probl in Ind Int Symp.
3. Païdoussis, M. P. 2004 "Fluid-Structure Interactions – Slender Structures and Axial Flow Volume - 2." Elsevier Academic Press, London, UK.
4. Andrew Dimarogonas. 1995 "Vibration for Engineers-second edition." Prentice Hall, Upper Saddle River, NJ.
5. M.K. Au - Yang. 2001 "Flow-Induced Vibration of Power and Process Plant Components – A Practical Work book." ASME Press, New York.
6. Abbasian, F., S.D. Yu and J. Cao., 2009 Experimental and numerical investigations of three-dimensional turbulent flow of water surrounding a CANDU simulation fuel bundle structure inside a channel. Nuclear Engineering Design, 239, 2224-2235.
7. Païdoussis, M.P., Grinevich, E., Adamovic, D., Semler, C. 2002 "Linear and nonlinear dynamics of cantilevered cylinders in axial flow. Part 1: Physical dynamics" Elsevier Science Ltd, Journal for Fluids and Structures, 16, 691-713.
8. Chen.S, Wambsganss, M.W. 1972 "Parallel-flow-induced vibration of fuel rods" Nuclear Engineering and Design, 18, 253-278.
9. Païdoussis, M.P., Pettigrew, M.J. 1979 "Dynamics of flexible cylinders in axisymmetrically confined axial flow" Trans. ASME J. Appl. Mech. Volume 46, 37-44.

10. Tang, L. Païdoussis, M. P. and Jiang, J. 2009 "Cantilevered flexible plates in axial flow: Energy transfer and the concept of flutter-mill" Journal of Sound and Vibration, 26, 263-276.

11. Tang, L. Païdoussis, M. P. and DeLaurier, J.D. 2008 "Flutter-Mill: a New Energy-Harvesting Device" Ontario-sea.org.

12. J. J. Allen and A. J. Smits., 2001 "Energy Harvesting eel." Department of Mechanical and Aerospace Engineering, Princeton University Princeton, NJ 08543, U.S.A , Journal for Fluids and Structures, 15.

13. Païdoussis, M. P. 1998 "Fluid-Structure Interactions – Slender Structures and Axial Flow Volume - 1." Elsevier Academic Press, London, UK.

14. William T. Thomson, Marie Dillon Dahleh. 1998 "Theory of Vibration with Applications, 5th Ed." Prentice Hall, Upper Saddle River, NJ.

15. Val S. Lobanoff, Robert R. Ross. 1992 "Centrifugal Pumps – Design & Application – second edition." Butterworth-Heinemann, Woburn, MA.

16. Michael R. Hatch, 2000 "Vibration Simulation Using MATLAB and ANSYS." Chapman & Hall/Crc, Florida.

17. O'Hara, G. P., 1983 "Mechanical Properties of Silicone Rubber in a Closed Volume." Army Armament Research and Development Center, Large Caliber Weapon Systems Lab, Watervliet, NY.

④ BL-4-44